Supplementary Materials for Elastic-invisibility-enabled metastructure with mechanically programmed nonlinear resonators for vibration attenuation and energy harvesting

João Pedro Norenberg, Americo Cunha Jr, Diego Misseroni*
* E-mail: diego.misseroni@unitn.it (DM)

This PDF file includes:

Supplementary Text
Figures S1 to S40
Tables S1 to S7
Captions for Movies S1 to S6

Other Supplementary Materials for this manuscript:

Movies S1 to S6

Contents

Supplementary Text **S2**

Overview of previous multifunctional metamaterials for vibration attenuation and energy harvesting . . . S3

Elastic invisibility for rectangular voids . . . S5

Mathematical formulation . . . S6

Implementation of the elastic reconstruction in the metabeam . . . S9

Scattering Reduction Coefficient Based on Natural Frequencies . . . S11

Frequency Response Function Analysis . . . S12

Time-Domain Dynamic Response at Resonance . . . S12

Experimental Validation of Cloaking Performance . . . S14

Scattering Reduction Coefficient for the Plate . . . S18

Scattering Measure from Displacement Field Analysis . . . S18

Impact of Elastic Invisibility on Energy Concentration and Energy Harvesting Potential . . . S21

Metabeam with magneto-elastic piezoelectric resonators . . . S23

Nonlinear magnetic force . . . S25

Governing equations of the metabeam . . . S28

Verification of the clamped boundary condition for the resonator beam . . . S33

Numerical procedure . . . S34

Numerical results . . . S37

Fabrication and assembly of the physical prototype . . . S49

Vibration experiments . . . S55

Experimental setup . . . S55

Experimental results . . . S56

Energy harvesting demonstration and low-power sensing potential . . . S71

0-1 test for chaos . . . S76

Caption for Movies . . . S78

References and Notes **S79**

Supplementary Text

Overview of previous multifunctional metamaterials for vibration attenuation and energy harvesting

Metamaterials have shown strong potential for combined energy harvesting and vibration attenuation. One early example is the development of a unit cell combining a spring-loaded magnet and copper coils for linear electromagnetic harvesting, which demonstrated a bandgap between 146–171 Hz and harvested up to 36 mW (*1*). Another approach used a 3D-printed 10×10 array of cantilevers with piezoelectric patches, achieving a similar bandgap and a peak power of approximately 0.05 μW (*2*). A triboelectric nanogenerator-based metamaterial was also introduced, creating a bandgap near 190 Hz and an output power of 124.6 nW (*3*). More recently, nonlinear piezoelectric resonators using multistable dynamics have been implemented to enhance broadband performance, achieving bandgaps in the 12.5–16 Hz range and harvesting up to 6 mW (*4, 5*). Another study used a 10×10 array of resonator beams with a central 4×4 defect region, placing a piezoelectric patch at the defect to achieve a bandgap between 291–451 Hz and generate 18.6 nW (*6*). A chiral metastructure with five units and a geometric defect hosting a piezoelectric layer was developed, demonstrating a bandgap from 120–600 Hz under flexural and longitudinal excitation, harvesting 0.016 μW and 0.27 μW, respectively (*7*). Other studies have also explored multifunctionality in metamaterials, particularly for acoustic filtering applications (*8–10*).

Although these studies have significantly advanced multifunctional metamaterials, several challenges remain for their integration into physical structures. Many reported architectures operate over fixed or narrow frequency ranges, limiting their ability to adapt to changing excitation conditions. Others rely on external resonator attachments, defect regions, or geometrically complex unit cells that may add bulk, break structural symmetry, introduce parasitic modes, or perturb the background dynamics of the host. These limitations highlight the need for multifunctional metastructures that combine tunability, compact internal integration, broadband or reconfigurable operation, efficient vibration attenuation and energy harvesting, and preservation of the dynamic integrity of the host structure.

The present work addresses this need by combining elastic invisibility with nonlinear magnetoelastic piezoelectric resonators. The internal voids required to embed the resonators are mechanically reconstructed by restoring the stiffness, mass, and mass moment of inertia removed from the host, so that the modified beam recovers a near-intact dynamic response. Within these dynamically reconstructed integration bays, the resonators act as mechanically programmed functional inserts whose nonlinear states are prescribed by magnet spacing. This architecture therefore differs from conventional externally attached or defect-based designs by combining internal resonator integration, host-dynamics preservation, locally programmed nonlinear response, vibration attenuation, and electromechanical conversion within the same metastructure.

Table S1 presents a comparative overview of relevant multifunctional metamaterials for vibration attenuation and energy harvesting. For each work, the table summarizes the system architecture, operating mechanism, geometric scale of the host (H) and unit (U) cells, reported bandgap bandwidth, reported electrical output, and additional functional attributes. Because the reported electrical outputs were obtained under different excitation levels, load conditions, transduction mechanisms, and measurement definitions, the table is intended as a contextual comparison of architectures and reported performance rather than a direct ranking of harvesting efficiency. This comparison highlights the distinct contribution of the present metastructure, which combines internal resonator integration, elastic-invisibility-based host preservation, magnet-spacing-programmed nonlinear states, vibration attenuation, and electromechanical conversion within a single structural platform.

Table S1: Overview of multifunctional metamaterial studies for vibration attenuation and energy harvesting compared with the present work. Reported values and features are taken from the cited references.

Work	**System**	**Bandgap**	**Peak output**	**Key features**
Present work	Beam with 7 internal magneto-piezoelectric resonators Mechanism: *local resonance and piezoelectric effect* Size: H: 985 mm; U: 85 mm	35–90 Hz	~10.7 μW (resonance) and ~2.05 μW (bandgap)	Elastic invisibility: *Yes* Tunability: *adjusting the magnet spacing* Nonlinearity: *multistable resonators* Complexity: *Low*
Mikoshiba et al. (2013) (*1*)	Hollow tube with 7 units of spring-loaded magnets and copper coils Mechanism: *local resonance and electromagnetic induction* Size: H: 333.2 mm; U: 47.6 mm	146.5–171 Hz	~36 mW	Elastic invisibility: *No* Tunability: *No* Nonlinearity: *No* Complexity: *Low*
Lu et al. (2021) (*11*)	Beam periodically arrayed with spherical-cavity nonlinear resonators containing rolling balls and electromagnetic coils Mechanism: *local resonance/Bragg scattering and electromagnetic induction* Size: H: no information; U: 100 mm	6–7 Hz and 45–65 Hz	no information	Elastic invisibility: *No* Tunability: *No* Nonlinearity: *nonlinear spherical pendulum* Complexity: *Medium*
Li et al. (2017) (*2*)	Plate with 10×10 cells; each with 4 cantilever beams (400 beams total) Mechanism: *local resonance and piezoelectric effect* Size: H: 25×25 cm^2; U: 2.5 cm	146–171 Hz	~0.05 μW	Elastic invisibility: *No* Tunability: *No* Nonlinearity: *No* Complexity: *High*

Continued on next page

Continued from previous page

Work	System	Bandgap	Peak output	Key features
Xu et al. (2022) (*3*)	Plate with chiral beam-like unit cell (48 total), each with central mass Mechanism: *local resonance and triboelectric effect* Size: H: –; U: 12×12 mm^2	≈190 Hz (bandwidth not reported)	124.6 nW	Elastic invisibility: *No* Tunability: *No* Nonlinearity: *chiral structure* Complexity: *High*
Xu et al. (2023) (*4*), Xu, C. et al. (2024) (*5*)	Beam with 12 lateral piezoelectric resonators on both sides of host beam Mechanism: *local resonance and piezoelectric effect* Size: H: 850 mm; U: 97.5 mm	12.5–14.6 Hz (linear) bandwidth ↑ 52% (nonlinear)	6 mW (linear)	Elastic invisibility: *No* Tunability: *adjusting the resonator length* Nonlinearity: *multistable resonators* Complexity: *Medium*
Hyun et al. (2024) (*6*)	Plate with 10×10 coupled beam resonators; 4×4 central cells removed to form defect with PZT Mechanism: *local resonance and piezoelectric effect* Size: H: 400×320 mm^2; U: 24×25 mm^2	291–451 Hz	18.6 nW	Elastic invisibility: *No* Tunability: *No* Nonlinearity: *No* Complexity: *Medium*
Park et al. (2024) (*7*)	Chiral structure with 5 units; defect introduced by changing base thickness; PZT at defect base Mechanism: *local resonance and piezoelectric effect* Size: H: –; U: 40×40 mm^2	120–600 Hz	0.016 μW and 0.27 μW	Elastic invisibility: *No* Tunability: *No* Nonlinearity: *chiral structure* Complexity: *High*
Ahmed et al. (2014) (*8*)	Aluminum frame with cylindrical matrix enclosing a heavy core and a piezoelectric layer between the core and cavity wall Mechanism: *local resonance and piezoelectric effect* Size: H: –; U: $36.5 \times 36.5 \times 14$ mm^3	0.3–1.1 kHz	90 μW	Elastic invisibility: *No* Tunability: *No* Nonlinearity: *No* Complexity: *Medium*
Li et al. (2016) (*9*)	Membrane-type acoustic metamaterial with aluminum boundary ring and sheets with flexible piezoelectric Mechanism: *local resonance and piezoelectric effect* Size: H: –; U: 50 mm	≈356–432 Hz	0.16 V	Elastic invisibility: *No* Tunability: *No* Nonlinearity: *No* Complexity: *Medium*
Chen et al. (2019) (*10*)	Beam with pretensioned elastic membrane resonators and split-ring masses (9 units) Mechanism: *local resonance and piezoelectric effect* Size: H: 405 mm; U: 36 mm	340–426 Hz	≈1.2 μW	Elastic invisibility: *No* Tunability: *No* Nonlinearity: *No* Complexity: *Low*

Table end

Elastic invisibility for rectangular voids

We adopt an elastic invisibility strategy based on the reinforcement of the boundaries and mass redistribution to render the voids embedded in the beam invisible to elastic wave propagation; in other words, dynamically equivalent to an intact beam. To achieve this equivalence, we reinforce the boundaries of the voids with a frame whose dimensions were determined to match the target flexural and torsional rigidities within the adopted equivalent-continuum model. In addition to the rigidities, the removed mass and mass moment of inertia were also conserved (*12*).

Building on (*12*), which proposed an elastic-invisibility design for square voids, we generalize the elastic-reconstruction conditions to rectangular voids. In the following, we provide a detailed mathematical formulation for the cloaking design and finite-element simulations to demonstrate its effectiveness. Furthermore, we validate our approach through experimental modal analysis by comparing an uncloaked beam with a cloaked beam.

Mathematical formulation

The elastic reconstruction methodology is first formulated for a generic rectangular void of dimensions $a_x \times a_y$ introduced into a host structure of thickness h, as illustrated in Fig. S1A. The host material is characterized by Young's modulus E_p, density ρ_p, and Poisson's ratio ν_p. To recover the mechanical properties removed from the host, a rectangular reinforcement frame is bonded symmetrically to both faces of the structure. The frame consists of two members parallel to the x-axis, each with width b_y, and two members parallel to the y-axis, each with width b_x. Each reinforcement layer has thickness h_t (Fig. S1B).

For the analytical formulation, the reinforcement frame is represented by an equivalent orthogonal grid, as shown in Fig. S1C. The two members parallel to the x-axis are represented by a single equivalent member of width $2b_y$, whereas the two members parallel to the y-axis are represented by a single equivalent member of width $2b_x$. The resulting grid occupies a region of dimensions $(a_x + 2b_x) \times (a_y + 2b_y)$. Because the reinforcement is bonded symmetrically to both faces of the host, the effective thickness of the reinforced sections is $h + 2h_t$.

The material removed from the host is modeled as an isotropic elastic plate undergoing transverse displacement $w(x, y, t)$. According to classical plate theory (*13, 14*), its equation of motion is

$$\boxed{\rho_p h \frac{\partial^2 w}{\partial t^2} + D\frac{\partial^4 w}{\partial x^4} + 2D\frac{\partial^4 w}{\partial x^2 \partial y^2} + D\frac{\partial^4 w}{\partial y^4} = q(x, y, t),} \tag{S1}$$

where $q(x, y, t)$ is the distributed transverse load and

$$D = \frac{E_p h^3}{12(1 - \nu_p^2)} \tag{S2}$$

is the bending rigidity of the removed plate.

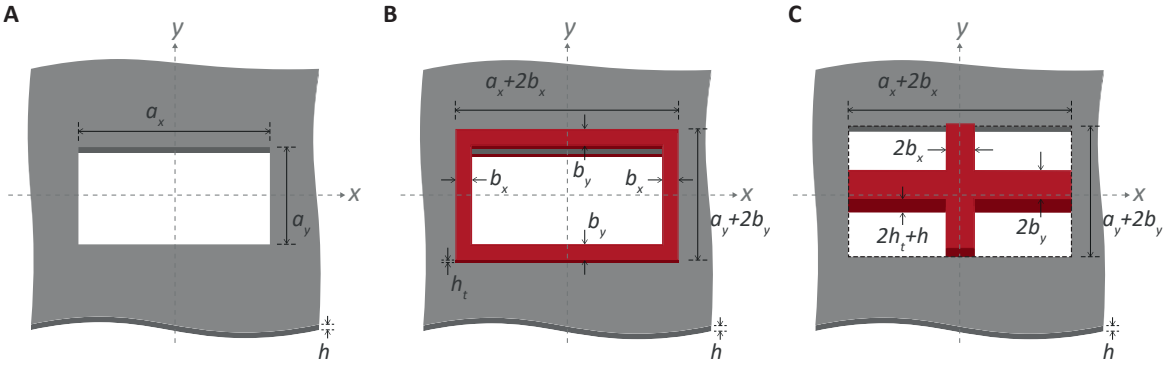


Figure S1: Generic elastic reconstruction formulation for a rectangular void. (A) Rectangular void of dimensions $a_x \times a_y$ introduced into the host structure. (B) Physical reinforcement frame with in-plane widths b_x and b_y and reinforcement thickness h_t. (C) Equivalent orthogonal grid used in the analytical stiffness formulation, with member widths $2b_x$ and $2b_y$ and effective thickness $h + 2h_t$.

Following the equivalent grid representation for orthogonal gridworks (*13*), the reinforcement can be described in terms of an equivalent anisotropic elastic plate

$$\boxed{(\rho h + \rho 2h_t)\frac{\partial^2 w}{\partial t^2} + D_x\frac{\partial^4 w}{\partial x^4} + 2H\frac{\partial^4 w}{\partial x^2 \partial y^2} + D_y\frac{\partial^4 w}{\partial y^4} = q(x,y,t).} \tag{S3}$$

where ρ and h_t are the density and thickness of the reinforcement frame, respectively, and D_x, D_y, and H characterize its flexural and torsional stiffnesses. The equivalent plate representation is used here to establish the stiffness reconstruction conditions.

B_x and C_x denote the flexural and torsional rigidities of the members oriented parallel to the x-axis, whereas B_y and C_y denote those of the members oriented parallel to the y-axis:

$$B_x = EJ_x, \qquad B_y = EJ_y, \qquad C_x = GJ_{t,x}, \qquad C_y = GJ_{t,y}, \tag{S4}$$

where E and G are the Young's and shear moduli of the reinforcement material, respectively. The quantities J_x and J_y are the second moments of area associated with the x- and y-oriented beams, and $J_{t,x}$ and $J_{t,y}$ are their corresponding torsion constants.

The second moments of area for out-of-plane bending of a single x- and y-oriented reinforcing member are

$$J_x = \frac{1}{12}b_y(h+2h_t)^3, \qquad J_y = \frac{1}{12}b_x(h+2h_t)^3. \tag{S5}$$

As shown in Fig. S1C, each equivalent grid member represents two symmetric reinforcing members. Thus, the x-oriented pair has combined flexural and torsional rigidities $2B_x$ and $2C_x$ over the transverse spacing $a_y + 2b_y$, while the y-oriented pair has corresponding rigidities $2B_y$ and $2C_y$ over the transverse spacing $a_x + 2b_x$. Defining the corresponding half-spacing as

$$d_x = a_y/2 + b_y, \qquad d_y = a_x/2 + b_x, \tag{S6}$$

the equivalent grid rigidities become

$$D_x = \frac{B_x}{d_x}, \qquad D_y = \frac{B_y}{d_y}, \qquad 2H = \frac{C_x}{d_x} + \frac{C_y}{d_y}. \tag{S7}$$

Elastic reconstruction requires the equivalent grid to recover the flexural and torsional rigidities of the material removed from the host. Equating the stiffness coefficients of Eqs. S1 and S3 therefore yields

$$\boxed{\frac{B_x}{d_x} = \frac{B_y}{d_y} = \frac{E_p h^3}{12(1-\nu_p^2)} \qquad \text{and} \qquad \frac{C_x}{d_x} + \frac{C_y}{d_y} = \frac{E_p h^3}{6(1-\nu_p^2)}.} \tag{S8}$$

The first two conditions restore the flexural rigidity of the removed region along the two principal directions, while the third restores its torsional contribution.

The inertial properties are reconstructed separately. Let M_p denote the mass of the corresponding intact reference region and $I_{p,x}$ and $I_{p,y}$ its mass moments of inertia about the centroidal x- and y-axes, respectively. After the reinforcement dimensions have been determined from Eq. S8, the mass M and mass moments of inertia I_x and I_y of the reconstructed frame, including the remaining host and the bonded reinforcement layers, are evaluated before the addition of the discrete compensating masses.

Additional discrete masses m_i are positioned around the reconstructed region at in-plane offsets $\tilde{d}_{x,i}$ and $\tilde{d}_{y,i}$ from its centroidal axes. Under the thin-plate representation, conservation of mass and of the mass moments of inertia requires

$$\boxed{\begin{aligned} M_p &= M + \sum_{i=1}^{n} m_i, \\ I_{p,x} &= I_x + \sum_{i=1}^{n} m_i \tilde{d}_{y,i}^{\,2}, \\ I_{p,y} &= I_y + \sum_{i=1}^{n} m_i \tilde{d}_{x,i}^{\,2}. \end{aligned}} \tag{S9}$$

The perpendicular offset enters each mass moment of inertia, such that I_x depends on $\tilde{d}_{y,i}$ and I_y on $\tilde{d}_{x,i}$. Denoting $L_x = a_x + 2b_x$ and $L_y = a_y + 2b_y$, the mass and mass moments of inertia of the corresponding intact plate region are

$$M_p = \rho_p h L_x L_y, \quad I_{p,x} = \frac{M_p L_y^2}{12}, \quad I_{p,y} = \frac{M_p L_x^2}{12}. \tag{S10}$$

For the symmetric reconstructed frame, the inertial properties are obtained by superposition of the outer rectangle and the inner rectangular opening. Thus,

$$M = M_o - M_v, \quad I_x = \frac{1}{12}\left(M_o L_y^2 - M_v a_y^2\right), \quad I_y = \frac{1}{12}\left(M_o L_x^2 - M_v a_x^2\right), \tag{S11}$$

where $M_o = \left(\rho_p h + 2\rho h_t\right) L_x L_y$ and $M_v = \left(\rho_p h + 2\rho h_t\right) a_x a_y$.

The reconstruction is therefore performed in two stages. First, the reinforcement dimensions b_x, b_y, and h_t are determined from the flexural- and torsional-rigidity equivalence conditions in Eq. S8. The inertial properties of the resulting reconstructed frame are then evaluated, and the discrete compensating masses are determined from the mass and mass-moment equivalence conditions in Eq. S9.

Implementation of the elastic reconstruction in the metabeam

The generic elastic reconstruction formulation is adapted to the geometry required for integrating the piezoelectric resonator, as illustrated in Fig. S2. The original rectangular void, with dimensions $a_x \times a_y = 118 \times 30$ mm^2, is divided by a transverse crossbar into a small opening of length $a_{x,1} = 8$ mm and a large opening of length $a_{x,2} = 103$ mm, such that $a_x = a_{x,1} + b_c + a_{x,2}$, as illustrated in Fig. S2A. The crossbar provides the clamping region for the piezoelectric resonator. Its prescribed width, $b_c = 7$ mm, follows the mounting recommendation of the piezoelectric manufacturer and is therefore retained as part of the reconstructed structure. The local axes y_1 and y_2 pass through the centroids of the small and large openings, respectively, and are parallel to the transverse direction. They are used as the reference axes when applying the generic reconstruction formulation to each opening.

The physical reinforcement is shown in Fig. S2B. The two outer members oriented in the transverse direction, parallel to the local axes y_1 and y_2, have widths $b_{x,1}$ and $b_{x,2}$, whereas the upper and lower longitudinal members, parallel to the x-axis, have a common width b_y. Reinforcement layers of thickness h_t are bonded symmetrically to both faces of the host, resulting in an effective reinforced thickness $h + 2h_t$.

For the stiffness calculation, the generic rectangular void formulation is adapted to the two openings through the adjacent equivalent grids shown in Fig. S2C. For the small opening, the generic dimensions a_x and b_x are replaced by $a_{x,1}$ and $b_{x,1}$, respectively, resulting in an equivalent y-oriented member of width $2b_{x,1}$. The corresponding portion $b_{x,1}$ of the crossbar is therefore associated with this grid. The remaining crossbar width, $b_c - b_{x,1}$, is combined with the outer reinforcement $b_{x,2}$ to form the y-oriented member of the second grid, with equivalent width $b_{x,2} + b_c - b_{x,1}$. Because both openings have the same transverse dimension and share the upper and lower reinforcement, a_y, b_y, and h_t are common to both grids.

The corresponding grid spacings, second moments of area, and torsional rigidities are evaluated

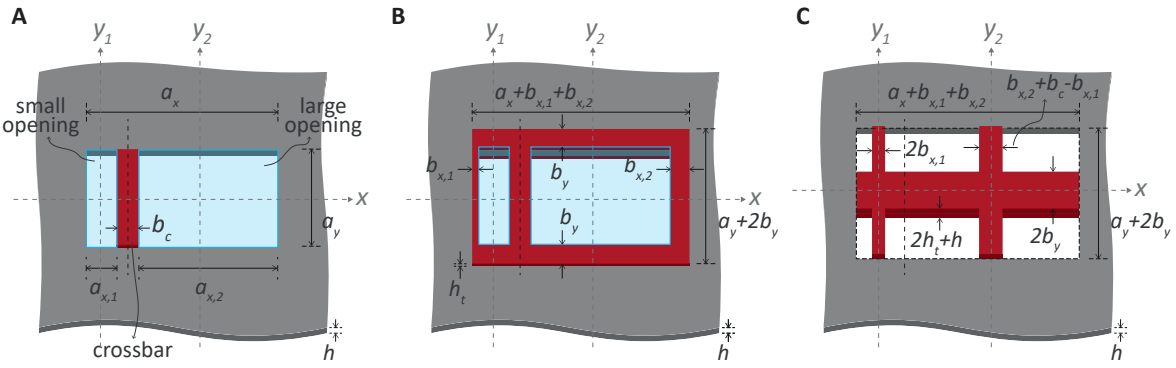


Figure S2: Elastic reconstruction of the metabeam geometry. (A) Original rectangular void partitioned by the crossbar into small and large openings, with local centroidal axes y_1 and y_2. (B) Physical reinforcement bonded symmetrically to both faces of the host. (C) Equivalent grids used to apply the generic reconstruction formulation to the two openings.

for each grid using the expressions derived in the generic formulation and substituted into the flexural- and torsional-rigidity equivalence conditions. The prescribed dimensions $a_{x,1}$, $a_{x,2}$, a_y, and b_c are kept fixed, while the reinforcement dimensions are determined numerically in MATLAB by minimizing the residuals of the flexural- and torsional-rigidity equivalence conditions. Both the host and reinforcement are represented using the effective carbon fiber properties $E = 62$ GPa, $\rho = 1335\,\mathrm{kg\,m^{-3}}$, and $\nu = 0.3$, with $G = E/[2(1+\nu)]$. These parameters constitute an effective isotropic representation of the laminate used in the reduced reconstruction model. This approximation is adopted to obtain the reinforcement geometry and is subsequently assessed through the finite-element and experimental modal comparisons. The resulting reinforcement dimensions are $b_{x,1} = 0.55$ mm, $b_{x,2} = 7.15$ mm, $b_y = 2.08$ mm, and $h_t = 1.08$ mm.

Once the reinforcement geometry is determined, the mass and principal mass moments of inertia of each reconstructed region, including the remaining host and bonded reinforcement layers, are evaluated from the physical geometry, as shown in Fig. S3. The compensating masses are then determined analytically to recover the remaining differences relative to the corresponding intact regions. Their positions are prescribed relative to the local centroidal axes so that the principal mass moments of inertia can be adjusted independently. Masses offset from the x-axis contribute to I_x, and masses offset along the x-direction from the local axes y_1 and y_2 contribute to I_{y_1} and I_{y_2}, respectively.

For the small opening, masses m_1 and m_2 are positioned symmetrically about the x-axis, each at a distance $\tilde{d}_y$, while m_3 is positioned along the x-axis at a distance $\tilde{d}_{x,1}$ from y_1. For the large opening, masses m_4 and m_5 are positioned symmetrically about the x-axis, each at a distance $\tilde{d}_y$, while m_6 is positioned along the x-axis at a distance $\tilde{d}_{x,2}$ from y_2. The analytically determined compensating masses are $m_1 = m_2 = 0.017$ g, $m_3 = 0.11$ g, $m_4 = m_5 = 0.38$ g and $m_6 = 5.31$ g.

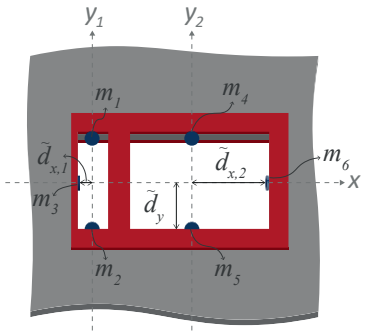


Figure S3: Arrangement of the compensating masses for the small and large reconstructed openings.

Due to machining tolerances and fabrication constraints, the manufactured reinforcement adopts $b_{x,1} = 1$ mm, $b_{x,2} = 7.1$ mm, $b_y = 2.1$ mm, and $h_t = 1.1$ mm. In addition, the analytically determined masses m_1, m_2, and m_3, associated with the small opening, are sufficiently small that they are neglected in the manufactured structure. The numerical and experimental validation presented below shows that these fabrication simplifications preserve the reconstructed dynamic response.

Scattering Reduction Coefficient Based on Natural Frequencies

To demonstrate the effectiveness of the cloaking design, we conduct a finite element numerical simulation using ABAQUS. Initially, we implement the cloaking design on a cantilever beam with dimensions of $985 \times 45 \times 2$ mm^3 with seven rectangular voids measuring 118×30 mm^2, matching those of the metastructure proposed in this paper (see Fig. S4A). The beam is subjected to sinusoidal base excitation with null rotation, inducing elastic wave propagation in the beam. About 25000 quadratic tetrahedral elements of type C3D10 are employed to discretize the structure. The eigenmodes and the steady-state frequency response are obtained using the Lanczos solver. To check the accuracy of cloaking, we use the natural frequencies of the transverse modes for the intact beam, uncloaked beam (voids without reinforcements), and cloaked beam (voids with reinforcements). Results of finite element model simulations are reported in Fig. S4. The scattering reduction coefficient (SRC) is then computed as a measure of cloaking accuracy,

$$\boxed{\text{SRC} = \frac{|f^c - f^i|}{|f^v - f^i|}} \tag{S12}$$

depending on the eigenvalues of the cloaked structure, f^c, the uncloaked structure, f^v, and the intact structure, f^i. When the SRC is equal to 0, it signifies that the cloaking design is perfect, i.e., the cloaked structure behaves identically to an intact one. Conversely, an SRC equal to 1 implies that the cloaking is inefficient, and a value greater than 1 means that the uncloaked structure behaves

	1^{st} mode	2^{nd} mode	3^{th} mode	4^{th} mode	5^{th} mode	6^{th} mode
Intact beam	2.27 Hz	14.27 Hz	39.98 Hz	78.38 Hz	129.65 Hz	193.84 Hz
Uncloaked beam	2.01 Hz	12.61 Hz	35.42 Hz	69.61 Hz	115.39 Hz	172.46 Hz
Cloaked beam	2.27 Hz	14.28 Hz	40.03 Hz	78.46 Hz	129.32 Hz	190.49 Hz
SRC	0.0000	0.0060	0.0110	0.0091	0.0231	0.1567

Table S2: Natural frequencies of the initial six transverse modes for the cantilever beam under intact, cloaked, and uncloaked conditions. The scattering reduction coefficients (SRC) for each mode are also displayed.

more similarly to an intact structure than the cloaked one. Figure S4B demonstrates the SRC for the initial six transverse modes, with their respective values reported in Tab. S2. The first five cloaked natural frequencies differ from the intact beam by less than 0.25%, and the sixth differs by less than 1.8%. The transverse mode shapes associated with the first four modes are reported in Fig. S4C. The efficacy of the cloaking mechanism becomes evident upon comparing the behaviors of beams with cloaked and uncloaked voids. The cloaked beam dynamically behaves almost identically to the intact beam, whereas the uncloaked beam displays significant differences, since when the intact and cloaked beams are in resonance, the uncloaked beam is far from the resonance condition.

Frequency Response Function Analysis

The frequency-response functions (FRFs) of the three beams are also calculatedby applying a concentrated force at their tip and measuring the resulting displacement over the frequency range of 1 Hz to 200 Hz. As shown in Fig. S5, the FRF of the cloaked beam matches closely that of the intact beam, confirming the effectiveness of the cloaking design. In contrast, the uncloaked beam exhibits substantial differences, demonstrating the detrimental effects of the voids in the absence of cloaking.

Time-Domain Dynamic Response at Resonance

We perform transient finite-element simulations to assess the time responses of the three beam configurations. A single-sine harmonic excitation is applied at the base of each beam, with the excitation frequencies set to match the natural frequencies of the intact beam, and the resulting tip displacements are recorded. Figure S6 shows the displacement for frequency excitations of (A) 2.3 Hz, (B) 14.3 Hz, (C) 40 Hz, (D) 78.4 Hz, (E) 129.5 Hz, and (F) 191.5 Hz. The cloaked beam exhibits nearly identical time-series responses to the intact beam for all frequency values. Minor discrepancies in amplitude are attributable to slight shifts in natural frequencies due to the fabrication tolerances of the reinforcement frames. In contrast, the uncloaked beam shows significant discrepancies in amplitude and frequencies because they are outside the resonance condition. This

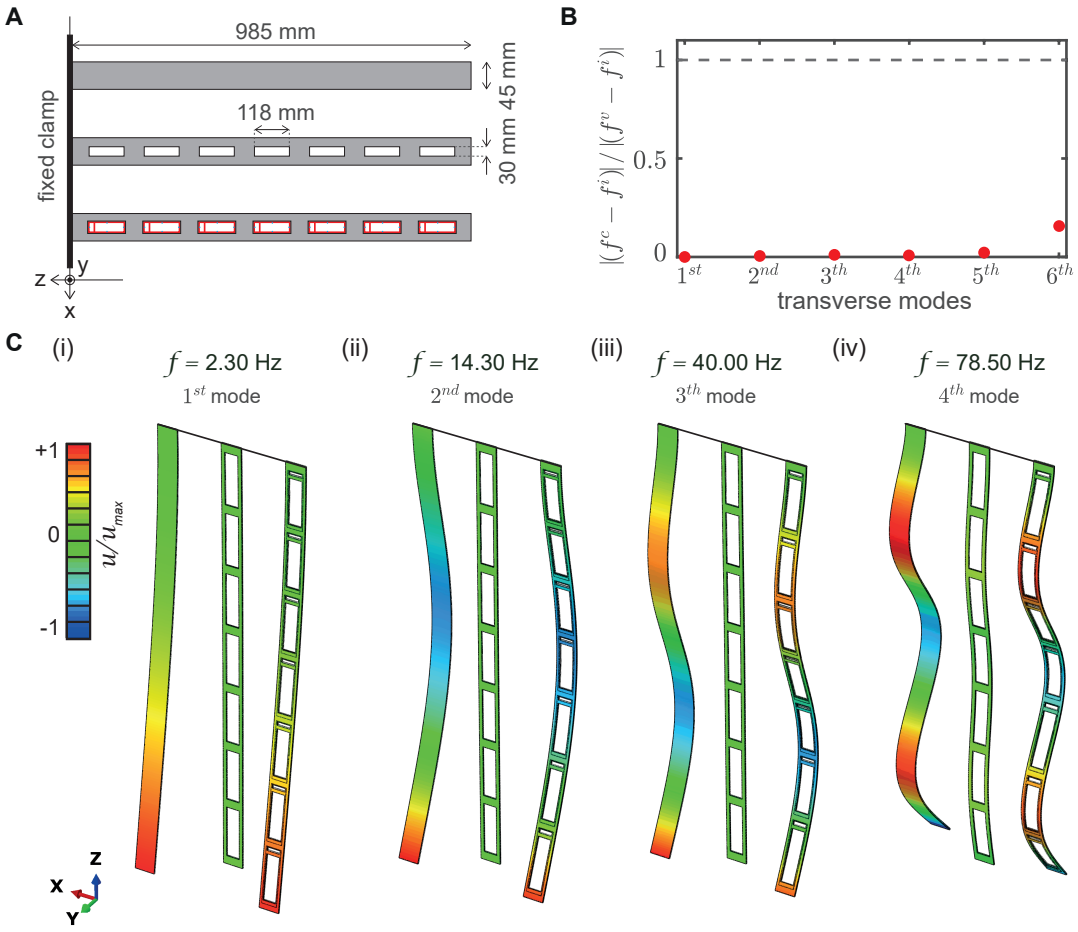


Figure S4: Finite-element simulation results of the cloaking performance on a cantilever beam with seven rectangular voids. (A) Setup of intact, uncloaked, and cloaked beams. One end of the beams is clamped, while the other end is free to vibrate. A sinusoidal base vibration with null rotation is applied along the y-axis. (B) Illustration of the Scattering Reduction Coefficient (SRC) for the initial six resonance modes of the cantilever beam. (C) Eigenmodes of the intact beam (on the left), the uncloaked beam (in the middle), and the cloaked beam (on the right) for the first (i), second (ii), third (iii), and fourth modes (iv).

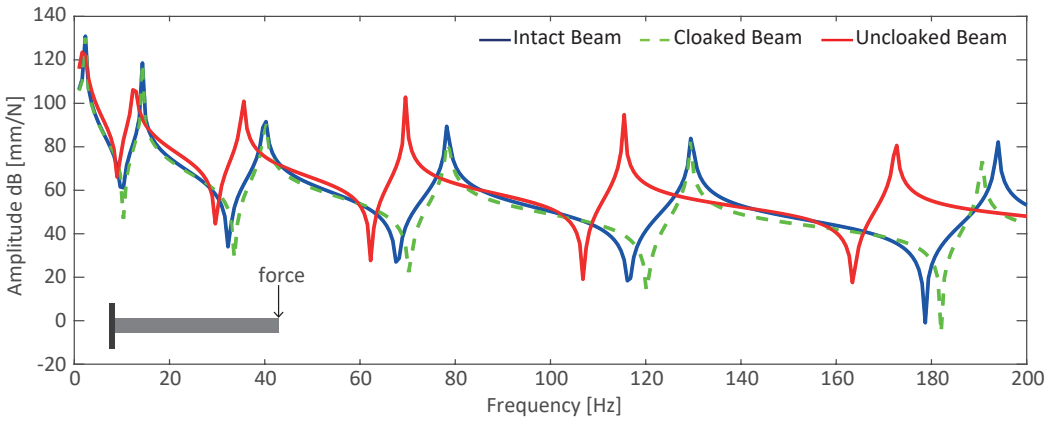


Figure S5: Frequency response functions of the intact, cloaked, and uncloaked beams.

divergence confirms that the presence of internal voids, uncompensated by cloaking, severely disrupts the dynamic integrity of the structure.

We further investigated the behavior of the system under pulse excitation from the base, capturing how waves propagate through each medium. Finite-element simulations are carried out using single-pulse inputs at various frequencies, and displacements are recorded over time at several locations along the beam (x_1 through x_7, coinciding with resonator positions) as well as at the beam tip ($\mathrm{w}(L,t)$). Figures S7 and S8 present time-series comparisons for excitations at 14.3 Hz, 40 Hz, 78.4 Hz, and 129.5 Hz. These results clearly illustrate that the waveforms traveling through the cloaked and continuous beams are nearly identical in shape, arrival time, and phase, thereby demonstrating comparable wave propagation behavior. Conversely, the uncloaked configuration shows significant distortion, delay, and amplitude attenuation, again confirming its impaired dynamic performance.

These observations reinforce that modal equivalence between the cloaked and intact beams achieves high fidelity, manifesting both in the global dynamic response and wave propagation characteristics.

Experimental Validation of Cloaking Performance

The beam with voids and the reinforcements are fabricated as described in Section Fabrication and assembly of the physical prototype. Free vibration tests are conducted to determine the first natural frequencies of the uncloaked and cloaked beams. For each test, the beam is fixed on the shaker, and a single impact is applied at the midpoint of the beam. The velocity field is measured using the VIC-3D system (described in Section Experimental setup), and the response of the system in the frequency domain is obtained through Fast Fourier Transform analysis.

The experimental results, including their natural frequencies, are shown in Fig. S9. Figure S9A shows that the frequency responses of the uncloaked and cloaked beams are notably distinct. The resonance conditions of these structures are defined in different frequency ranges, mainly for higher

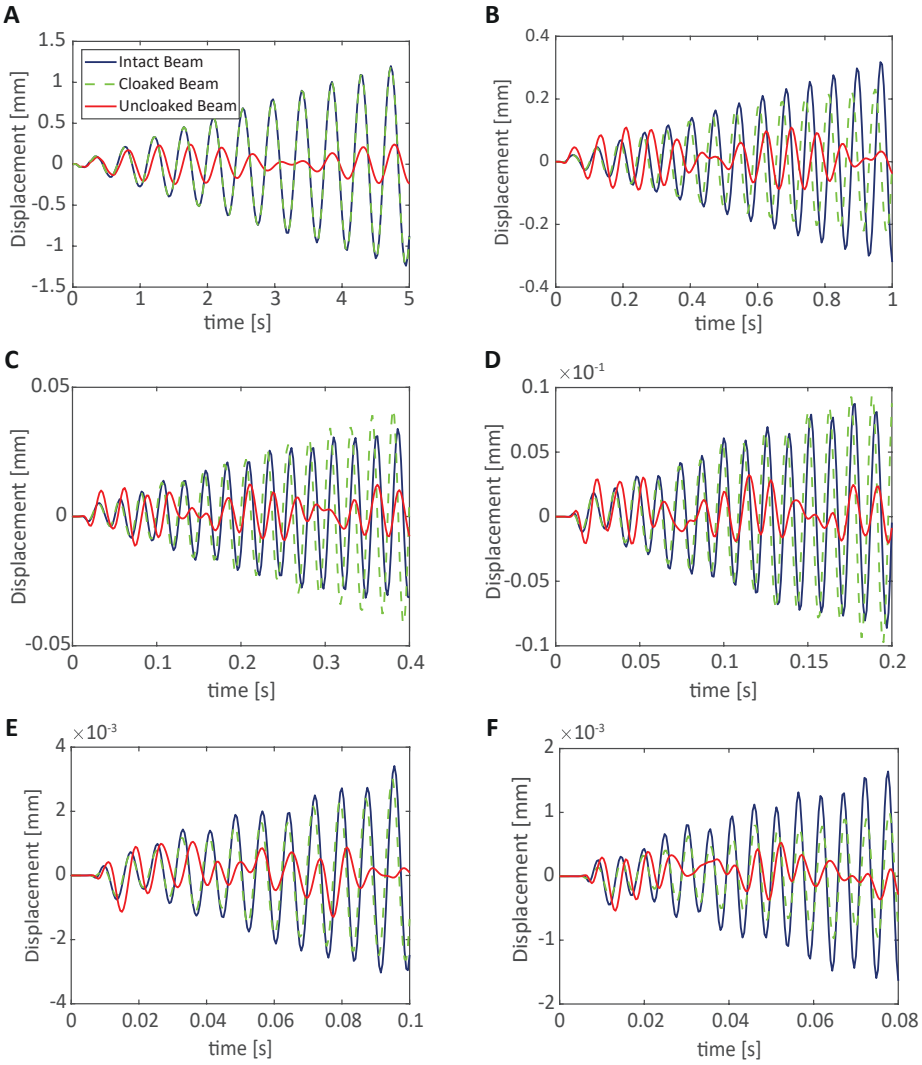


Figure S6: Displacement time series at the beam tip for the intact, cloaked, and uncloaked configurations obtained from finite-element simulations under single-sine harmonic excitation at (A) 2.3 Hz, (B) 14.3 Hz, (C) 40 Hz, (D) 78.4 Hz, (E) 129.5 Hz, and (F) 191.5 Hz.

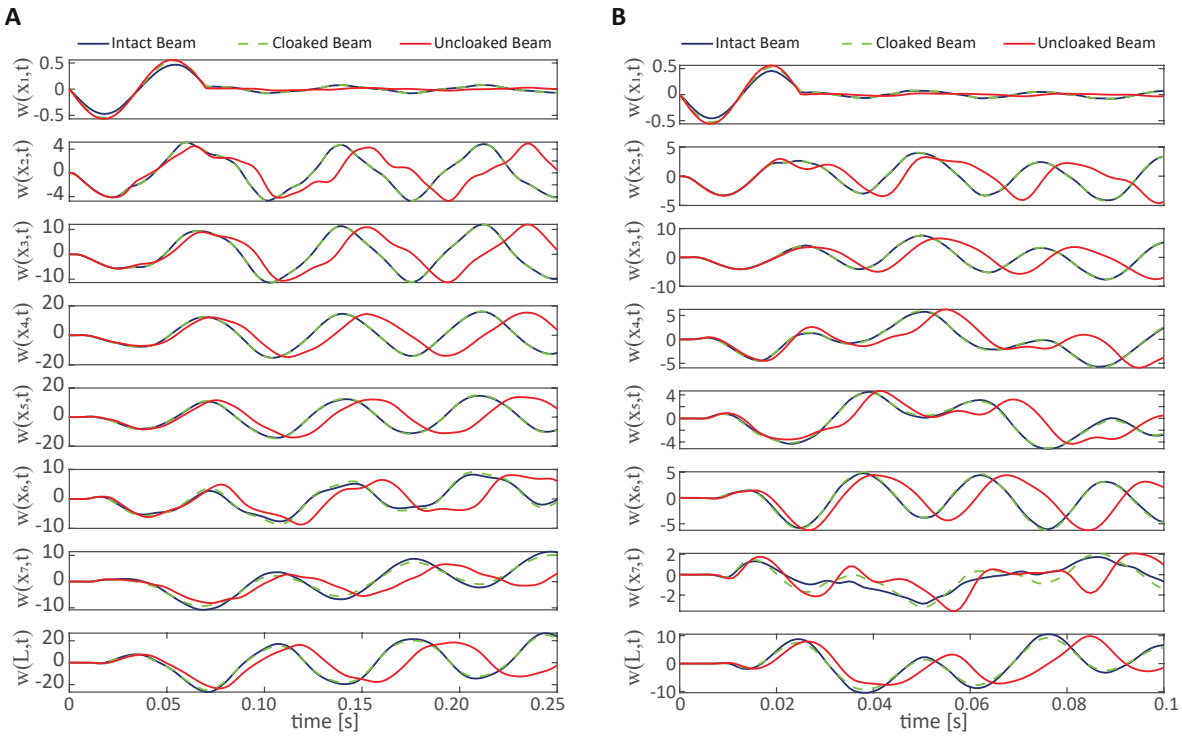


Figure S7: Displacement time series at various locations along the beam in response to pulse excitation, obtained from finite-element simulations for the intact, cloaked, and uncloaked configurations at (A) 14.3 Hz and (B) 40 Hz. $w(x_j,t)$ denotes the displacement at position x_j, where the j-th resonator is placed, and $w(L,t)$ denotes the displacement at the beam tip.

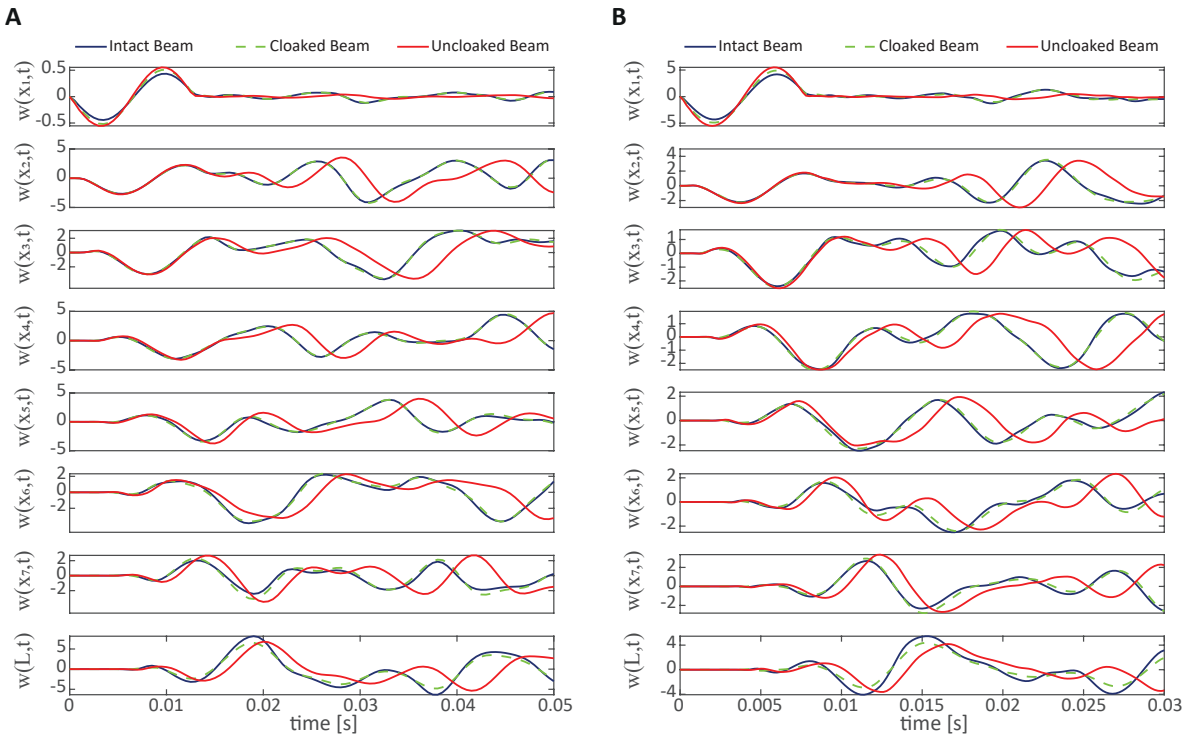
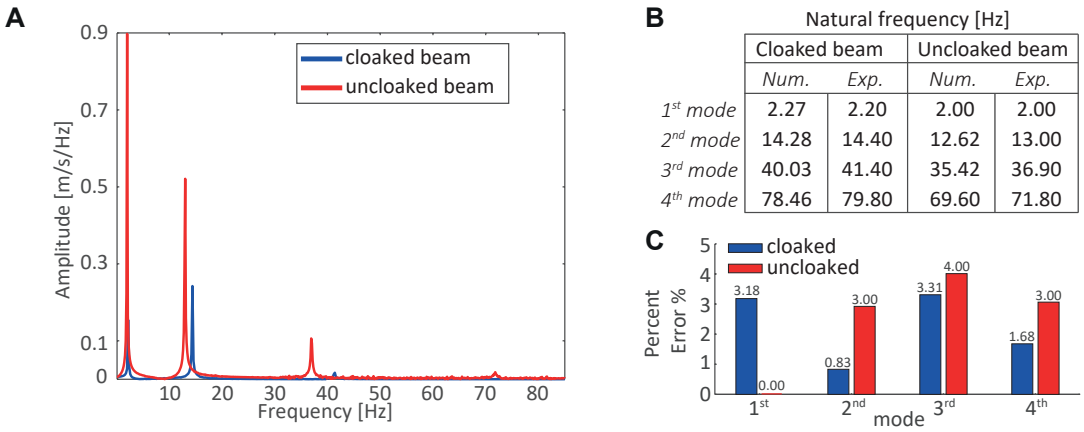


Figure S8: Displacement time series at various locations along the beam in response to pulse excitation, obtained from finite-element simulations for the intact, cloaked, and uncloaked configurations at (A) 78.4 Hz and (B) 129.5 Hz. $w(x_j,t)$ denotes the displacement at position x_j, where the j-th resonator is placed, and $w(L,t)$ denotes the displacement at the beam tip.



Natural frequency [Hz]	Cloaked beam		Uncloaked beam	
	Num.	*Exp.*	*Num.*	*Exp.*
1st mode	2.27	2.20	2.00	2.00
2nd mode	14.28	14.40	12.62	13.00
3rd mode	40.03	41.40	35.42	36.90
4th mode	78.46	79.80	69.60	71.80

Figure S9: Experimental validation of the cloaking design. (A) Fast Fourier Transform of the velocity measured on the tip of the beam for the cloaked and uncloaked beams under free vibration. (B) Comparison between the natural frequencies in Hz obtained from the experiment and the numerical results. (C) Percent error between the numerical and experimental natural frequencies of the cloaked and uncloaked beams.

natural frequency values. Figure S9B shows a comparison between the experimental and numerical results of the uncloaked and cloaked beams. The experimental frequencies align closely with those obtained from finite-element simulations, as confirmed by the percentage error shown in Fig. S9C. These findings demonstrate the reliability of the experimental and numerical methods.

Scattering Reduction Coefficient for the Plate

To explore the efficacy of cloaking in scenarios where flexural and torsional modes are strongly coupled, we use a plate model. The same finite-element analysis is conducted for a plate, but considering a plate of dimensions $750 \times 500 \times 2$ mm^3 with nine rectangular voids of dimensions 118×30 mm^2, as shown in Fig. S10. One end of the plate is clamped, while the opposite end is free to vibrate. The structure is excited by sinusoidal base excitation with null rotation. The SRCs are calculated for frequencies ranging from 0 to 260 Hz, exploring a broader band compared to the beam case. The results are shown in Fig. S10 and reported in Tab. S3. The plate study shows substantial scattering reduction and improved recovery of the intact natural frequencies in a more complex flexural-torsional field, with cloaked frequencies differing by less than 4.1% over the tested range. The eigenmodes at different specific frequencies involving flexural and torsional vibrations are reported in Fig. S10C for the intact plate, cloaked plate, and uncloaked plate. The cloaked plate behaves almost identically to the intact plate at these frequencies, while the uncloaked plate displays significant differences.

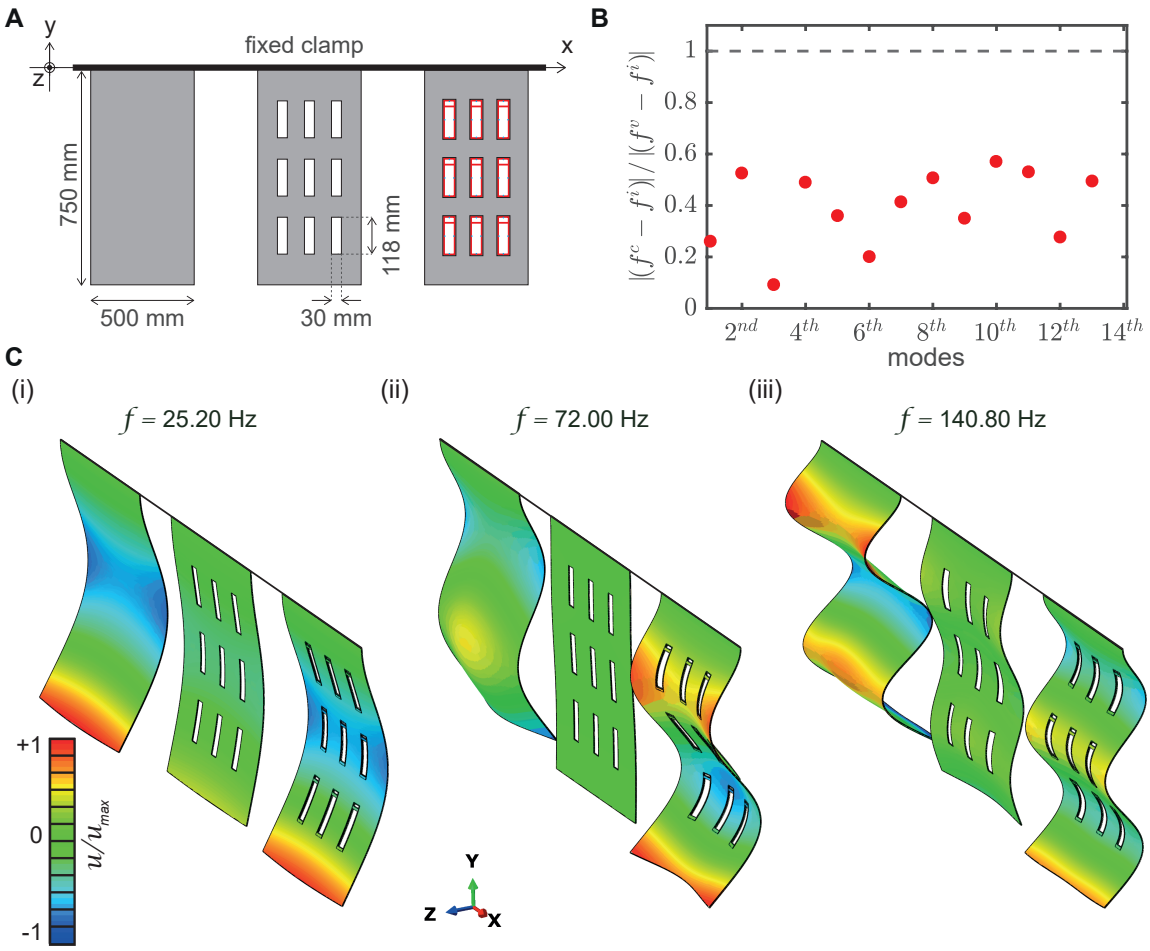


Figure S10: Finite-element simulation results of the cloaking performance of a plate with nine rectangular voids showing coupled flexural and torsional modes. (A) Setup of intact, uncloaked, and cloaked plates. One end of the plates is clamped, while the other end is free to vibrate. A sinusoidal base excitation with null rotation is applied along the z-axis. (B) Illustration of the Scattering Reduction Coefficient (SRC) for frequencies ranging from 0 to 260 Hz. (C) Eigenmodes of the intact plate (on the left), the uncloaked plate (in the middle), and the cloaked plate (on the right) for different frequencies (i) 25.20 Hz, (ii) 72.00 Hz, and (iii) 140.80 Hz.

mode	Intact plate	Uncloaked plate	Cloaked plate	SRC
1	4.04 Hz	3.94 Hz	4.02 Hz	0.2629
2	13.64 Hz	13.12 Hz	13.37 Hz	0.5278
3	25.12 Hz	24.66 Hz	25.16 Hz	0.0943
4	46.10 Hz	44.40 Hz	45.27 Hz	0.4918
5	62.60 Hz	53.49 Hz	59.33 Hz	0.3596
6	72.16 Hz	69.63 Hz	71.65 Hz	0.2014
7	94.29 Hz	91.11 Hz	92.97 Hz	0.4139
8	100.27 Hz	91.32 Hz	95.71 Hz	0.5097
9	142.36 Hz	136.37 Hz	140.26 Hz	0.3506
10	158.06 Hz	146.80 Hz	151.63 Hz	0.5710
11	201.00 Hz	175.05 Hz	187.24 Hz	0.5303
12	232.09 Hz	227.00 Hz	233.50 Hz	0.2770
13	256.14 Hz	249.05 Hz	252.64 Hz	0.4937

Table S3: Natural frequencies for the cantilever plate under intact, cloaked, and uncloaked conditions. The scattering reduction coefficients (SRC) for each mode are also displayed.

Scattering Measure from Displacement Field Analysis

To further evaluate the effectiveness of the cloak in reducing scattering, we compute the scattering measure directly from the displacement fields, following the approach proposed in (*15*). The scattering measure is defined as

$$\boxed{\varepsilon(u_1, u_2, \mathcal{R}) = \left(\int_{\mathcal{R}} |u_1(\mathbf{x}) - u_2(\mathbf{x})|^2 \, \mathrm{d}\mathbf{x}\right) \left(\int_{\mathcal{R}} |u_2(\mathbf{x})|^2 \, \mathrm{d}\mathbf{x}\right)^{-1}} \tag{S13}$$

where $\mathcal{R} \in \mathbb{R}^2$ represents a region outside the cloak, and $u_1(\mathbf{x})$ and $u_2(\mathbf{x})$ are displacement fields used for comparison.

The scattering is evaluated for two cases, $\varepsilon(u_u, u_i, \mathcal{R})$ and $\varepsilon(u_c, u_i, \mathcal{R})$, where u_c is the displacement field of the cloaked beam, u_u is that of the uncloaked beam, and u_i is that of the intact beam. A perfectly cloaked structure corresponds to $\varepsilon \to 0$, indicating that the scattered field is nearly identical to that of the intact beam.

To provide a normalized measure of the cloaking performance, we also compute the relative scattering reduction Q, defined as

$$\boxed{Q = \frac{|\varepsilon(u_u, u_i, \mathcal{R}) - \varepsilon(u_c, u_i, \mathcal{R})|}{\varepsilon(u_u, u_i, \mathcal{R})}.} \tag{S14}$$

A value of Q close to 1 indicates a strong reduction of scattering.

For the numerical evaluation, seven regions are defined in the forward scattering area of the beam, as illustrated in Fig. S11A. The displacement fields are obtained from finite-element simulations performed in ABAQUS. Within each region, 24 uniformly distributed points are selected to extract the displacement time series. The analysis is conducted considering an out-of-plane base excitation over a wide frequency range, from 2.2 Hz to 129 Hz, to capture different dynamic responses.

Figure S11B presents the computed scattering measures and parameter Q. The results show that, across all seven regions, the cloaked beam exhibits substantially smaller scattering values compared with the uncloaked beam, yielding a relative reduction Q close to 1. These findings confirm that the proposed cloak effectively suppresses wave scattering and restores intact wave propagation through the metastructure.

Impact of Elastic Invisibility on Energy Concentration and Energy Harvesting Potential

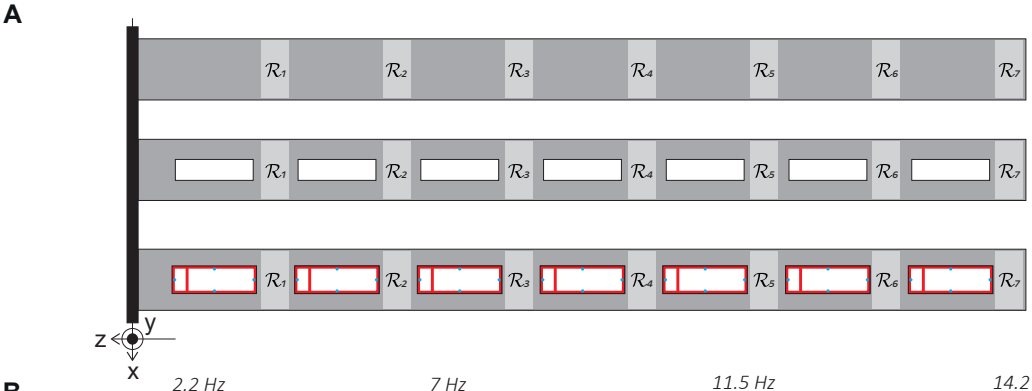
Subsequently, we investigate the role of scattering reduction in enhancing the energy harvesting performance of the metastructure. When scattering is minimized, less mechanical energy is lost through the cloaked voids, allowing a greater portion of the incident energy to be concentrated within the local resonators. In this work, these resonators are later engineered to also operate as energy harvesters, enabling the conversion of the concentrated vibrational energy into electrical power. Thus, reducing scattering increases the mechanical energy available to the embedded resonators and, consequently, their energy harvesting potential.

To demonstrate this effect, finite-element simulations were conducted in ABAQUS for both uncloaked and cloaked beams containing identical fixed–free resonators embedded within the seven voids, as shown in Fig. S12A. Each resonator, made of carbon fiber with dimensions of $85\times24\times0.26$ mm^3, was designed to exhibit a fundamental frequency of 40 Hz. A base excitation at 40 Hz was applied to induce local resonance, enabling the evaluation of energy absorption by the resonators. The velocity at each resonator tip was extracted from the simulations and used to compute the kinetic energy, serving as an indicator of the potential for harvested energy.

Figure S12B presents the kinetic energy of the seven resonators for both the uncloaked and cloaked metastructures. In both cases, the kinetic energy gradually decreases as the resonators are positioned farther from the base of the host beam. This behavior arises from the local resonance condition, in which the propagating wave is progressively attenuated as its energy is absorbed by the resonators, leading to a diminished wave amplitude toward the beam tip.

When comparing the two configurations, overall, the resonators in the cloaked metastructure consistently exhibit higher kinetic energy than those in the uncloaked beam. Over a short excitation period of 1 s, the total kinetic energy of the resonators in the cloaked system is approximately 7% greater than in the uncloaked case, demonstrating that the cloaking mechanism enhances the

A



B

	2.2 Hz			7 Hz			11.5 Hz			14.2 Hz		
	Uncloaked	Cloaked	Q	Uncloaked	Cloaked	Q	Uncloaked	Cloaked	Q	Uncloaked	Cloaked	Q
$\mathcal{R}_1$	0.3167	5.019×10^{-4}	0.9984	0.5129	7.808×10^{-4}	0.9985	4.7661	8.140×10^{-4}	0.9998	1.2990	8.659×10^{-4}	0.9993
$\mathcal{R}_2$	0.4018	3.824×10^{-4}	0.9990	1.4286	1.039×10^{-3}	0.9993	9.1630	1.254×10^{-3}	0.9999	1.2796	1.001×10^{-3}	0.9992
$\mathcal{R}_3$	0.4282	5.717×10^{-4}	0.9987	2.3293	1.233×10^{-3}	0.9995	11.9235	1.479×10^{-3}	0.9999	1.2682	7.855×10^{-4}	0.9994
$\mathcal{R}_4$	0.4399	6.509×10^{-4}	0.9985	3.1683	2.295×10^{-3}	0.9993	14.4662	2.346×10^{-3}	0.9998	1.2674	6.038×10^{-4}	0.9995
$\mathcal{R}_5$	0.4468	6.862×10^{-4}	0.9985	1.8473	1.334×10^{-2}	0.9928	21.6120	2.886×10^{-2}	0.9987	1.2982	1.730×10^{-2}	0.9867
$\mathcal{R}_6$	0.4517	6.874×10^{-4}	0.9985	0.3075	1.110×10^{-2}	0.9639	4.4250	4.147×10^{-2}	0.9906	1.1896	6.711×10^{-2}	0.9436
$\mathcal{R}_7$	0.4554	6.841×10^{-4}	0.9985	0.9476	6.387×10^{-3}	0.9933	9.1302	9.798×10^{-3}	0.9989	1.2288	1.214×10^{-2}	0.9901

	20 Hz			37 Hz			40 Hz			54 Hz		
	Uncloaked	Cloaked	Q	Uncloaked	Cloaked	Q	Uncloaked	Cloaked	Q	Uncloaked	Cloaked	Q
$\mathcal{R}_1$	0.5624	2.194×10^{-3}	0.9961	1.4449	4.163×10^{-4}	0.9997	1.0230	5.522×10^{-4}	0.9995	1.9162	7.699×10^{-3}	0.9960
$\mathcal{R}_2$	2.1133	3.056×10^{-3}	0.9986	1.6925	4.737×10^{-4}	0.9997	0.8493	8.129×10^{-4}	0.9990	2.0985	3.247×10^{-3}	0.9985
$\mathcal{R}_3$	1.0179	2.396×10^{-3}	0.9976	2.0224	2.995×10^{-3}	0.9985	0.7123	1.270×10^{-3}	0.9982	0.5686	2.447×10^{-3}	0.9957
$\mathcal{R}_4$	0.5714	1.102×10^{-3}	0.9981	1.4215	1.446×10^{-2}	0.9898	0.9750	2.151×10^{-2}	0.9779	3.1364	3.334×10^{-2}	0.9894
$\mathcal{R}_5$	0.4673	6.498×10^{-3}	0.9861	1.7232	2.220×10^{-4}	0.9999	0.8161	4.446×10^{-4}	0.9995	0.8989	6.908×10^{-3}	0.9923
$\mathcal{R}_6$	1.3167	1.541×10^{-1}	0.8830	2.7417	5.210×10^{-1}	0.8100	0.6439	3.794×10^{-2}	0.9411	1.8165	8.236×10^{-2}	0.9547
$\mathcal{R}_7$	0.6331	1.676×10^{-2}	0.9735	1.5735	3.197×10^{-2}	0.9797	0.8427	3.593×10^{-2}	0.9574	0.8520	4.901×10^{-2}	0.9425

	68 Hz			78.4 Hz			98 Hz			129 Hz		
	Uncloaked	Cloaked	Q	Uncloaked	Cloaked	Q	Uncloaked	Cloaked	Q	Uncloaked	Cloaked	Q
$\mathcal{R}_1$	5.6602	2.929×10^{-3}	0.9995	0.7441	4.643×10^{-3}	0.9938	6.3470	7.297×10^{-2}	0.9885	0.8429	1.060×10^{-2}	0.9874
$\mathcal{R}_2$	16.0042	7.197×10^{-3}	0.9996	0.6954	6.367×10^{-3}	0.9908	0.4472	4.110×10^{-2}	0.9081	0.8944	1.130×10^{-1}	0.8737
$\mathcal{R}_3$	4.0651	3.901×10^{-3}	0.9990	0.8169	1.108×10^{-2}	0.9864	6.5139	9.532×10^{-2}	0.9854	0.8064	1.752×10^{-2}	0.9783
$\mathcal{R}_4$	11.2756	1.062×10^{-2}	0.9991	0.8585	7.722×10^{-3}	0.9910	1.5785	4.075×10^{-2}	0.9742	0.7668	3.196×10^{-2}	0.9583
$\mathcal{R}_5$	3.8834	1.939×10^{-2}	0.9950	0.8238	3.192×10^{-2}	0.9613	3.0537	2.063×10^{-1}	0.9324	1.8598	2.995×10^{-1}	0.8389
$\mathcal{R}_6$	9.7877	3.656×10^{-2}	0.9963	0.9720	2.357×10^{-2}	0.9758	3.5702	6.052×10^{-2}	0.9830	0.8393	1.178×10^{-2}	0.9860
$\mathcal{R}_7$	4.3410	6.241×10^{-2}	0.9856	0.8031	7.268×10^{-2}	0.9095	1.4384	1.059×10^{-1}	0.9264	0.7728	1.414×10^{-1}	0.8171

Figure S11: Scattering wave analysis for the uncloaked and cloaked beams evaluated across seven regions over a range of incident wave frequencies. (A) Intact, uncloaked, and cloaked beams showing the seven regions (R_i) considered in the analysis. (B) Scattering measures for the uncloaked and cloaked beams and their corresponding relative reduction Q.

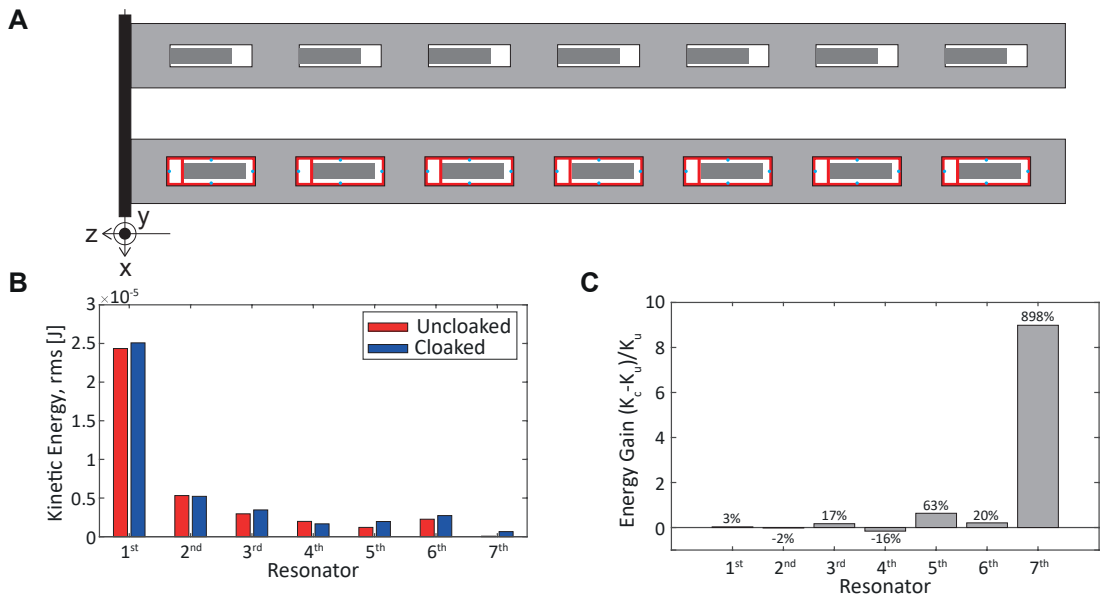


Figure S12: Effect of scattering reduction on energy concentration within the resonators. (A) Finite element model of the uncloaked and cloaked beams containing seven identical resonators embedded within the voids. (B) Root mean square (RMS) kinetic energy of the resonator tips for the uncloaked and cloaked metastructures under base excitation at 40 Hz. (C) Energy gain of each resonator, where K_c and K_u denote the kinetic energies for the cloaked and uncloaked systems, respectively.

concentration of vibrational energy within the resonators.

Figure S12C quantifies this improvement by showing the energy gain for each resonator. The relative gain is most significant for resonators located near the beam tip, where scattering effects are typically more pronounced. This behavior confirms that the cloaking mechanism mitigates energy losses through the voids, allowing a greater portion of the incident energy to be retained and transferred to the resonators.

Overall, these results demonstrate that the cloaking not only reduces scattering but also enhances the concentration of mechanical energy within the resonators, thereby improving the power generation potential of the metastructure.

Figure S13 shows the time-series displacement at the tip of each resonator for both configurations. The results clearly indicate that the resonators in the cloaked system exhibit larger vibration amplitudes compared to those in the uncloaked beam, particularly for the 5th, 6th, and 7th resonators located near the beam tip. This enhancement is primarily attributed to the reduced scattering achieved by the cloak, which reduces void-induced scattering and enables a greater concentration of vibrational energy within the resonators.

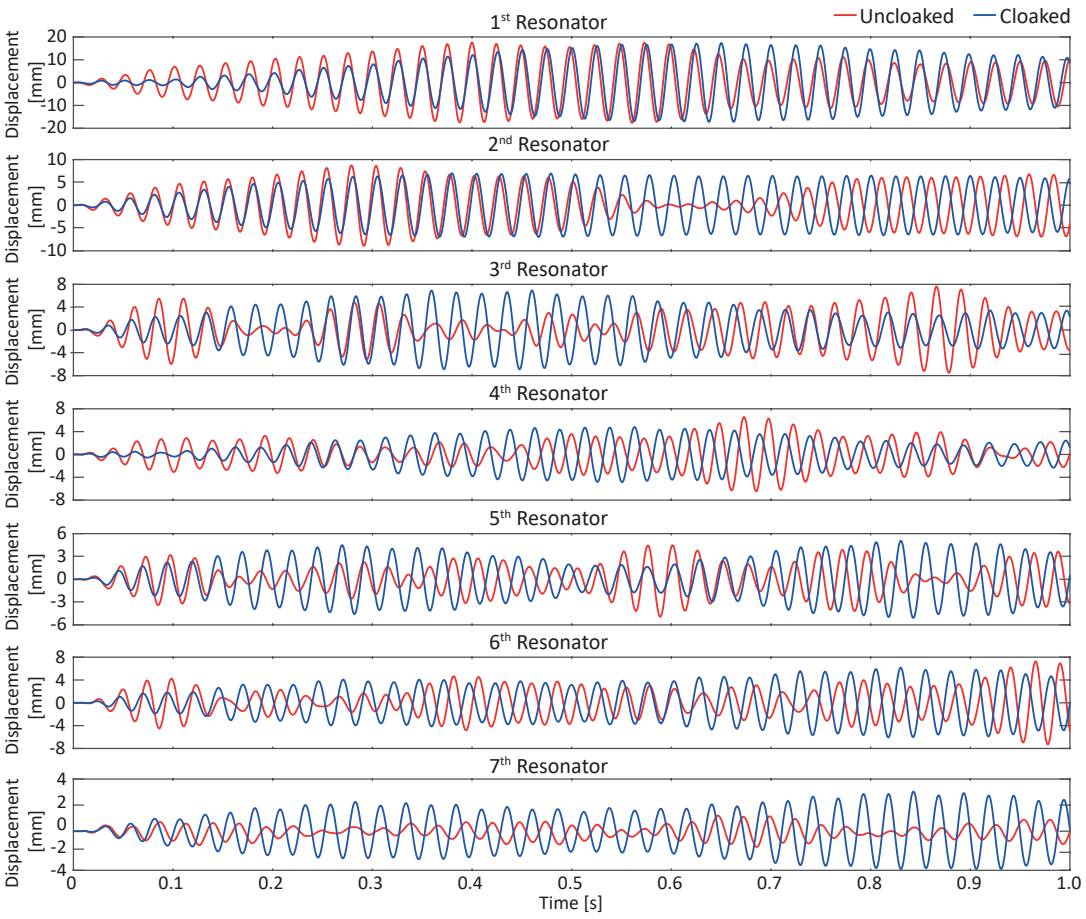


Figure S13: Time-series displacement responses of the resonator tips for the uncloaked and cloaked systems, obtained from finite-element simulations under base excitation at 40 Hz.

Metabeam with magneto-elastic piezoelectric resonators

The proposed metastructure is designed based on the local-resonance phenomenon. Locally resonant attenuation arises when the embedded resonators interact out of phase with the host motion near their resonance, producing frequency-dependent reaction forces that reduce vibration transmission through the beam. In this frequency range, part of the incident mechanical energy is localized in the resonators rather than transmitted along the host structure. The piezoelectric layers then convert part of this localized mechanical energy into electrical energy.

We design the resonator as a magneto-elastic piezoelectric cantilever beam, utilizing piezoelectric patches to convert kinetic energy into electrical energy. Piezoelectric transduction was selected because its thin patches can be symmetrically integrated within the reconstructed bay without altering the magnetic interactions that define the nonlinear potential. Although electromagnetic or hybrid transduction mechanisms could yield higher power output under specific operating conditions, implementing them would necessitate a complete redesign of both the elastic-invisibility strategy and the magnetic interaction due to their additional mass and induced flux variations. The magneto-elastic interaction is produced by a permanent magnet attached to the resonator tip and a second permanent magnet fixed in front of it. It introduces an intentional nonlinearity and allows us to control the restoring force of the resonator. In the following, we describe the nonlinear magnetic interaction force between the magnets, the mathematical background of the equation of motion of the metabeam, and numerical results to demonstrate the capability of vibration suppression and energy harvesting of the metastructure.

Nonlinear magnetic force

Nonlinearity is intentionally introduced into each resonator by placing two permanent magnets in a repulsive configuration. For the j-th resonator, magnet A is attached to the resonator tip, whereas magnet B is fixed to the rigid base near the free end of the resonator, as shown in Fig. S14. The magnets are positioned with the poles facing each other, producing a repulsive magnetic interaction that modifies the restoring force of the resonator.

The magnitude of the magnetic interaction depends on the magnetic moments of the two magnets and on the center-to-center distance between them. For the j-th resonator, this distance is denoted by $r_j = |\mathbf{r}_j|$, where $\mathbf{r}_j$ is the vector connecting the two dipole centers. As r_j decreases, the repulsive magnetic interaction increases. Following the dipole-dipole formulation (*16–18*), the magnetic flux density generated by magnet B at magnet A is written as

$$\mathbf{B}_{BA,j} = -\frac{\mu_0}{4\pi}\nabla\left(\frac{\boldsymbol{\mu}_B \cdot \mathbf{r}_j}{r_j^3}\right), \tag{S15}$$

where μ_0 is the vacuum permeability, and $\boldsymbol{\mu}_B$ is the magnetic moment of dipole B. The correspond-

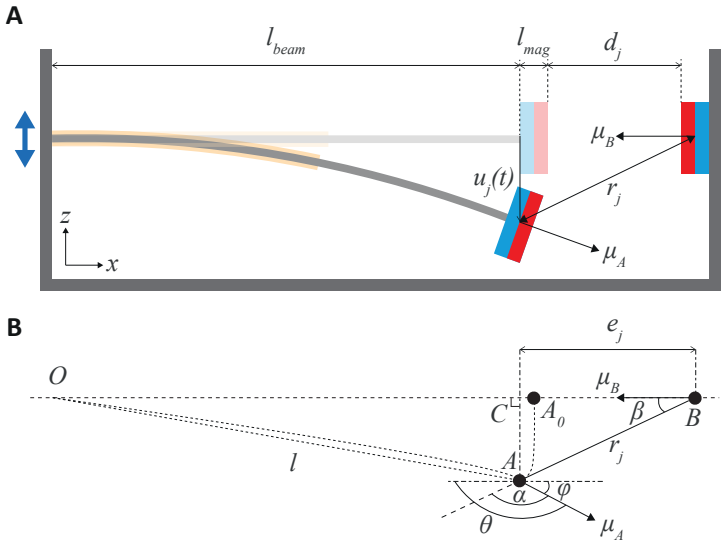


Figure S14: Nonlinear magneto-elastic piezoelectric resonator beam. The system consists of the j-th piezoelectric cantilever resonator of length l_{beam}, with piezoelectric patches bonded to both surfaces near the clamped region. Magnet A is attached to the resonator tip, and magnet B is fixed to the rigid base. The two magnets are positioned with approximately collinear magnetization axes and with equal polarity faces opposing each other, producing a repulsive magnetic interaction. (A) Illustration of the nonlinear magneto-elastic piezoelectric resonator. The light gray beam represents the undeformed configuration. (B) Geometric model used to derive the magnetic force. The fixed end of the resonator is denoted by O. Point A is the center of magnet A in the deformed configuration, and A_0 is its position in the undeformed configuration. Point C is the projection of A onto the horizontal direction, and point B is the center of magnet B. The quantities $u_j(t)$, d_j, e_j, and r_j denote the transverse tip displacement, prescribed magnet spacing, horizontal dipole separation, and center-to-center dipole distance of the j-th resonator, respectively.

ing magnetic potential energy is

$$U_{m,j} = -\mathbf{B}_{BA,j} \cdot \boldsymbol{\mu}_A = \frac{\mu_0}{4\pi} \nabla \left(\frac{\boldsymbol{\mu}_B \cdot \mathbf{r}_j}{r_j^3} \right) \cdot \boldsymbol{\mu}_A, \tag{S16}$$

where $\boldsymbol{\mu}_A$ is the magnetic moment of dipole A. The magnetic force acting on dipole A due to dipole B is obtained from

$$\mathbf{F}_{B_j} = -\nabla U_{m,j}. \tag{S17}$$

The resulting dipole-dipole interaction force can be expressed as

$$\mathbf{F}_{B_j} = \frac{3\mu_0 \mu_A \mu_B}{4\pi r_j^4} \left[\hat{\mathbf{r}}_j \left(\hat{\boldsymbol{\mu}}_A \cdot \hat{\boldsymbol{\mu}}_B \right) + \hat{\boldsymbol{\mu}}_B \left(\hat{\boldsymbol{\mu}}_A \cdot \hat{\mathbf{r}}_j \right) + \hat{\boldsymbol{\mu}}_A \left(\hat{\boldsymbol{\mu}}_B \cdot \hat{\mathbf{r}}_j \right) - 5\hat{\mathbf{r}}_j \left(\hat{\boldsymbol{\mu}}_A \cdot \hat{\mathbf{r}}_j \right) \left(\hat{\boldsymbol{\mu}}_B \cdot \hat{\mathbf{r}}_j \right) \right], \tag{S18}$$

where $\hat{\mathbf{r}}_j$, $\hat{\boldsymbol{\mu}}_A$, and $\hat{\boldsymbol{\mu}}_B$ are unit vectors in the directions of $\mathbf{r}_j$, $\boldsymbol{\mu}_A$, and $\boldsymbol{\mu}_B$, respectively, and $\mu_A = |\boldsymbol{\mu}_A|$, $\mu_B = |\boldsymbol{\mu}_B|$.

The dot products in Eq. S18 are evaluated using the geometric relations shown in Fig. S14. For the j-th resonator, the force can be written as

$$\mathbf{F}_{B_j} = \frac{3\mu_0 \mu_A \mu_B}{4\pi r_j^4} \left(\hat{\mathbf{r}}_j \cos\theta + \hat{\boldsymbol{\mu}}_B \cos\alpha + \hat{\boldsymbol{\mu}}_A \cos\beta - 5\hat{\mathbf{r}}_j \cos\alpha \cos\beta \right). \tag{S19}$$

Here, α, β and θ are the angles defined in Fig. S14B.

In the reduced-order model, the magnets are represented by equivalent magnetic dipoles. The flexural dynamics of the j-th resonator are described by the transverse displacement $u_j(t)$, and only the magnetic-force component projected along the z-direction is retained in the equation of motion. The axial component of the magnetic interaction is not included as an independent degree of freedom in this transverse model. The nonlinear geometric dependence of the magnetic interaction is retained through the displacement-dependent horizontal separation $e_j(u_j)$ and the center-to-center distance $r_j(u_j)$. With these definitions, the transverse magnetic force acting on the j-th resonator is written as

$$F_{B_{j,z}}(u_j) = \frac{3\mu_0 \mu_A \mu_B}{4\pi {r_j}^4} \left[(\cos\theta - 5\cos\alpha\cos\beta)\sin\beta + \cos\beta\sin\varphi \right]. \tag{S20}$$

Based on the geometry in Fig. S14B, the effective distance from the clamp to the center of magnet A is

$$l = OA = l_{beam} + \frac{l_{mag}}{2}. \tag{S21}$$

The displacement-dependent horizontal separation between the dipole centers is

$$e_j(u_j) = BC = d + l_{\text{mag}} + l\,(1 - \cos\varphi), \tag{S22}$$

and the center-to-center distance between the dipoles is

$$r_j(u_j) = AB = \sqrt{u_j(t)^2 + e_j(u_j)^2}. \tag{S23}$$

For compactness, we write $e_j = e_j(u_j)$ and $r_j = r_j(u_j)$ in the following expressions. The corresponding trigonometric relations are

$$\sin\theta = \sin\varphi = \frac{AC}{OA} = \frac{u_j(t)}{l} \tag{S24}$$

$$\cos\theta = -\cos\varphi = -\frac{1}{l}\sqrt{l^2 - u_j(t)^2} \tag{S25}$$

$$\cos\beta = \frac{AC}{AB} = \frac{e_j}{r_j} \tag{S26}$$

$$\sin\beta = \frac{BC}{AB} = \frac{u_j(t)}{r_j} \tag{S27}$$

$$\cos\alpha = \cos(\theta - \beta) = \cos\theta\cos\beta + \sin\theta\sin\beta = \frac{1}{l\, r_j}\left(u_j(t)^2 - e_j\sqrt{l^2 - u_j(t)^2}\right). \tag{S28}$$

Finally, by substituting these geometric relations into Eq. S20, the magnetic force in the z-direction is obtained as

$$\boxed{F_{B_{j,z}}\left(u_j(t)\right) = \frac{3\mu_0\mu_A\mu_B u_j(t)}{4\pi r_j^5 l}\left[e_j - \sqrt{l^2 - u_j(t)^2} - \frac{5e_j}{r_j^2}\left(u_j(t)^2 - e_j\sqrt{l^2 - u_j(t)^2}\right)\right].} \tag{S29}$$

Governing equations of the metabeam

Owing to the elastic reconstruction of the voids, the metabeam is modeled as an effectively continuous cantilever beam coupled to discrete nonlinear electromechanical oscillators at positions x_j. A schematic illustration of the metabeam is shown in Fig. S15.

The cantilever beam is subjected to base-motion excitation. The total transverse displacement $\mathrm{w}_t(x,t)$ is defined as

$$\mathrm{w}_t(x,t) = \mathrm{w}_b(t) + \mathrm{w}(x,t), \tag{S30}$$

where $\mathrm{w}_b(t)$ is the base displacement, and $\mathrm{w}(x,t)$ is the transverse displacement of the beam relative to the base.

The host beam is modeled using Euler–Bernoulli beam theory with viscous damping (*14*). The interaction between the host beam and the j-th resonator is introduced through the reaction force exerted at x_j. The governing equations are

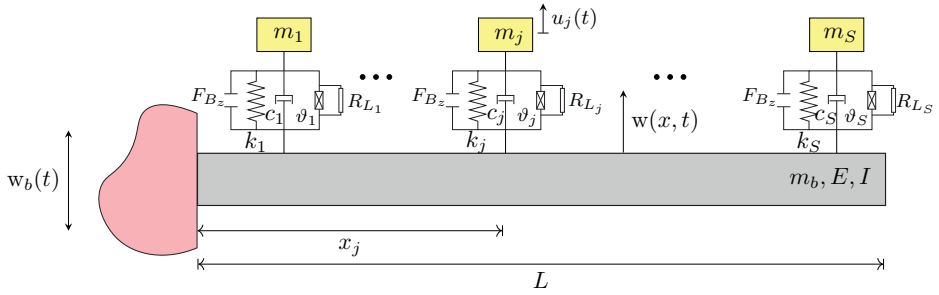


Figure S15: Schematic illustration of the metastructure based on a cantilever beam with embedded magneto-elastic piezoelectric resonators.

$$\boxed{\begin{aligned} &m_b \frac{\partial^2 \mathrm{w}}{\partial t^2}(x,t) + c\frac{\partial \mathrm{w}}{\partial t}(x,t) + EI\frac{\partial^4 \mathrm{w}}{\partial x^4}(x,t) \\ &\quad - \sum_{j=1}^{S} \left(c_j \dot{u}_j(t) + k_j u_j(t) - F_{B_{j,z}}(u_j(t)) - \vartheta_j v_j(t) \right) \delta(x - x_j) = -m_b \ddot{\mathrm{w}}_b(t) \end{aligned}} \tag{S31}$$

$$\boxed{\begin{aligned} &m_j \ddot{u}_j(t) + c_j \dot{u}_j(t) + k_j u_j(t) - F_{B_{j,z}}(u_j(t)) - \vartheta_j v_j(t) \\ &= -m_j \left[\frac{\partial^2 \mathrm{w}}{\partial t^2}(x_j,t) + \ddot{\mathrm{w}}_b(t) \right], \quad j = 1, 2, \ldots, S \end{aligned}} \tag{S32}$$

$$\boxed{C_{p,j} \dot{v}_j(t) + \mathcal{Y}_j v_j(t) + \vartheta_j \dot{u}_j(t) = 0, \quad j = 1, 2, \ldots, S} \tag{S33}$$

where $\delta(\cdot)$ denotes the Dirac delta function; $u_j(t)$ and $v_j(t)$ are the relative transverse displacement and voltage of the j-th resonator, respectively; x_j is the resonator position along the beam; m_b, c and EI are the mass per unit length, the damping coefficient and the flexural rigidity of the host beam, respectively; m_j, c_j and k_j are the mass, damping coefficient and the linear stiffness of the j-th resonator, respectively; $F_{B_{j,z}}$ is the transverse magnetic force; ϑ_j is the electromechanical coupling coefficient; $C_{p,j}$ is the equivalent piezoelectric capacitance; $\mathcal{Y}_j = 1/R_L$ is the load admittance; and S is the total number of resonators.

The clamped-free boundary conditions of the host beam are

$$\mathrm{w}(0,t) = 0, \qquad \frac{\partial \mathrm{w}(0,t)}{\partial x} = 0, \qquad EI\frac{\partial^2 \mathrm{w}(L,t)}{\partial x^2} = 0, \qquad \text{and} \qquad EI\frac{\partial^3 \mathrm{w}(L,t)}{\partial x^3} = 0. \tag{S34}$$

The relative displacement of the host beam is approximated through a Galerkin expansion using the mass-normalized mode shapes $\phi_r(x)$ of the cantilever beam without resonators,

$$\mathrm{w}(x,t) \approx \sum_{r=1}^{N} \eta_r(t) \phi_r(x), \tag{S35}$$

where N is the number of modes in the expansion, and $\eta_r(t)$ is the r-th modal coordinate. We neglect the nonlinear modal interactions because the modes of the beam are well-separated. The normalized mass modal shapes of the beam are given by the following equation

$$\phi_r(x) = \frac{1}{\sqrt{m_b L}}\left[\cos\left(\frac{\lambda_r x}{L}\right) - \cosh\left(\frac{\lambda_r x}{L}\right) + \frac{\sin\lambda_r - \sinh\lambda_r}{\cos\lambda_r + \cosh\lambda_r}\left(\sin\left(\frac{\lambda_r x}{L}\right) - \sinh\left(\frac{\lambda_r x}{L}\right)\right)\right], \quad \text{(S36)}$$

where λ_r is the r-th positive real solution of the characteristic equation for the cantilever beam given by

$$\cos\lambda\cosh\lambda + 1 = 0. \quad \text{(S37)}$$

The mode shapes satisfy the orthogonality conditions

$$\begin{aligned} \int_{x=0}^{x=L} \phi_r(x) m_b \phi_s(x) dx &= \delta_{r,s}, \qquad r,s = 1,2,\ldots \\ \int_{x=0}^{x=L} \phi_r(x) EI \phi_s''''(x) dx &= \omega_r^2 \delta_{r,s}, \qquad r,s = 1,2,\ldots \end{aligned} \quad \text{(S38)}$$

where δ_{rs} is the Kronecker delta. The natural frequencies are

$$\omega_r = \lambda_r^2 \sqrt{\left(\frac{EI}{\rho A L^4}\right)}. \quad \text{(S39)}$$

After substituting Eq. S35 into the coupled beam–resonator equations Eqs. S31 and S32 and rearranging the resonator reaction forces, the modal equations can be written as

$$\boxed{\ddot{\eta}_r + 2\zeta_r\omega_r\dot{\eta}_r + \omega_r^2\eta_r - \sum_{j=1}^{S}\left[k_j u_j + c_j\dot{u}_j - F_{B_{j,z}}(u_j) - \vartheta_j v_j\right]\phi_r(x_j) = -m_b\ddot{\mathrm{w}}_b\int_{x=0}^{x=L}\phi_r(x)dx} \quad \text{(S40)}$$

$$\boxed{m_j\left[\sum_{r=1}^{N}\ddot{\eta}_r\phi_r(x_j) + \ddot{u}_j\right] + c_j\dot{u}_j + k_j u_j - F_{B_{j,z}}(u_j) - \vartheta_j v_j = -m_j\ddot{\mathrm{w}}_b(t), \quad j = 1,2,\ldots,\mathrm{S}.} \quad \text{(S41)}$$

Equations S40, S41, and S33 form a coupled electromechanical system composed of $N+S$ second-order mechanical equations and S first-order electrical equations.

The coupled mechanical and electrical equations can be expressed in a common second-order form by introducing an auxiliary electrical coordinate $\bar{v}_j(t)$ such that $\dot{\bar{v}}_j(t) = v_j(t)$. Accordingly, Eq. S33 can be written as

$$C_{p,j}\ddot{\bar{v}}_j(t) + Y_j\dot{\bar{v}}_j(t) + \vartheta_j\dot{u}_j(t) = 0. \tag{S42}$$

The coupled electromechanical system can then be expressed in matrix form as

$$\boxed{[\mathbf{M}]\,\ddot{\mathbf{Z}}(t) + [\mathbf{C}]\,\dot{\mathbf{Z}}(t) + [\mathbf{K}]\,\mathbf{Z}(t) = \mathbf{F}(t) + \mathbf{F}_{\mathrm{nl}}(\mathbf{Z}(t)),} \tag{S43}$$

where $\mathbf{Z}(t) = [\eta_1(t), \ldots, \eta_N(t), u_1(t), \ldots, u_S(t), \bar{v}_1(t), \ldots, \bar{v}_S(t)]^T$ contains the modal coordinates of the host beam, the relative displacements of the resonators, and the auxiliary electrical coordinates, respectively. The physical voltage across the load of the j-th resonator is recovered as $v_j(t) = \dot{\bar{v}}_j(t)$. The notation $(\dot{})$ denotes the first derivative with respect to time, and $(\ddot{})$ represents the second derivative with respect to time.

The system matrices are defined as

$$\begin{gathered}
[\mathbf{M}] = \begin{bmatrix} \mathbf{M_{11}} & \mathbf{M_{12}} & \mathbf{0} \\ \mathbf{M_{21}} & \mathbf{M_{22}} & \mathbf{0} \\ \mathbf{0} & \mathbf{0} & \mathbf{C}_p \end{bmatrix}, \quad [\mathbf{C}] = \begin{bmatrix} \mathbf{D_{11}} & \mathbf{0} & \mathbf{0} \\ \mathbf{0} & \mathbf{D_{22}} & -\mathbf{\Theta} \\ \mathbf{0} & \mathbf{\Theta} & \mathbf{Y} \end{bmatrix}, \\
[\mathbf{K}] = \begin{bmatrix} \mathbf{K_{11}} & \mathbf{0} & \mathbf{0} \\ \mathbf{0} & \mathbf{K_{22}} & \mathbf{0} \\ \mathbf{0} & \mathbf{0} & \mathbf{0} \end{bmatrix}, \mathbf{F_{nl}}(\mathbf{Z(t)}) = \begin{bmatrix} 0 \\ \mathbf{F_{B_z}} \\ 0 \end{bmatrix}, \quad \mathbf{F} = \begin{bmatrix} \mathbf{F_1} \\ \mathbf{F_2} \\ \mathbf{F_3} \end{bmatrix},
\end{gathered} \tag{S44}$$

where $\mathbf{M_{11}}$ is a N×N matrix, with the entries: $m_{mn} = \delta_{mn} + \sum_{j=1}^{S} m_j\phi_m(x_j)\phi_n(x_j)$; $\mathbf{M_{12}}$ is a N×S matrix, with the entries: $m_{mq} = m_q\phi_m(x_q)$; $\mathbf{M_{21}}$ is a S×N matrix, with the entries: $m_{pn} = m_p\phi_n(x_p)$; $\mathbf{M_{22}}$ is a S×S matrix, with the entries: $m_{pq} = \delta_{pq}m_p$; $\mathbf{C_p}$ is a S×S matrix, with the entries: $C_{pq} = \delta_{pq}C_p$; $\mathbf{K_{11}}$ is a N×N diagonal matrix, with the entries: $k_{mn} = \delta_{mn}\omega_m^2$; $\mathbf{K_{22}}$ is a S×S diagonal matrix, with the entries: $k_{pq} = \delta_{pq}k_p$; $\mathbf{D_{11}}$ is a NxN diagonal matrix, with the entries: $d_{mn} = \delta_{mn}2\zeta_m\omega_m$; $\mathbf{D_{22}}$ is a SxS diagonal matrix, with the entries: $d_{pq} = \delta_{pq}2\zeta_p\sqrt{k_p m_p}$; $\mathbf{\Theta}$ is a SxS diagonal matrix, with the entries: $\Theta_{pq} = \delta_{pq}\vartheta_p$; $\mathbf{Y}$ is a SxS diagonal matrix, with the entries: $Y_{pq} = \delta_{pq}\mathcal{Y}_p$; $\mathbf{F_{B_z}}$ is a Sx1 vector, with the entries: $f_{nl_p} = F_{B_{p,z}}(u_p(t))$; $\mathbf{F_1}$ is a Nx1 vector, with the entries $f_m = -\ddot{\mathrm{w}}_b(t)\left[\int_{x=0}^{x=L} m_b\phi_m(x)dx + \sum_{j=1}^{S} m_j\phi(x_j)\right]$, $\mathbf{F_2}$ is a Sx1 vector, with the entries $f_p = -m_p\ddot{\mathrm{w}}_b(t)$ and $\mathbf{F_3}$ is a Sx1 vector, with the entries $f_p = 0$. For all the indices above, $m, n = 1, 2, ..., N$ and $p, q = 1, 2, ..., S$. The base acceleration is defined as $\ddot{\mathrm{w}}_b(t) = A_0\cos(\Omega_0 t)$, where A_0 is the acceleration amplitude and Ω_0 is the excitation frequency.

The equivalent parameters of each piezoelectric resonator are obtained using an energy-based assumed-mode formulation that considers only out-of-plane flexural motion. A local coordinate ξ is defined along the resonator length, with $\xi = 0$ at the clamped end and $\xi = l_{\mathrm{beam}}$ at the free end. The transverse displacement of the j-th resonator is approximated as $\psi(\xi)u_j(t)$, where $u_j(t)$ is the tip displacement and $\psi(\xi)$ is the assumed resonator mode shape normalized such that $\psi(l_{\mathrm{beam}}) = 1$.

This notation distinguishes the resonator mode shape $\psi(\xi)$ from the host-beam modes $\phi_r(x)$ used in the Galerkin expansion.

The resonator substrate is modeled as an isotropic cantilever beam, whereas the piezoelectric layers are described by the one-dimensional piezoelectric constitutive relation $\sigma = \bar{C}_{11}^{E}\varepsilon - \bar{e}_{31}E_z$, where σ is the axial stress, ε is the axial strain, $\bar{C}_{11}^{E}$ is the elastic modulus of the piezoelectric layer at constant electric field, $\bar{e}_{31}$ is the effective piezoelectric stress constant, and E_z is the electric field through the piezoelectric thickness. The effective piezoelectric stress constant is computed as $\bar{e}_{31} = d_{31}\bar{C}_{11}^{E}$, where d_{31} is the transverse piezoelectric strain coefficient. The electrical potential is assumed to vary linearly through the piezoelectric thickness. Details of this formulation can be found in (*19, 20*).

With the tip-normalized mode shape $\psi(\xi)$, the effective mass of the j-th resonator is written as

$$m_j = m_{\text{beam}} \int_0^{l_{\text{beam}}} \psi^2(\xi)d\xi + 2m_{\text{patch}} \int_0^{l_{\text{patch}}} \psi^2(\xi)d\xi + M_t, \tag{S45}$$

where m_{beam} and m_{patch} are the mass per unit length of the resonator substrate and of one piezoelectric patch, respectively, and M_t is the tip mass, including the tip magnet and its attachment.

The corresponding linear stiffness is

$$k_j = D_{\text{beam}} \int_0^{l_{\text{beam}}} \left(\frac{d^2\psi(\xi)}{d\xi^2}\right)^2 d\xi + 2D_{\text{patch}} \int_0^{l_{\text{patch}}} \left(\frac{d^2\psi(\xi)}{d\xi^2}\right)^2 d\xi, \tag{S46}$$

where $D_{\text{beam}} = E_{\text{beam}}I_{\text{beam}}$ is the bending rigidity of the resonator substrate, and D_{patch} is the equivalent bending rigidity of one multilayer piezoelectric patch about the neutral axis of the composite section.

The electromechanical coupling coefficient of the j-th resonator is

$$\vartheta_j = B_{\text{eq}} \int_0^{l_{\text{patch}}} \frac{d^2\psi(\xi)}{d\xi^2} d\xi, \tag{S47}$$

where B_{eq} is the equivalent bending-piezoelectric coupling term of the two piezoelectric patches connected in parallel. For the symmetric bimorph configuration used here

$$B_{\text{eq}} = 2\bar{e}_{31}b_{\text{patch}} \frac{\left[\left(\frac{h_{\text{beam}}}{2} + h_{\text{polyimide}} + h_{\text{steel}} + h_{\text{pzt}}\right)^2 - \left(\frac{h_{\text{beam}}}{2} + h_{\text{polyimide}} + h_{\text{steel}}\right)^2\right]}{2h_{\text{pzt}}}, \tag{S48}$$

where the factor 2 accounts for the two piezoelectric patches, b_{patch} is the patch width, h_{beam} is the resonator-substrate thickness, and $h_{\text{polyimide}}$, h_{steel}, and h_{pzt} are the thicknesses of the polyimide, stainless-steel, and PZT layers, respectively.

The equivalent capacitance of the two piezoelectric patches connected in parallel is

$$C_{p,j} = 2\frac{\varepsilon_{33}^{S} l_{\text{patch}} b_{\text{patch}}}{h_{\text{pzt}}}, \tag{S49}$$

where ε_{33}^{S} is the permittivity of the PZT layer at constant strain.

The piezoelectric patch used in this prototype consists of multiple layers arranged from bottom to top as polyimide, stainless steel 304, PZT-5J, copper, and polyester, according to the manufacturer datasheet. Its bending rigidity is evaluated using a composite-beam formulation, so that

$$D_{patch} = D_{polymide} + D_{steel} + D_{pzt} + D_{copper} + D_{polyester}, \tag{S50}$$

where each D_ℓ is the bending-rigidity contribution of layer ℓ about the neutral axis of the composite patch. More details about the piezoelectric patch geometry and material properties are provided in the manufacturer datasheet by Mide Company.

Verification of the clamped boundary condition for the resonator beam

To address potential concerns regarding the fidelity of the clamped boundary condition of the resonator beam assumed in our model, we evaluated the possibility that bending of the resonators could induce a small rotational displacement at their fixed base, potentially compromising the idealized clamped boundary condition.

The system consists of a piezoelectric resonator beam oriented along the x-axis, with one end free and the other end rigidly connected by bolts to two identical supporting shafts, denoted as shaft A and shaft B (see Fig. S16A). The resonator bends in the z-direction. Shafts A and B are both aligned along the y-axis and are symmetrically arranged with respect to the beam. Each shaft is clamped at both ends, ensuring fixed boundary conditions. The mid-span cross-sections of shafts A and B are rigidly connected to the top and bottom surfaces of the beam, respectively, forming a sandwiched configuration. Thus, bending of the resonator induces torsional effects in the shafts (see Fig. S16).

Assuming the resonator beam is ideally clamped, the maximum bending moment at its fixed end is given by:

$$M_b = \frac{3EI_{beam}}{L_{beam}^2}\mathrm{w}_0, \tag{S51}$$

where EI_{beam} is the flexural rigidity of the piezoelectric coupled resonator beam, L_{beam} is the length of the resonator beam and w_0 is the displacement at the free tip of the beam.

Since the connection between the resonator beam and the supporting shafts is rigid, this bending moment is transmitted as torque to shafts A and B (see Fig. S16B).

The angle of twist at the point on the shaft where it connects to the beam due to this torque is:

$$\theta_t = \frac{M_b/2\ L_{shaft}/2}{GJ_{shaft}}, \tag{S52}$$

where L_{shaft} is the length of the shaft and GJ_{shaft} is its torsional rigidity. Therefore, a final

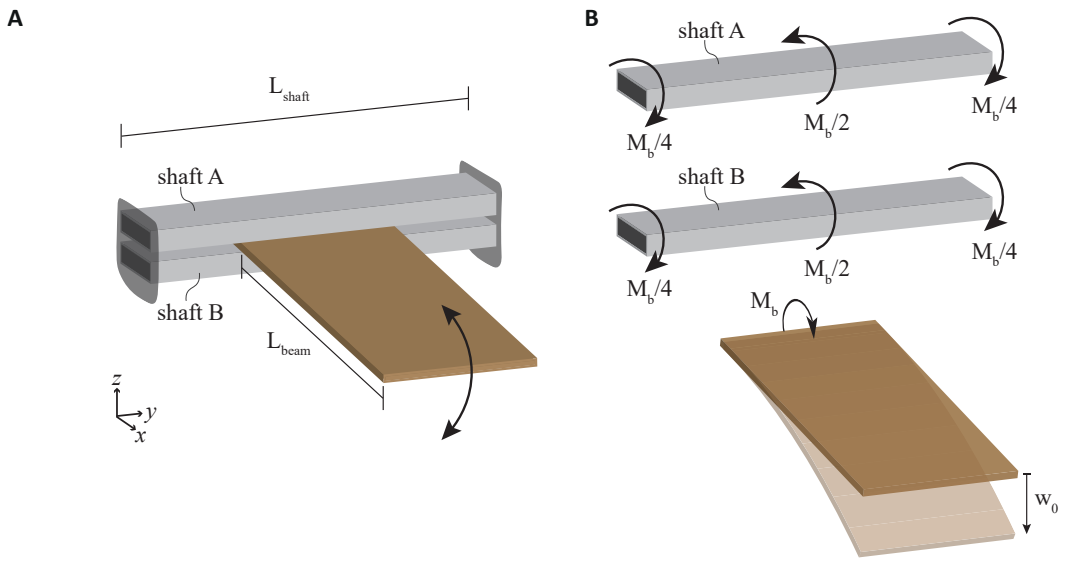


Figure S16: Schematic illustration of the resonator beam clamped by the support shafts. (A) Assembled configuration showing the beam rigidly connected between shafts A and B. (B) Free body diagram of the separated system, highlighting the bending moment at the beam's fixed end and the corresponding torques transmitted to shaft A and shaft B.

expression is obtained

$$\theta_t = \frac{3}{4}\frac{EI_{beam}}{GJ_{shaft}}\frac{L_{shaft}}{L_{beam}^2}\mathrm{w}_0 \tag{S53}$$

Using the parameters $\mathrm{w}_0 = 20$ mm (maximum tip displacement of the resonators), $L_{\mathrm{shaft}} = 30$ mm, $L_{\mathrm{beam}} = 85$ mm, $EI_{\mathrm{beam}} = 0.1592\ \mathrm{N{\cdot}m^2}$, $GJ_{\mathrm{shaft}} = 1.3284\ \mathrm{N{\cdot}m^2}$, we find:

$$\boxed{\theta_t \approx 0.0075\,\mathrm{rad}}$$

This small rotational angle confirms that the torsional rotation introduced at the resonator base is negligible. Therefore, the clamped boundary condition used in the model remains valid and is not significantly compromised by the mechanical configuration of the supporting structure.

Numerical procedure

A numerical procedure is implemented to solve the system of ordinary differential equations. The 4^{th} and 5^{th}-order Runge–Kutta method is applied over the time interval $0 \le t \le 10$ using a MATLAB code. Relative tolerance of 10^{-6} and absolute tolerance of 10^{-9} are defined to achieve high numerical accuracy.

Equation S43 is expressed in first-order state-space form as

$$\dot{\mathbf{y}}(t) = \mathbf{A}_1\mathbf{y}(t) + \mathbf{A}_2(t) + \mathbf{A}_3(\mathbf{y}(t)), \tag{S54}$$

where

$$\mathbf{y}(t) = \begin{bmatrix} \mathbf{Z}(t) \\ \dot{\mathbf{Z}}(t) \end{bmatrix}, \mathbf{A_1} = \begin{bmatrix} \mathbf{0} & \mathbf{I} \\ -\mathbf{M^{-1}K} & -\mathbf{M^{-1}C} \end{bmatrix}, \quad \mathbf{A_2}(t) = \begin{bmatrix} \mathbf{0} \\ \mathbf{M^{-1}F}(t) \end{bmatrix}, \quad \mathbf{A_3}(\mathbf{y}(t)) = \begin{bmatrix} \mathbf{0} \\ \mathbf{M^{-1}F_{nl}}(\mathbf{Z}(t)) \end{bmatrix}. \tag{S55}$$

To integrate the differential equation, the initial conditions of the system are defined at its stable equilibrium point. The initial displacement and velocity of the host beam are 0 mm and 0 mm/s, respectively. The initial displacement of the resonator beam (u_0) depends on its stability configuration. When the resonator is in a monostable configuration, the initial displacement is 0 mm. When the resonator is in a bistable configuration, there are two stable equilibrium points, and the values depend on the magnet spacing. For our analysis, we select the equilibrium point with a positive value for the initial displacement. The initial velocity ($\dot{u}_0$) and voltage (v_0) of the resonator beam are 0 mm/s and 0 V, respectively.

In the sweep-frequency analysis, the system is excited with a stepped-sine input over a range of frequency at a fixed amplitude. The initial conditions are updated at each frequency step following a continuation method. For instance, at the first frequency value, we use the predefined initial state ($u_0, \dot{u}_0 = 0, v_0 = 0$), whereas at the n^{th} frequency the initial displacement and velocity are taken from the final state obtained at the $(n-1)^{\text{th}}$ step. This procedure is repeated across the entire sweep. Updating the initial conditions in this manner rapidly drives the response to the steady-state regime at each frequency, substantially reducing the computational cost while naturally capturing any hysteresis effects that arise during the sweep.

Table S4 shows the values of the parameters of the system, which are adopted based on the geometry and physical properties of the fabricated metastructure.

The transmissibility frequency response is used to investigate the vibration of the metastructure. The base is excited by an upward stepped-sine sweep from 25 to 90 Hz in increments of 0.1 Hz. Transmissibility T is defined as the ratio of the root mean square (rms) of the steady-state velocity at the tip of the host beam to that at its base as a function of excitation frequency Ω_0

$$\boxed{\mathrm{T}(\Omega_0) = \frac{\text{rms } (\dot{\mathrm{w}}_t(L, t_{ss}))}{\text{rms } (\dot{\mathrm{w}}_t(0, t_{ss}))},} \tag{S56}$$

where t_{ss} is the time interval of the steady-state regime, which corresponds to the last 20% of the total time series, for each frequency step. The transmissibility is reported on a logarithmic scale as $\log_{10} T(\Omega_0)$. The locally resonant attenuation band is identified from the frequency interval in which $\log_{10} \mathrm{T}(\Omega_0) < -0.025$.

To investigate the electrical generation, the RMS voltage across each load resistance is first calculated over the steady-state interval t_{ss} as

$$V_{\text{rms},j}(\Omega_0) = \text{rms}\left[v_j(t_{ss})\right], \qquad j = 1, 2, \ldots, S. \tag{S57}$$

Length of the host beam, L	985 mm
Length of the resonator beam, l_{beam}	85 mm
Length of the piezoelectric patch, l_{patch}	39 mm
Width of the host beam, b	45 mm
Width of the resonator beam, b_{beam}	24 mm
Width of the piezoelectric patch, b_{patch}	23.3 mm
Thickness of the host beam, h	2 mm
Thickness of the resonator beam, h_{beam}	0.5 mm
Thickness of the piezoelectric patch, h_{patch}	0.41 mm
Young's modulus of carbon fiber, E	62 GPa
Density of the carbon fiber, ρ	1335 kg/m^3
Length of the magnet, l_{mag}	2 mm
Magnet moment of magnet A, μ_A	0.08 Am^2
Magnet moment of magnet B, μ_B	0.08 Am^2
Modal damping of the r-th mode of the host beam, ζ_r	0.005
Damping ratio of the j-th resonator, ζ_j	0.03
Number of modes in expansion, N	10
Load resistance, R_L	470 kΩ

Table S4: Summary for values of the parameters of the metastructure with magneto-elastic piezoelectric resonators.

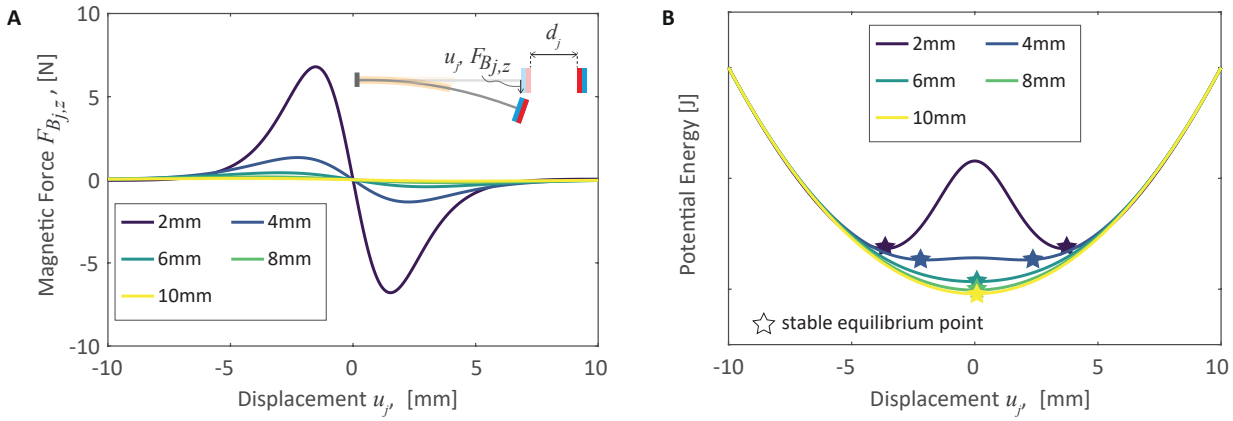


Figure S17: Nonlinear magnetic force and potential energy for different magnet spacings. (A) Magnetic force in z direction as function of the displacement of the j-th resonator. (B) Potential energy of the resonator under the magnetic force influence.

The total harvested power is obtained by summing the power dissipated in each load,

$$\boxed{P_{\text{tot}}(\Omega_0) = \frac{1}{R_L}\sum_{j=1}^{S} V_{\text{rms},j}^2(\Omega_0)}. \tag{S58}$$

where, for the present metastructure, all resonator channels use the same load resistance. The quantity P_{tot} is used to quantify the total electrical power harvested by the metastructure across the independent resonator channels.

Numerical results

Nonlinear magnetic force (Fig. S17A) and potential energy of the j-th resonator (Fig. S17B) are reported as a function of displacement u_j for different magnet spacings. Figure S17A shows that as the spacing between the magnets decreases, the magnetic force increases. Figure S17B shows that at spacings of 2 mm and 4 mm, the system exhibits a bistable potential, where the beam has two stable equilibrium points. At larger spacings, the magnetic force decreases, resulting in a monostable potential. At a spacing of 10 mm, the system is effectively free from magnetic influence because the magnitude of the magnetic force is nearly zero.

The equations of motion are numerically integrated as defined in the Numerical Procedure subsection. Then, the transmissibility and the total harvested power are calculated as a function of the excitation frequency. We first obtain numerical results for various magnet spacings while keeping the spacing identical across all resonators in the metastructure.

Figure S18 presents the numerical transmissibility of the system over the frequency for various magnet spacings (from 2 mm to 10 mm). The peaks in the transmissibility correspond to the wave amplification (around the resonance conditions), while the gray region highlights the local

resonance bandgap. When the resonators are in the monostable regime at 10 mm (magnet spacing), the bandgap region is established in the frequency range of 41 Hz to 59 Hz. As the spacing decreases, the bandgap region shifts to lower frequencies; for instance, at a magnet spacing of 5 mm, the bandgap is defined from 25 Hz to 40 Hz. At a spacing of approximately 4.3 mm, a transition point is reached, where the resonators change from a monostable to a bistable regime. Approaching the monostable-bistable transition reduces the effective stiffness and shifts the attenuation region toward lower frequencies, potentially below the analyzed range near the transition. When the resonators are in a bistable regime and the magnet spacing decreases, the bandgap region shifts toward higher frequencies.

Figure S19 presents the numerically evaluated total harvested power normalized by the squared base-acceleration amplitude for different magnet spacings. The total harvested power is computed by summing the power dissipated in the independent load resistances of the resonator channels. The largest power levels occur near the transmissibility peaks, where resonance of the host beam produces higher oscillation amplitudes and stronger strain in the piezoelectric patches. Inside the bandgap regions, the harvested power decreases relative to the resonance peaks because the locally resonant attenuation reduces the vibration transmitted through the host beam. As the magnet spacing changes, the power peaks shift in frequency, following the magnetically tuned resonator dynamics. The top view of the normalized power surface highlights this tuning behavior and shows the bandgap boundaries for each magnet spacing. In the bistable regime, multiple power peaks appear over a broader frequency interval, whereas the monostable regime produces a more concentrated power response at lower frequencies. At 10 mm, where the magnetic interaction is weak and the resonators approach a quasi-linear monostable response, the power peaks decrease in magnitude. The highest normalized harvested-power levels are obtained for magnet spacings between 6 and 7 mm, indicating that this range provides a favorable balance between resonator motion and electromechanical conversion in the numerical model.

Figure S20 presents the transmissibility and the normalized total harvested power of the metastructure for selected magnet spacings under different excitation amplitudes. Figures S20A and B show the bistable configuration with a magnet spacing of 3 mm. For low and moderate excitation amplitudes, the bistable resonators produce a clear attenuation band. However, when the excitation amplitude is increased to 16 g, the bandgap region is strongly reduced and the transmissibility response becomes closer to $log_{10}T = 0$, indicating that the attenuation effect is impaired and that vibration is transmitted through the host beam with limited suppression. The corresponding normalized total harvested power increases with excitation amplitude and exhibits multiple peaks over a broad frequency range, reflecting the amplitude-dependent nonlinear dynamics of the bistable resonators.

Figures S20C and D show the monostable configuration with a magnet spacing of 7 mm. In this case, the transmissibility and normalized harvested-power responses remain comparatively

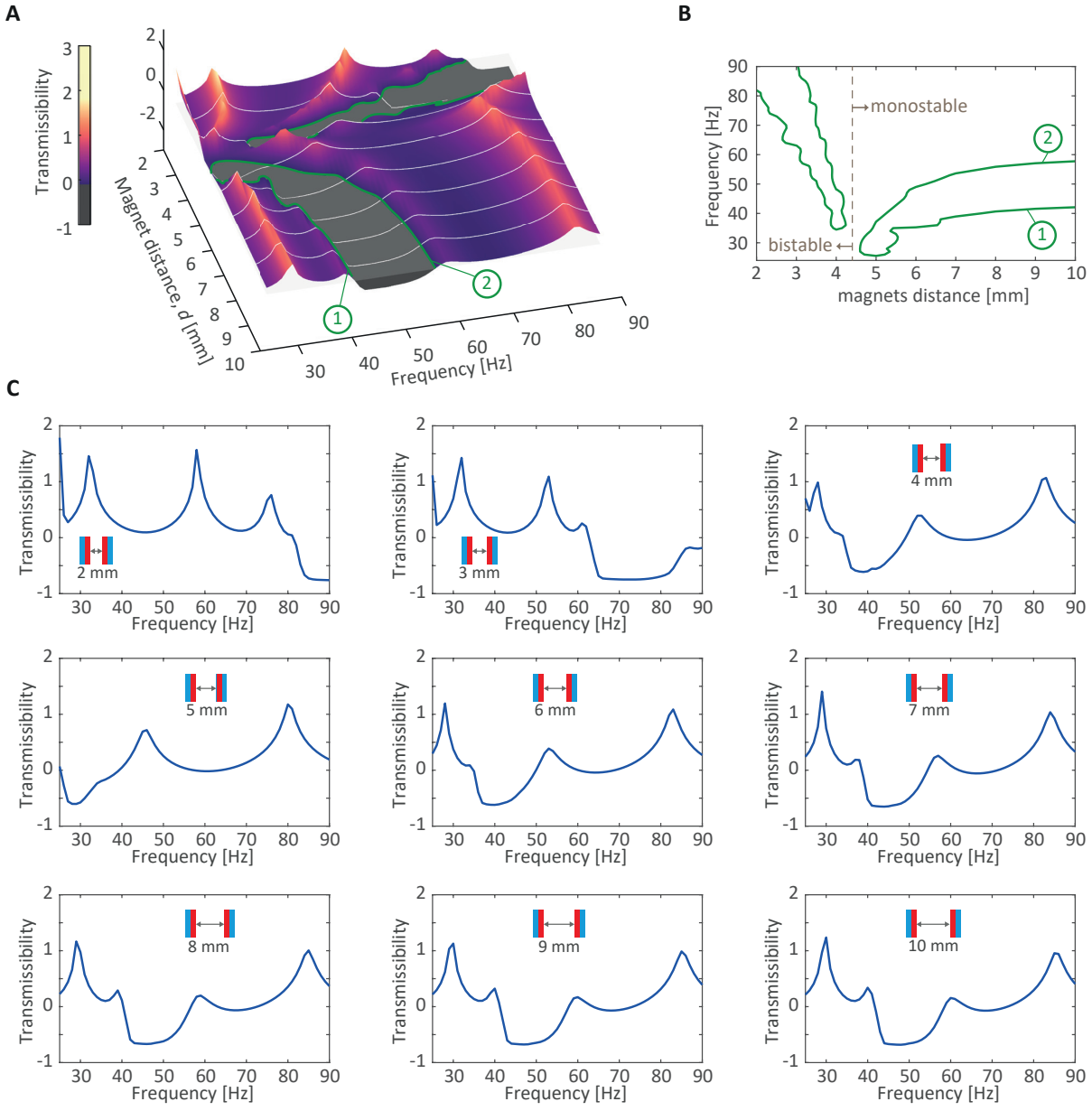


Figure S18: Transmissibility evaluated numerically over a frequency range between 25-90 Hz. (A) Velocity transmissibility between the tip of the beam and its base for various excitation frequencies and magnet spacings. The gray region indicates the bandgap, where the transmissibility is below –0.05 on the logarithmic scale, with the green lines marking the lower (line 1) and upper (line 2) boundaries. (B) Bandgap boundary for different magnet spacings. The vertical gray dashed line indicates the numerical transition from bistable to monostable behavior of the resonators. (C) 2D plots of the velocity transmissibility for different magnet spacings.

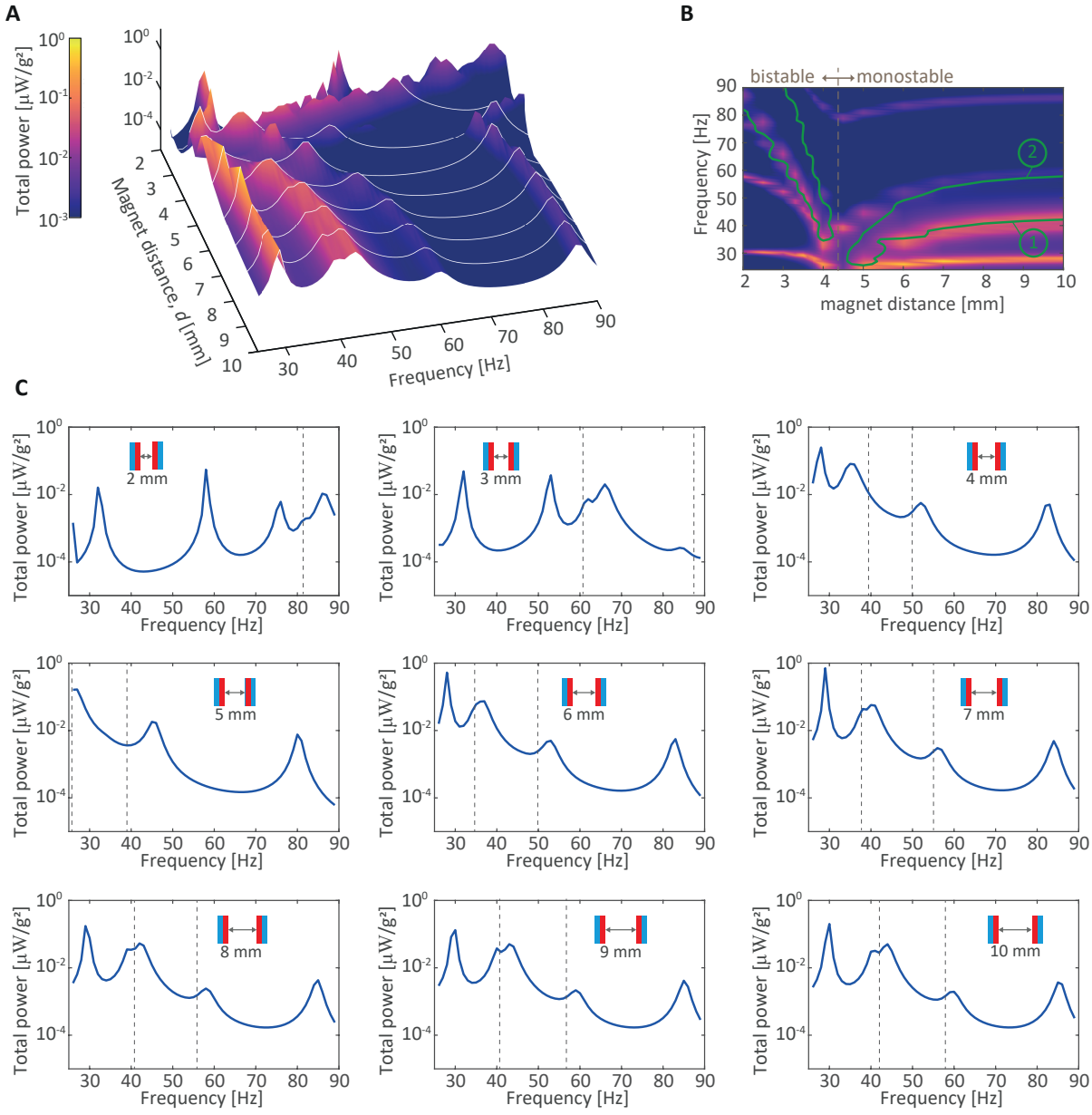


Figure S19: Numerically evaluated total harvested power normalized by the squared base-acceleration amplitude over the 25–90 Hz frequency range. (A) Normalized total harvested power as a function of excitation frequency and magnet spacing. (B) Top view of the normalized total-power surface with the bandgap boundaries identified for each magnet spacing. The vertical gray dashed line indicates the numerical transition between monostable and bistable resonator behavior. (C) 2D normalized total power curves for selected magnet spacings, with vertical dashed lines indicating the lower and upper limits of the corresponding bandgap regions.

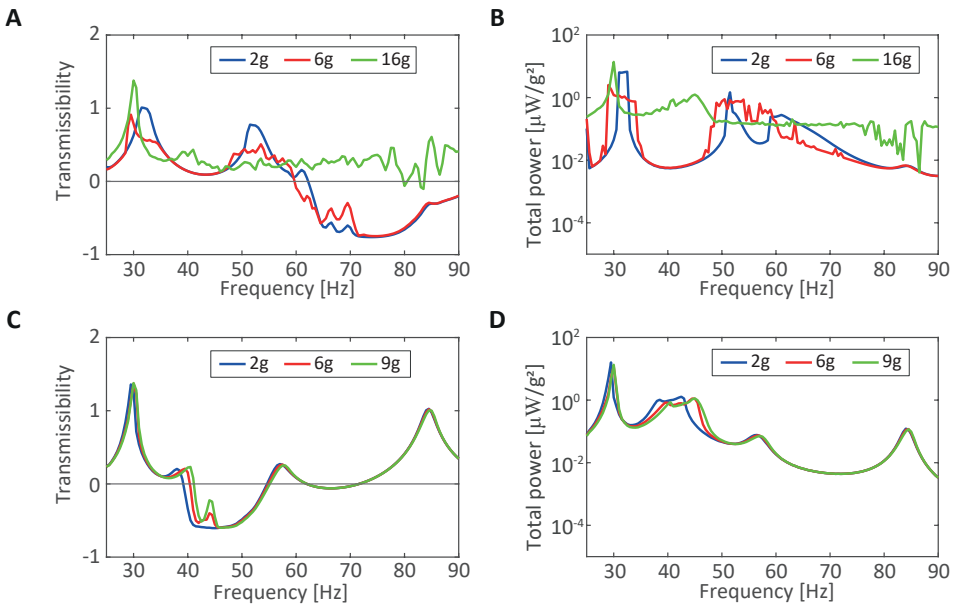


Figure S20: Numerically evaluated transmissibility and total harvested power normalized by the squared base-acceleration amplitude over the 25–90 Hz frequency range for different excitation amplitudes. (A,B) Bistable configuration with magnet spacing of 3 mm. (C,D) Monostable configuration with magnet spacing of 7 mm.

stable across the excitation amplitudes considered. This behavior indicates that the monostable configuration is less sensitive to excitation amplitude over the tested range, preserving both the attenuation band and the main harvesting peaks.

To investigate the amplitude dependence of the metastructure in the bistable regime, we study the dynamic behavior of the system under a fixed excitation frequency inside the bandgap region. The displacement of the resonators, with magnet spacing of 3 mm, is shown in Fig. S21A,B and C for excitation amplitudes of 2 g, 6 g, and 16 g, respectively. The resonators are numbered from 1 to 7, where resonator 1 is located closest to the fixed end of the host beam, and resonator 7 is located nearest to the free end, as shown in Fig. 1A of the main manuscript. For applied accelerations of 2 g and 6 g, the resonators exhibit intrawell motion. However, at 16 g, the resonators exhibit irregular interwell motion.

The 0–1 test for chaos is applied to determine whether the resonator responses are chaotic or nonchaotic. (as detailed in the section '0-1 Test for Chaos'). Figures S21D, F, and H show the results of the 0-1 test for chaos for each resonator under excitation amplitudes of 2 g, 6 g, and 16 g, respectively. At accelerations of 2 g and 6 g, the dynamic behavior of all the resonators is classified as regular motion, with test values below 0.2. However, at an acceleration of 16 g, the dynamic behavior of all the resonators is classified as chaotic motion, except for resonator 7, which yields an inconclusive test. The findings from the 0-1 test for chaos and the transmissibility under

different excitation amplitudes indicate that the presence of chaos disrupts the bandgap region. At high excitation amplitude, chaotic interwell motion disrupts the stable locally resonant interaction needed to sustain the bandgap.

Figures S21E, G, and I show the root mean square (rms) voltage for each resonator under excitation amplitudes of 2 g, 6 g, and 16 g, respectively. At an acceleration of 2 g (Fig. S21E), all resonators produce similar energy output. However, moving from the base to the tip, the resonators produce slightly less voltage. For example, resonator 1 generates 0.7 V (1.04 μW), while resonator 7 generates 0.65 V (0.89 μW). The observed decrease in voltage is attributed to the attenuation of the wave propagation along the length of the metabeam. As the resonators are positioned further from the excitation point, the harvested energy slightly decreases. This pattern is similar at an acceleration of 6 g (Fig. S21G). Resonator 1 generates 0.8 V (1.36 μW), and then the energy slightly decreases to 0.6 V (0.76 μW) at resonator 7. At an acceleration of 16 g (Fig. S21I), where the resonators exhibit chaotic motion, the harvested energy increases significantly relative to that obtained at 2 g and 6 g. Resonator 1 generates 1.6 V (5.4 μW). This energy gradually decreases until resonator 6 and drops to 0.8 V (1.36 μW) at resonator 7.

The same procedure is repeated to investigate the amplitude dependence of the metastructure in the monostable regime, with magnet spacing fixed at 7 mm. Figure S22 shows the displacement of the resonators, the results of the 0-1 test for chaos, and the rms voltage for an acceleration of 2 g, 6 g, and 9 g. For all excitation levels, the monostable resonators do not exhibit chaotic behavior. The time series of the displacement of the resonators shows regular motion, and the 0-1 test for chaos confirms their regular behavior. The rms voltage of monostable resonators demonstrates that resonator 1, closest to the fixed end of the beam, generates more energy than the resonators positioned closer to the tip of the beam across all acceleration levels. For example, at an acceleration of 9 g, resonator 1 generates 6.1 V (79.1 μW), while resonator 7 generates 0.05 V (0.005 μW).

Numerical results for upward and downward frequency sweeps under varying excitation amplitudes are presented in Fig. S23. Figures S23A–C depict the evolution of the bandgap boundaries as a function of frequency for 0.01 g, 2 g and 6 g, respectively. Figures S23D, E and F show the transmissibility response for the monostable configuration at a magnet spacing of 7 mm for 0.01 g, 2 g and 6 g, respectively, while Figs. S23G, H and I correspond to the bistable configuration at a magnet spacing of 3 mm for 0.01 g, 2 g and 6 g, respectively.

At very low excitation amplitudes (0.01 g), the system exhibits nearly identical responses for both sweep directions. This occurs because the nonlinearities are not significantly pronounced at this level of excitation. The results of the bandgap boundaries (Fig. S23A) and transmissibility response for monostable (Fig. S23D) and bistable (Fig. S23G) are superimposed by the sweep directions.

At an excitation of 2 g, the response for monostable configurations remains very similar for both sweep directions, as shown in Fig. S23E. In the bistable case (Fig. S23H), slight discrepancies

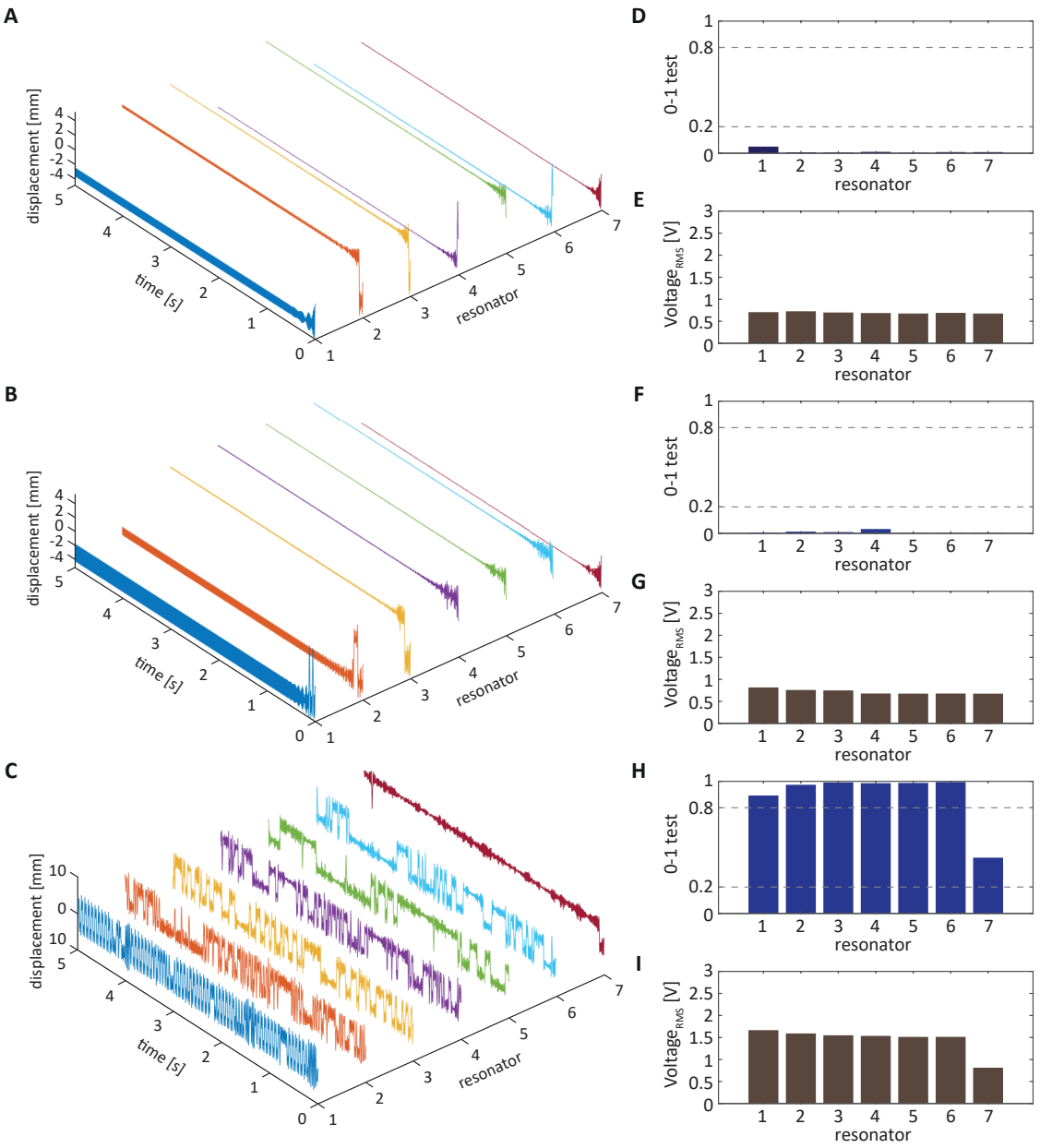


Figure S21: Numerical dynamic analysis of the resonators in bistable conditions (magnet spacing of 3 mm) under different excitation amplitudes and at a fixed frequency of 71 Hz. Time series of the displacement of resonators under (A) 2 g, (B) 6 g, and (C) 16 g. Results of the 0-1 test for chaos of the resonators under (D) 2 g, (F) 6 g, and (H) 16 g. Root Mean Square (RMS) voltage of the resonators under (E) 2 g, (G) 6 g, and (I) 16 g.

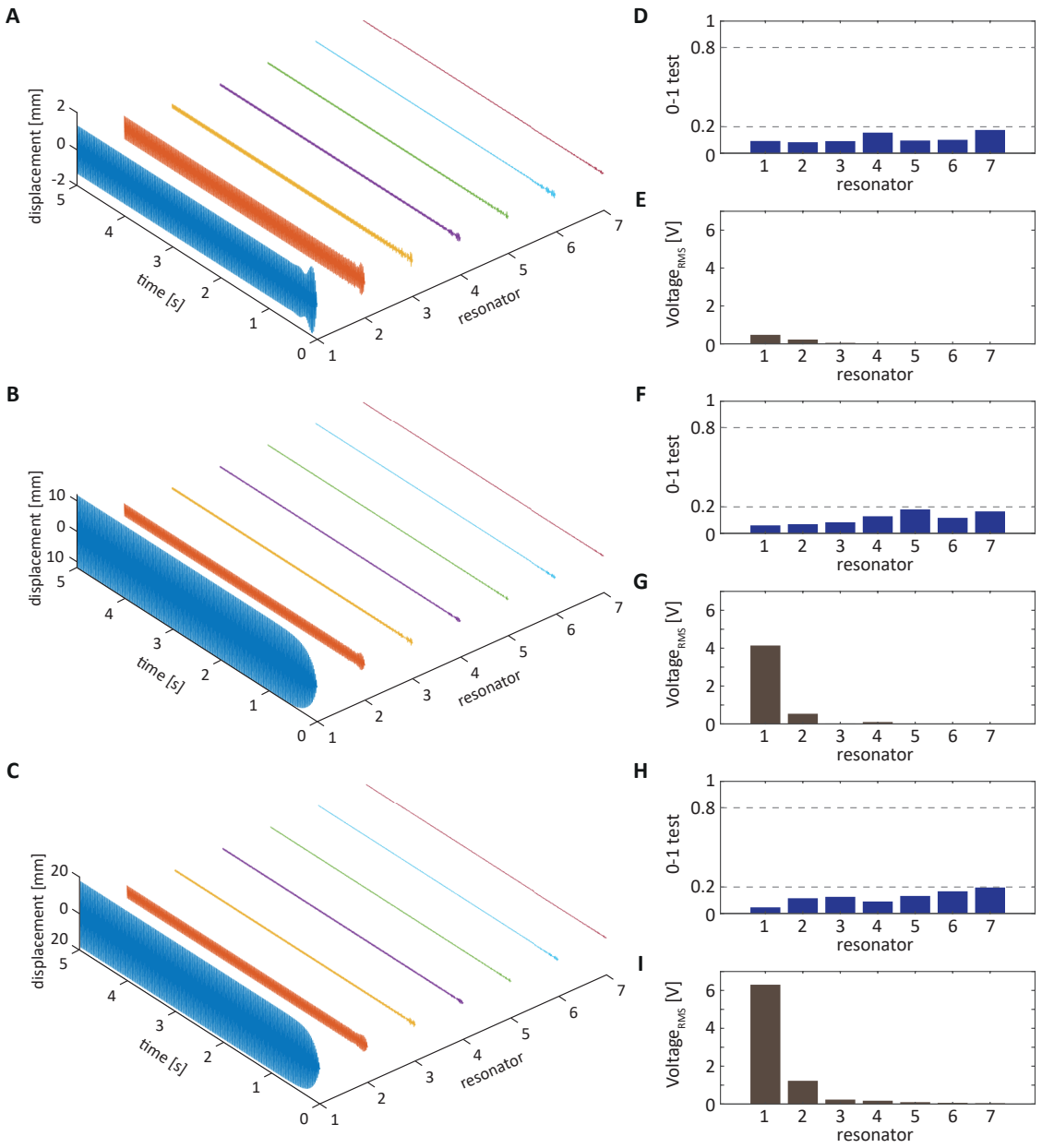


Figure S22: Numerical dynamic analysis of the resonators in monostable conditions (magnet spacing of 7 mm) under different excitation amplitudes and at a fixed frequency of 45 Hz. Time series of the displacement of resonators under (A) 2 g, (B) 6 g, and (C) 9 g. Results of the 0-1 test for chaos of the resonators under (D) 2 g, (F) 6 g, and (H) 9 g. Root Mean Square (rms) voltage of the resonators under (E) 2 g, (G) 6 g, and (I) 9 g.

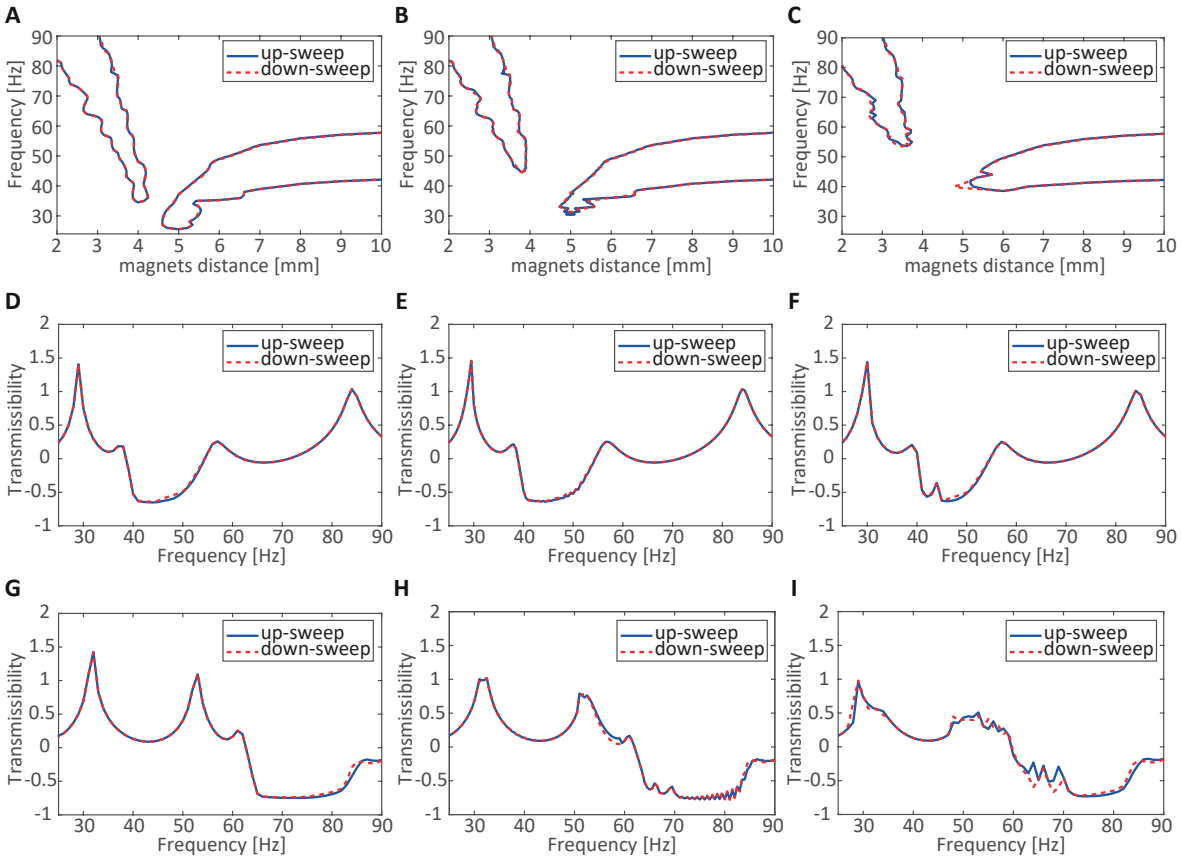


Figure S23: Numerical results of vibration attenuation performance under up- and down-frequency sweeps for different excitation amplitudes, 0.01 g (left column), 2 g (middle column) and 6 g (right column). (A–C) Bandgap boundary for different magnet spacings. (D-F) Transmissibility curves for the resonators in the monostable regime at a magnet spacing of 7 mm. (G-I) Transmissibility curves for the resonators in the bistable regime at a magnet spacing of 3 mm.

emerge, particularly in the 55–60 Hz range due to resonance of the nonlinear resonators. However, the bandgap region remains effectively unchanged, and this observation holds across all bistable configurations, as shown in Fig. S23B.

At higher excitation levels (6 g), the same trend is observed. The bandgap boundaries remain consistent between sweep directions. A notable exception occurs in the bistable case (Fig. S23I), where fluctuations arise due to the presence of chaotic dynamics. Nevertheless, these irregularities do not significantly affect the location or integrity of the bandgap. Overall, the global behavior of the host beam remains largely unaffected by the jump phenomena of the nonlinear resonators.

Figure S24 presents the numerical energy harvesting response under up- and down-frequency sweeps at an excitation amplitude of 2 g. For the complete metastructure, the electrical response is quantified by the total harvested power, computed as the sum of the power dissipated in the independent load resistances of the resonator channels, normalized by the squared base-acceleration.

For individual resonators, the voltage response is shown to illustrate the local electromechanical behavior. Results for the lowest excitation amplitude, 0.01 g, are omitted because the nonlinear effects are weak. For 6 g, the qualitative trends are similar to those observed at 2 g.

Figures S24A and B show the total normalized harvested power for the monostable and bistable configurations, respectively. Compared with the transmissibility response, the electrical response shows more evident differences between up- and down-frequency sweeps. This behavior is expected because the harvested electrical output is directly governed by the resonator dynamics, where nonlinear effects and jump phenomena are more pronounced.

In the monostable configuration, differences between up- and down-sweep responses are mainly restricted to a narrow frequency interval near 30 Hz, which corresponds to the resonance region of the host beam. These differences arise from the large vibration amplitudes near resonance, which activate the nonlinear response of the resonators. Figures S24C and E show the voltage responses of resonator 1, located near the fixed base of the host beam, and resonator 7, located near the free end, respectively. The voltage response of resonator 1 is nearly identical for both sweep directions, with its highest peak occurring near the resonator resonance at approximately 42 Hz. In contrast, resonator 7 is more affected by the host-beam resonance and exhibits a clearer sweep-dependent response, with its highest peak occurring near the host-beam resonance at approximately 29 Hz.

In the bistable configuration, the differences between up- and down-sweep responses are more pronounced, particularly near the resonator-dominated frequency range. This behavior is associated with the jump phenomenon, as illustrated by the voltage response of resonator 1 in Fig. S24D. For the up-frequency sweep, the jump occurs around 60 Hz, whereas for the down-frequency sweep it occurs near 51 Hz. Figure S24F shows the voltage response of resonator 7. In this case, only slight differences between sweep directions are observed. This occurs because, over this frequency interval, the system operates within the attenuation band, where the vibration transmitted toward the beam tip is reduced, limiting the nonlinear response of resonators located closer to the free end.

Therefore, while the difference between up- and down-sweep excitations has a more noticeable effect on the energy harvesting performance, particularly due to the jump phenomenon of the nonlinear resonators, these differences do not substantially alter the overall conclusions regarding the functionality of the metastructure.

To evaluate the effect of mechanically programmed nonidentical resonators, numerical simulations were performed for metastructures with selected magnet-spacing distributions. Each configuration is defined by the vector $\mathbf{d} = [d_1, d_2, \ldots, d_S]$, where d_j is the magnet spacing of the j-th resonator, as illustrated in Fig. S25A. The selected configurations are listed in Table S5. Cases $C1$–$C7$ correspond to the nonidentical configurations also considered experimentally, whereas $C8$–$C14$ are additional model-selected configurations. Cases $C8$, $C9$, $C11$, and $C12$ correspond, respectively, to the model-predicted candidates $P1$, $P2$, $P4$, and $P3$ highlighted in Fig. 5 of the main manuscript.

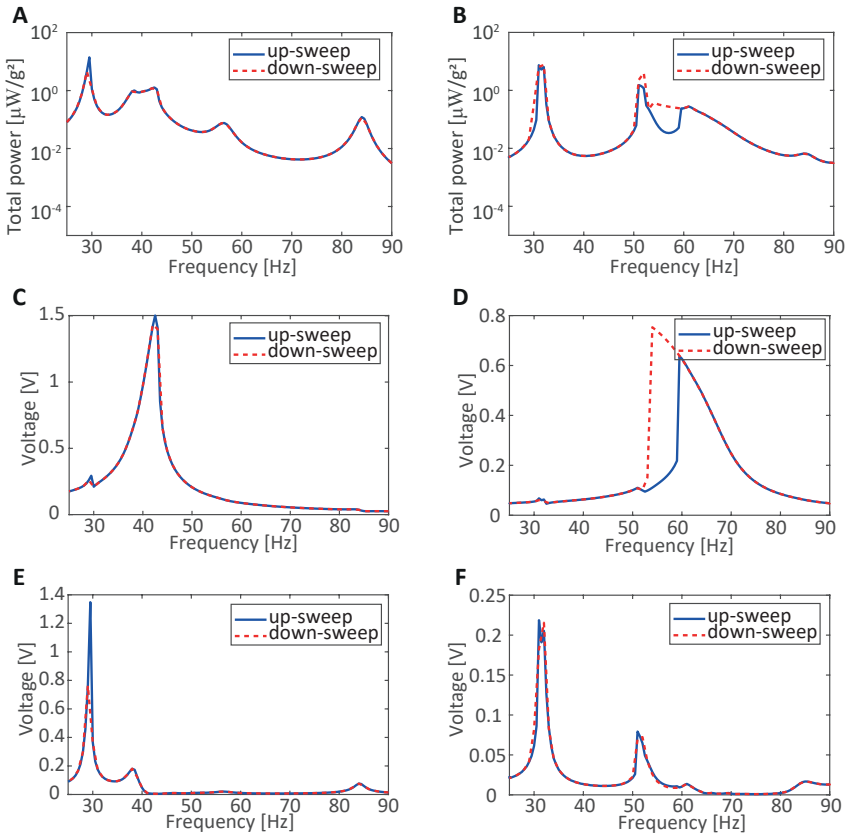


Figure S24: Numerical energy harvesting response under up- and down-frequency sweeps at an excitation amplitude of 2 g. (A,B) Total normalized harvested power of the metastructure for the monostable (A) and bistable (B) configurations. (C,E) Voltage response of resonator 1, located closest to the fixed base, and resonator 7, located closest to the free end, in the monostable configuration. (D,F) Voltage response of resonator 1 and resonator 7 in the bistable configuration.

Case	Magnet spacing vector **d** [mm]
C1	[7, 7, 7, 7, 3, 3, 3]
C2	[7, 7, 7, 3, 3, 3, 3]
C3	[3, 3, 3, 7, 7, 7, 7]
C4	[7, 3, 7, 3, 7, 3, 7]
C5	[3, 7, 3, 7, 3, 7, 3]
C6	[2, 3, 4, 5, 6, 7, 8]
C7	[8, 7, 6, 5, 4, 3, 2]
C8	[4, 5, 5, 5, 7, 3, 2]
C9	[4, 5, 7, 7, 3, 3, 2]
C10	[4, 7, 7, 3, 3, 2, 2]
C11	[7, 5, 3, 7, 3, 7, 2]
C12	[7, 5, 3, 7, 3, 5, 2]
C13	[7, 5, 3, 7, 3, 7, 3]
C14	[5, 7, 3, 7, 3, 7, 3]

Table S5: Selected nonidentical magnet spacing configurations included in the numerical performance map. Cases C_1–C_7 correspond to configurations also considered experimentally, whereas C_8–C_{14} are additional model-selected configurations.

The results are represented in a two-dimensional performance map that separates the vibration-attenuation and energy-harvesting metrics. The attenuation performance is quantified by the bandgap bandwidth B, defined from the identified locally resonant attenuation intervals. The harvesting performance is quantified by the area A_P under the normalized total harvested-power curve over the 25–90 Hz frequency range. The total harvested power is computed by summing the power dissipated in the independent load resistances of the resonator channels and is normalized by the squared base-acceleration amplitude.

The quantities A_P and B are normalized using reference identical configurations. The harvested-power area is normalized by the identical monostable configuration with a magnet spacing of 7 mm, whereas the bandgap bandwidth is normalized by the identical bistable configuration with a magnet spacing of 3 mm. Their normalized values are indicated by the dashed reference lines $A_P/A_{P,7\mathrm{mm}} = 1$ and $B/B_{3\mathrm{mm}} = 1$. The normalization follows the same reference definitions used in the experimental performance analysis.

Figure S25B presents the numerical performance map for the selected nonidentical configurations. Values larger than unity indicate improvement relative to the corresponding identical reference. Configurations located in the upper-left region improve the attenuation bandwidth while reducing the harvested-power area relative to the harvesting reference. Configurations located in the lower-right region increase the harvested-power area while reducing the attenuation bandwidth relative to the bandgap reference. Configurations located in the upper-right region provide simultaneous improvement in both metrics. In the selected set, $C11$ and $C12$ lie in this dual-improvement region, whereas $C9$ remains close to the attenuation reference while increasing the harvested-power area. These results show that the spatial distribution of magnet spacings can be used to redistribute the resonator dynamics and tune the balance between vibration attenuation and energy harvesting.

Fabrication and assembly of the physical prototype

The host beam is fabricated by cutting a carbon fiber plate (with dimensions of 985 × 45 × 2 mm^3) using a CNC engraving machine (Roland EGX 600). Seven uniformly spaced voids, each measuring 118 × 30 mm^2 and precisely aligned along the central axis of the beam, are perforated using the same CNC machine.

For the elastic-invisibility design, reinforcement grids are also fabricated from carbon fiber using the CNC machine. Their dimensions are defined as specified in the elastic-reconstruction section ($b_{x,1} = 1$ mm, $b_{x,2} = 7.1$ mm, $b_y = 2.1$ mm, and $h_t = 1.1$ mm). A total of seven pairs of reinforcements are prepared. They are bonded to encircle the voids on both sides of the beam to preserve the symmetry. Before bonding them to the host beam, a surface treatment of the bonding faces is carried out, which involves contaminant removal using detergents and isopropyl alcohol, followed by abrasion with sandpaper. A structural adhesive (3M Scotch-Weld DP460) is applied to bond the reinforcements, and the assembly is left to cure for 24 hours at 25°C.

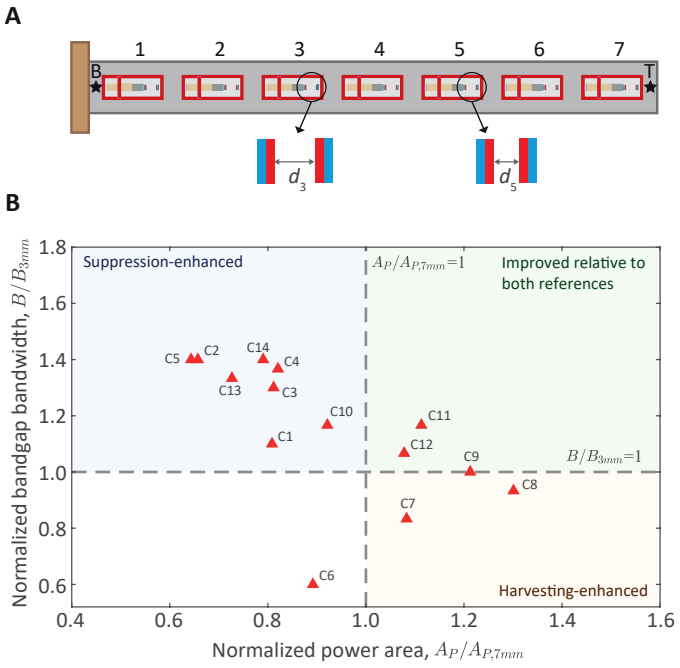


Figure S25: Numerical performance map of selected nonidentical magnet spacing configurations. (A) Schematic representation of the metabeam with mechanically programmed resonators. (B) Numerical performance map showing the normalized harvested-power area, $A_P/A_{P,7\text{mm}}$, and the normalized bandgap bandwidth, $B/B_{3\text{mm}}$, for the selected configurations listed in Table S5. The harvested-power reference $A_{P,7\text{mm}}$ is obtained from the identical monostable configuration with magnet spacing of 7 mm, whereas the bandgap reference $B_{3\text{mm}}$ is obtained from the identical bistable configuration with magnet spacing of 3 mm. Dashed lines indicate the reference value of unity for each metric.

The resonator beams are made of carbon fiber and were fabricated by CNC machining with overall dimensions of $95 \times 24 \times 0.5$ mm^3. After clamping, 85 mm of the resonator beam remains as the effective cantilever length. Two piezoelectric layers (S118-J1SS-1808YB, Mide Technology) are bonded to the two opposite faces of each resonator beam using the same structural adhesive and bonding procedure. The piezoelectric layers are positioned near the fixed end of the resonator beams, where the bending strain is higher, to enhance electromechanical conversion.

The piezoelectric resonator beams are mounted on the host beam and precisely positioned inside the voids, aligned along the neutral axis. The reinforcement bar is used to clamp the resonator in place. Two M2 bolts are carefully tightened to secure longitudinal and transverse movement constraints at the clamped region without overtightening, preventing potential damage to the piezo. The deformable part of the resonator is positioned inside the larger section of the void, while the smaller section allows easy access to electrical mounting. The effective length of each piezoelectric beam remains 85 mm.

A permanent magnet (Neodymium Magnet NdFeB with a diameter of 8 mm and a height of 2 mm, magnetized in the axial direction) is attached to the tip of the beam using a 3D-printed holder, manufactured with a Stratasys Origin One Printer. An identical magnet is mounted on the host beam in front of the first magnet using an adjustable 3D-printed holder. The magnets are positioned with approximately collinear magnetization axes with equal-polarity faces opposing each other, generating a repulsive magnetic force, as previously described. The adjustable holder enables precise control of the magnet spacings. A bolt is used to securely fix the holder at the desired magnet spacing during testing.

A custom 3D-printed connector is designed to support the electrode connections of the piezo patches. It is fixed using the same M2 bolts as the resonator clamp and aligned with the positive and negative conductive regions of the piezo, ensuring proper electrical contact with the wires. A 22-gauge cable is fixed with a small bolt to keep the connections. The cables are organized on a protoboard, with the piezo patches of each resonator connected in parallel. This parallel connection doubles the current output while maintaining the same voltage. A load resistor of 470 kΩ is also connected in parallel to the piezo terminals to properly measure the harvested energy. Each resonator has its dedicated electrical circuit, and there are no electrical connections between the seven circuits.

Figure S26 shows a detailed drawing of the proposed metastructure, including all assembling components. Movie S6 shows an exploded animation of the system assembly.

Figure S27 shows a photograph of our prototype. Details of the cloaked metabeam equipped with magneto-elastic piezoelectric resonators are illustrated in the zoomed-in view of Fig. S27A. The restoring force of the resonator can be manually controlled by using the adjustable magnet holder. Figure S27B shows the resonator with a small magnet spacing, which exhibits bistable behavior (the photo shows the beam on its stable equilibrium point on the right side; the other stable

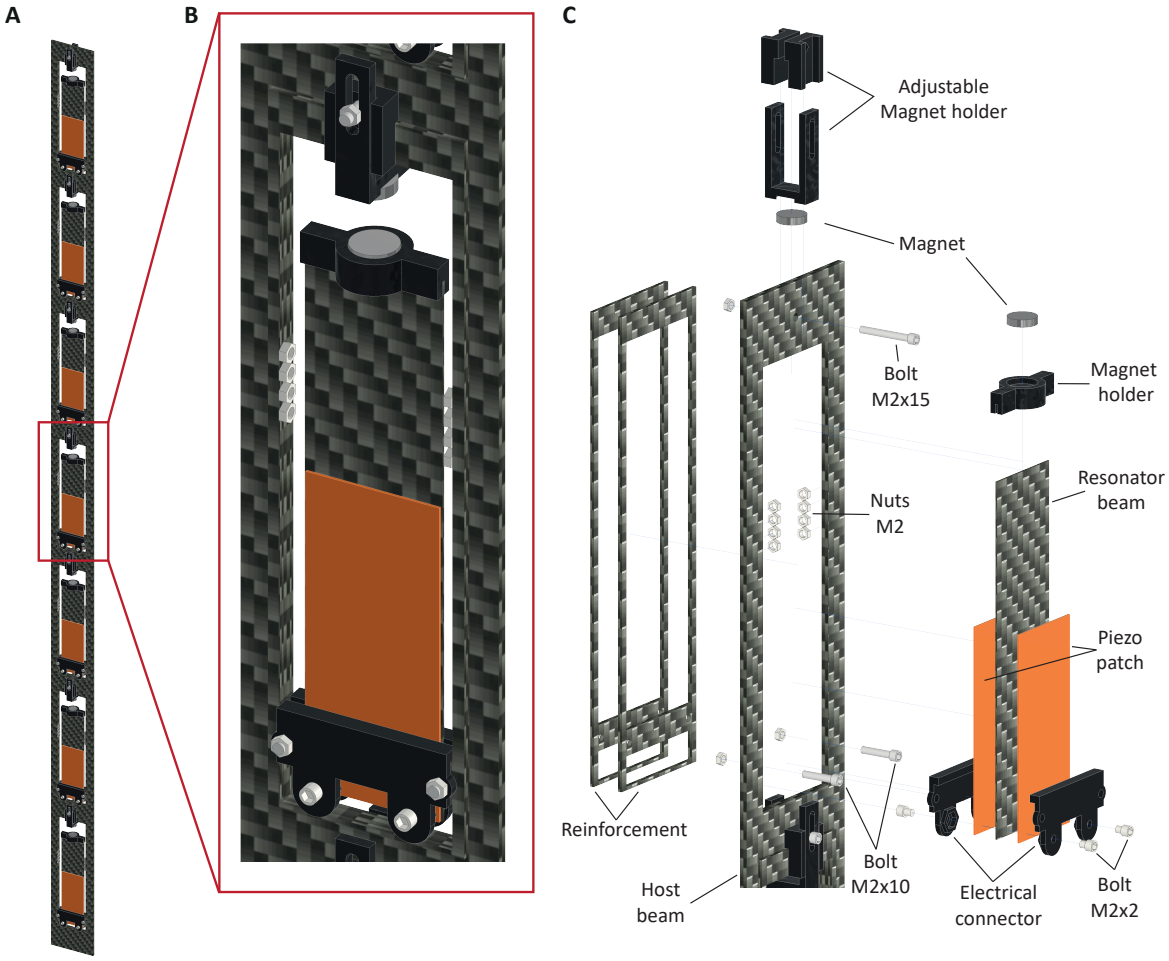


Figure S26: Illustration of the cloaked metastructure with the magneto-elastic piezoelectric resonators. (A) Drawing of the metastructure. (B) Zoomed-in view of the cloaking design and the magneto-elastic piezoelectric resonator. (C) Exploded-view drawing of all assembly parts.

equilibrium point is located on the left). Figure S27C shows the resonator with a large magnet spacings, which exhibits monostable behavior.

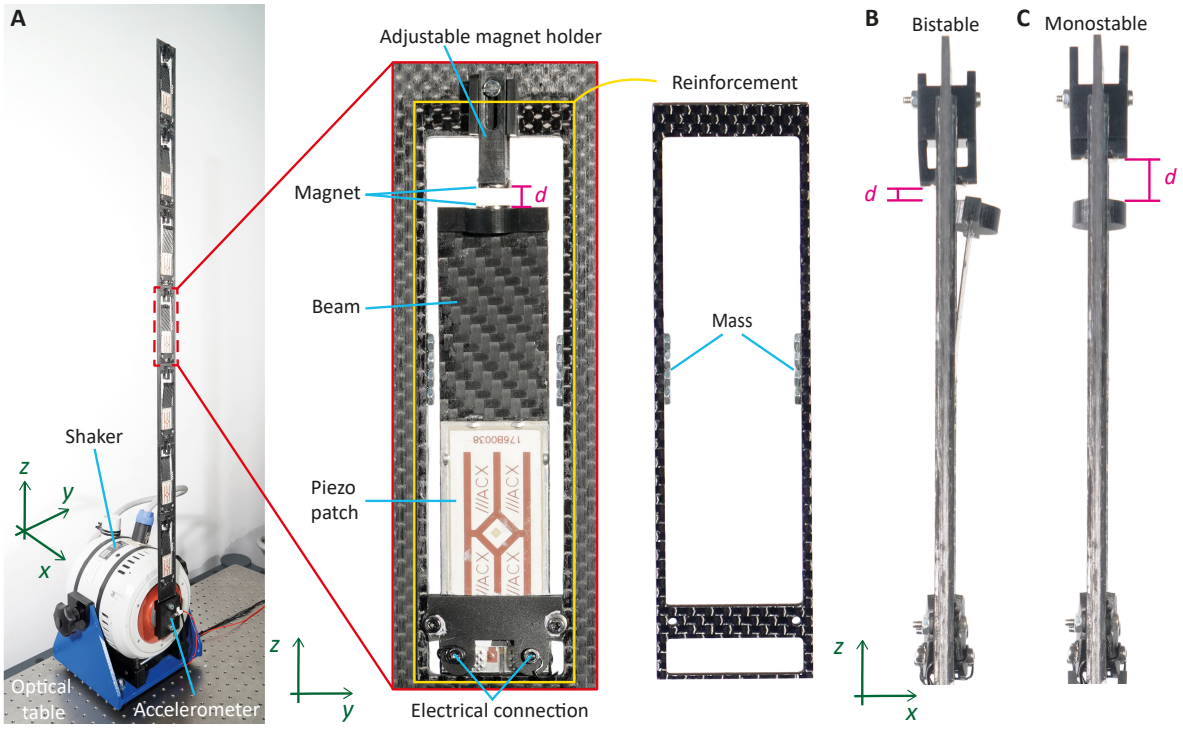


Figure S27: **Experimental setup of the cloaked metastructure equipped with magneto-elastic piezoelectric resonators**. (**A**) Photo of the metastructure clamped on an electromagnetic shaker which is mounted on an optical table. A zoomed-in view of the red-marked region highlights the detailed arrangement of the resonators and the cloaking design. Each resonator is equipped with piezoelectric patches bonded to both surfaces and a cylindrical permanent magnet on its tip. At the bottom, a 3D-printed connector is used to establish the electrical connections to the piezoelectric layers. At the top, an adjustable magnet holder carries an identical magnet, enabling repulsive force interactions between the magnets. This holder allows manual adjustment of the magnet spacing d. Additional structural details of the reinforcement design and the added masses are also shown. (**B**) Photo of the resonator with the magnets positioned close together, creating a bistable state. This setup results in two stable equilibrium points, with one shown in the image (shifted to the right) and the other shifted to the left. (**C**) Photo of the resonator with the magnets positioned farther apart, creating a monostable state. In this case, there is only one stable equilibrium point aligned along the neutral axis of the beam.

Vibration experiments

Experimental setup

Vibration tests are conducted using a shaker TIRA Vib 51144 (frequency range: 2-6500 Hz, rated peak force SINE/RANDOM: 440 N, maximum rated travel: 25.4 mm), equipped with a Power Amplifier TIRA BAA 1000 (frequency range: 2-20000 Hz) and mounted on a Nexus Optical Table from Thorlabs. The amplifier is connected to a vibration controller hardware VR9500 (4 channels, 26000 lines of resolution) to apply a controlled sine excitation. An accelerometer PCB 356A45 (ICP, sensitivity: 99.8 mV/g, measurement range: ± 50 g peak, frequency range: 0.4 to 10 kHz) is used to measure the base acceleration of the metastructure. This sensor provides a feedback signal for a closed-loop control. A sine module software VibrationVIEW is used to interface the controlled excitation. A sine sweep (from 25 Hz to 90 Hz, constant sweep rate of 3 Oct/min, and a fixed acceleration amplitude) is generated to investigate the metastructure behavior over a frequency range. After carefully analyzing the numerical results and confirming consistent responses for both up-sweep and down-sweep excitations, we conducted the experimental analysis using only the up-sweep excitation.

A 3D Digital Image Correlation (DIC-3D) system is used to measure the full-field displacement of the metastructure. This system consists of two high-speed Photron Fastcam Nova S9 cameras (1024x1024 pixel @ 9000 fps) arranged in a stereo configuration to achieve three-dimensional measurement. The cameras are positioned on adjustable tripods at an angle of approximately 30° relative to the specimen and with a distance of 55 cm between them. They are also placed 90 cm away from the center of the specimen. The intrinsic and extrinsic parameters, which include the focal length, lens distortion, stereo angle, image scale, and image center, are defined to maximize the measurement performance. A calibration process is conducted using a calibration target (grid pattern) to define the stereoscopic relationship between the two cameras. The final calibrated setup ensures measurement accuracy with a projection error below 0.1 pixels and a precise spatial measurement.

A speckle pattern is generated using a speckle generator software that randomly creates distributed black dots on a white background. The size of the speckles is chosen to ensure that each dot covers a diameter of 3 to 5 pixels in the captured images. With a 1 MP camera and a field of view of approximately 1 m^2, the spatial scale is about 1 mm/pixel. Thus, the dot diameter must be between 3 mm and 5 mm. We select a diameter of 4 mm. They are randomly distributed with a standard deviation of 75%. The speckle pattern is printed on adhesive sticker paper and carefully bound to the surface of the metastructure to provide accurate 3D displacement tracking.

During the experiments, images are captured at a sampling rate of 1000 fps. The trigger of the cameras is synchronized with the shaker excitation. The exposure time is adjusted to avoid motion blur (1/1000 s). Two blue lights are used to enhance the visibility of the speckle pattern on the

surface by increasing the contrast between the speckled surface and the background. These lights are strategically positioned to minimize shadows, enhance image contrast, and avoid glare.

The DIC processing is performed using VIC-3D software. This analysis involves tracking the full-field displacement in three dimensions. The software computes the displacement field by comparing the reference (undeformed) image with subsequent deformed images during the test. The subset size of 21x21 and step size of 4 pixels are carefully chosen for accurate displacement calculations, ensuring a good balance between resolution and noise sensitivity.

To measure the dissipated voltage across each resistor, we connect voltage probes with a 10x attenuation at each load resistor. The attenuation is applied to prevent overloading in the measurement system by reducing the voltage signal before acquisition. The BNC connectors of the probes are linked to a data acquisition system (DAQ, input range of ± 10V, 7-input channels, from Correlated Solutions). The DAQ is configured to operate in synchronous mode with the DIC system, obtaining synchronized measurements between the analog voltage data and the captured image. The voltage data and displacement fields are recorded at the same sampling rate: 1000 Hz for sweep frequency experiments and 2000 Hz for fixed frequency experiments. This synchronization ensures that the voltage measurements and the corresponding mechanical displacement are accurately recorded at the same time.

Figure S28 shows an illustration of the experimental apparatus and signal flow diagram used during the experimental analysis of the metastructure to measure the full-field displacement and the voltage of each resonator under a controlled base motion excitation.

Figure S29 presents images of the experimental apparatus, including details of the metastructure coated with the speckle pattern and the experimental setup.

Experimental results

The experimental tests are performed to validate the numerical results. A 3D-printed graduated scale is employed to accurately set the magnet spacings. The tests are conducted following the procedure outlined in the previous section.

The bistable configurations are tested at an acceleration amplitude of 2 g, which maintains regular intrawell motion and avoids the strong amplitude-dependent response associated with large-amplitude interwell dynamics. Within this low-amplitude regime, the bistable response is only weakly affected by excitation amplitude. The monostable configurations are tested at 6 g because their dynamics remain regular and comparatively robust to variations in excitation amplitude over the investigated range. The amplitude dependence of both regimes is examined separately in the section Amplitude-dependent dynamics and onset of chaos.

The transmissibility response is derived during post-processing. The power spectral density (PSD) is estimated from the velocity response measured under chirp-up excitation. A Hann window is used and the signal is divided into four segments, with a 50% overlap between the segments. The

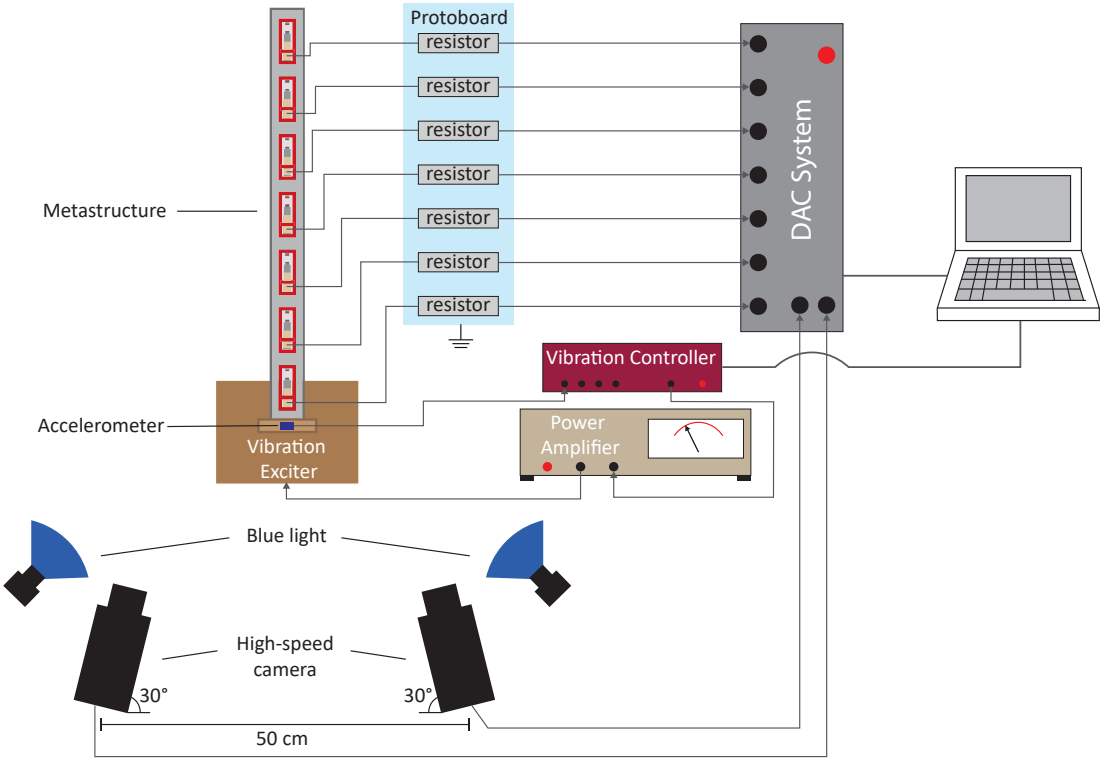


Figure S28: Illustration of the experimental apparatus and signal flow diagram for testing the proposed metastructure.

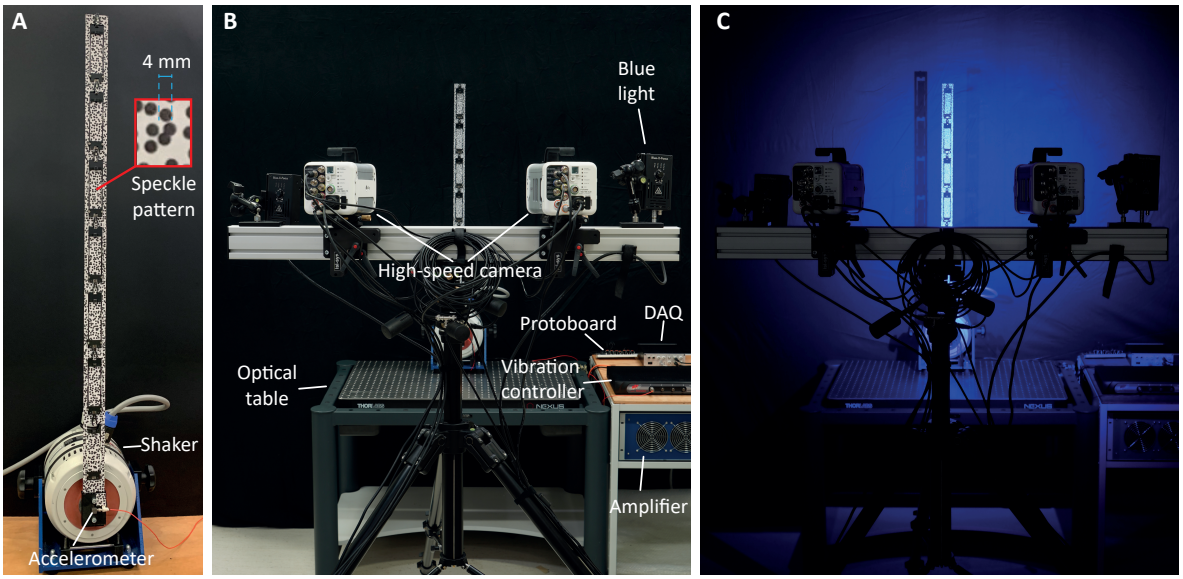


Figure S29: (A) Photo of the metastructure covered by the speckle pattern. The red-marked region shows a zoomed-in view of the black dots with a diameter of 4 mm. (B-C) Photo of the experimental setup without and with blue lights, respectively. These photos demonstrate the positions of the cameras, blue lights, and the metastructure mounted on the shaker.

Fast Fourier Transform (FFT) is computed using the same sampling frequency as the acquisition system. The transmissibility is then obtained by taking the ratio of the PSD of velocity at the tip of the beam to that at the base.

The voltage signals measured across the load resistances are processed using the same PSD estimation procedure. Before spectral estimation, each voltage signal is multiplied by a factor of 10 to compensate for the 10× attenuation introduced by the voltage probes. To reduce the amplification of high-frequency electrical noise associated with this correction, a low-pass filter is applied to the voltage signals before computing the PSD. Because the voltage PSD is expressed in units of voltage squared per frequency, the harvested-power PSD of the j-th resonator channel is obtained as $S_{P,j}(f) = \frac{S_{V,j}(f)}{R_L}$, where $S_{V,j}(f)$ is the voltage PSD and R_L is the load resistance of the corresponding channel. The result is then normalized by the squared base-acceleration amplitude. The normalized total harvested-power PSD is obtained by summing the normalized power PSDs of the independent resonator channels, $\bar{S}_{P,\text{tot}}(f) = \sum_{j=1}^{S} \frac{S_{V,j}(f)}{R_L a_0^2}$. Because each resonator is connected to an independent resistive load, the total harvested power is obtained by summing the individual channel powers. Consequently, the relative phase among the voltage signals does not affect the reported total power.

Initially, all resonators are configured with identical magnet spacings. Various values of the magnet spacing are tested. Experimental transmissibility of the metastructure for various magnet spacings is shown in Fig. S30. The figure illustrates the transmissibility surface across a range of

frequencies. The velocity transmissibility peaks correspond to the amplitude amplification of the tip of the beam. The gray region defines the local resonance bandgap. Similar to the numerical results, the experimental tests confirmed that in the monostable regime decreasing magnet spacing softens the local response and shifts the bandgap downward; after bistability, further decreasing spacing stiffens intrawell motion and shifts the bandgap upward.

The exact transition between monostable and bistable regimes is not directly resolved in the experiments. This is mainly due to the 1 mm increments used for adjusting the magnet spacing, together with geometric asymmetries, assembly tolerances, and manufacturing uncertainties of the prototype. Nevertheless, the experimental results show that, as the magnet spacing approaches the monostable–bistable transition from the monostable side, the attenuation band shifts to lower frequencies. This trend indicates that the repulsive magnetic interaction reduces the effective restoring stiffness of the resonators, thereby lowering their resonant frequency and shifting the associated locally resonant bandgap. This behavior is consistent with the numerical trend observed near the transition between monostable and bistable responses.

Figure S31 shows the experimental normalized total harvested-power PSD for different magnet spacings. The experimental trends are consistent with the numerical results. As the magnet spacing changes, the harvested-power peaks shift in frequency, reflecting the magnetically tuned resonator dynamics. The bistable configurations exhibit multiple peaks distributed over a broader frequency range, whereas the monostable configurations exhibit a more concentrated harvesting response. The largest harvested-power levels are observed for magnet spacings of 5 mm and 7 mm.

Nonlinear systems can exhibit multiple responses that change markedly with the initial conditions or excitation amplitude. For example, bistable oscillators may display intrawell or interwell motion with regular or irregular dynamics. Therefore, understanding the behavior of this structure across different responses is crucial.

The most sensitive parameters for exploring multiple solutions are the initial conditions and the amplitude of excitation. Given the significant challenge of controlling the initial conditions experimentally, this study focuses on varying the amplitude of excitation. The amplitude of excitation can significantly influence the behavior of the system. For instance, when a bistable oscillator is subjected to low excitation amplitudes, the external energy is insufficient to overcome the potential barrier, resulting in oscillation around a single stable equilibrium point. As the external energy increases, the oscillation starts alternating between stable points in either regular or irregular ways. Thus, to investigate how excitation amplitude affects the performance of this metastructure, we test the system under different acceleration amplitudes, specifically 2 g, 6 g, and 9 g, with the resonators configured at a magnet spacing of 3 mm (bistable) and 7 mm (monostable).

Figures S32A and B show the transmissibility for the metastructure when the resonators are under bistable and monostable conditions, respectively. In the bistable condition, we observe that at high excitation amplitudes of 9 g, the bandgap region disappears. The transmissibility response

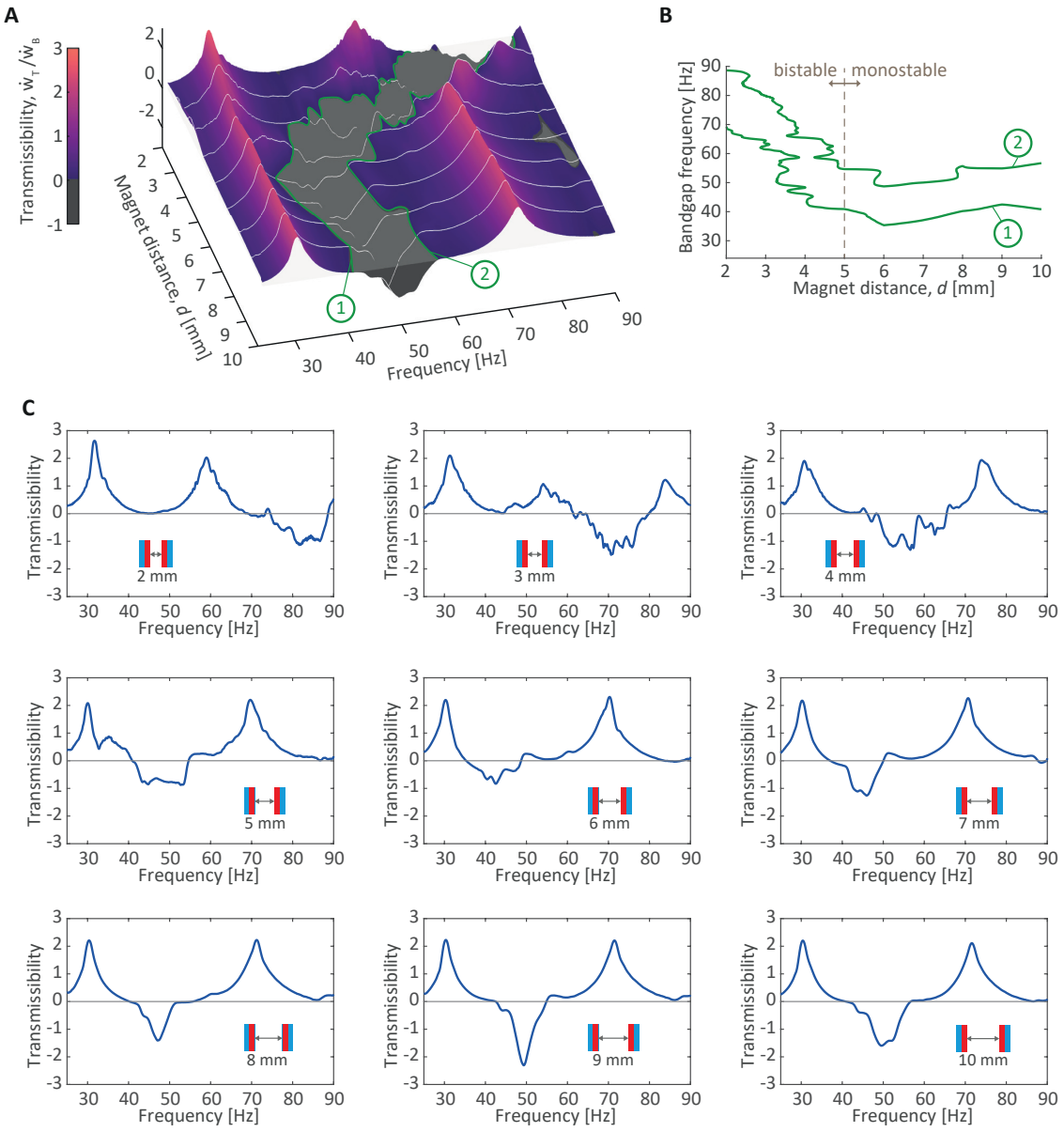


Figure S30: Experimental transmissibility frequency response under varying magnet spacing. (A) Transmissibility of the velocity at the tip of the beam relative to its base across a range of frequencies, shown for different magnet spacings. The gray region highlights the bandgap, where transmissibility is below –0.05 on the logarithmic scale. Green lines mark the lower boundary (line 1) and the upper boundary (line 2) of the bandgap. (B) Bandgap boundary lines as a function of magnet spacing. The vertical gray dashed line represents the transition from bistable to monostable behavior of the resonators. (C) A 2D plot of the transmissibility for different magnet spacings.

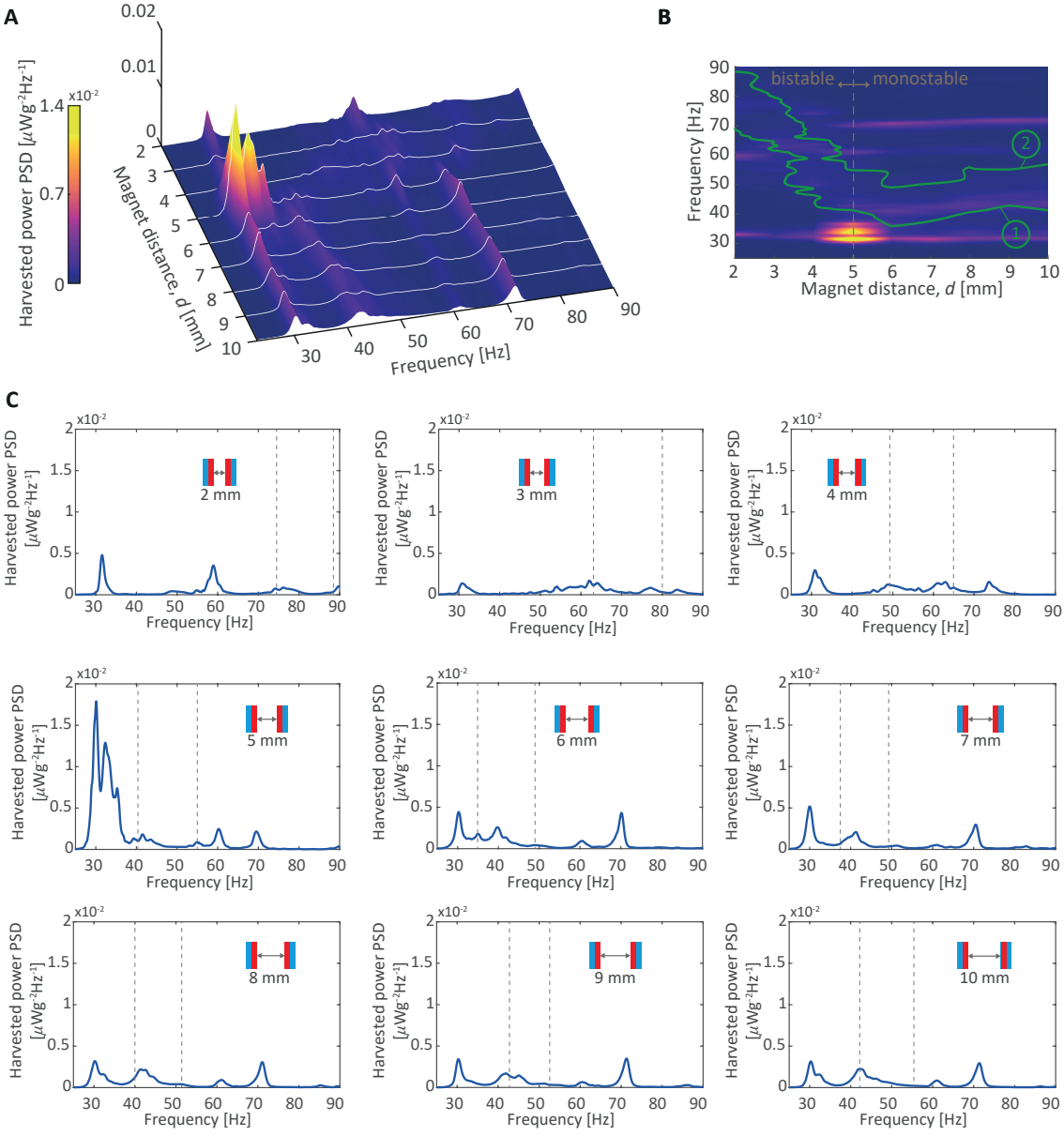


Figure S31: Experimental normalized total harvested-power PSD for different magnet spacings. (A) Normalized total harvested-power PSD surface as a function of frequency and magnet spacing. (B) Top view of the normalized total-power PSD surface with the bandgap boundaries identified for each magnet spacing. (C) 2D normalized total harvested-power PSD curves for selected magnet spacings, with vertical dashed lines indicating the lower and upper limits of the corresponding bandgap regions.

at this condition is nearly flat, with a magnitude close to 1. This indicates that the elastic wave propagation along the beam is not significantly amplified, showing only minor amplification but not comparable to the amplification observed under resonance conditions. At lower excitation amplitudes of 2 g and 6 g, the bandgap is still present. Notably, at 6 g, there are some narrow frequency bands where the transmissibility exceeds one. On the other hand, in the monostable case, the bandgap region remains consistent and clearly defined, regardless of the excitation amplitude.

Figures S32C and D show the normalized total harvested-power PSD for the bistable and monostable configurations, respectively. In the bistable configuration, the response at 9 g exhibits harvested-power contributions over a broader frequency range. However, as shown in Fig. S32A, the attenuation band is no longer preserved at this excitation level. Therefore, although the high-amplitude bistable response can broaden the harvesting bandwidth, it also impairs the vibration-attenuation functionality. In the monostable configuration, the normalized harvested-power peaks remain comparatively consistent across the tested excitation amplitudes, with the response concentrated within a narrower frequency range.

A single fixed-frequency excitation test is conducted to investigate the dynamic behavior at the local resonance bandgap condition for different acceleration values. Frequencies of 71 Hz and 45 Hz are used to excite the bistable and monostable configurations, respectively, that correspond to the frequency value within their respective bandgap zones. The sampling frequency for the measurement is increased to 2000 Hz to improve the signal resolution. A high time resolution is essential for time series analysis. The displacement and velocity responses of the resonators, along with the generated voltage, are measured.

We use the Poincaré map of these time series to experimentally verify and characterize the dynamic behavior of the resonators. The Poincaré map is a common method in dynamical systems analysis to investigate the projection of the trajectory of the system onto a low-dimensional subspace. Thus, we calculate the map by selecting a cross-section of its phase space that corresponds to the excitation frequency and observing the evolution of state points on that cross-section (*21*). The resulting map helps distinguish between periodic and irregular system responses. For example, when the trajectory intersects the cross-section at a single point, the system exhibits regular period-1 behavior. Two intersection points indicate period-2 motion, while multiple intersections suggest an irregular motion. This analysis provides a deeper understanding of the dynamic characteristics of the system.

To calculate the intersection points for the Poincaré map, we increase the time resolution of the response by using spline interpolation. This approach is effective due to the already high sampling frequency of the time series. However, it is necessary to ensure that there are enough samples available to accurately characterize the dynamic behavior. To further enhance the quality of the signal, we apply a Savitzky-Golay filter with a polynomial order of 3 and a frame length of 13 points. This filter helps to remove noise disturbances from the measurements. Additionally, we use

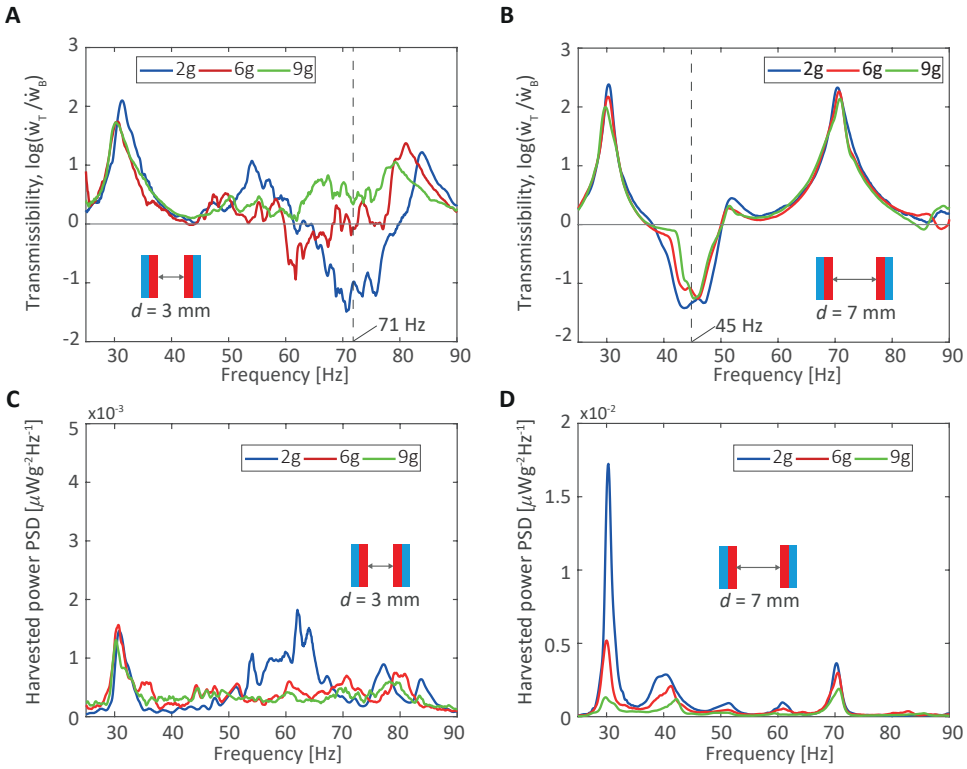


Figure S32: Amplitude dependence of the metastructure in bistable and monostable regimes. Experimental transmissibility frequency response at acceleration levels of 2 g, 6 g, and 9 g for (A) the bistable configuration with magnet spacing of 3 mm and (B) the monostable configuration with magnet spacing of 7 mm. Dashed vertical lines at 71 Hz for the bistable case and 45 Hz for the monostable case indicate the frequencies analyzed further below. (C,D) Normalized total harvested-power PSD for the bistable and monostable configurations, respectively.

singular value decomposition of a Hankel matrix with the time-series embedding to reconstruct a denoised time series by truncating smaller singular values. This combined methodology significantly improves the overall signal quality, minimizing noise interference that could impact the construction of the Poincaré map while preserving the dynamic characteristics of the motion.

Figure S33 shows the phase space of displacement and velocity with the Poincaré maps for resonators in the bistable configuration (magnet spacing of 3 mm) under accelerations of 2 g, 6 g, and 9 g, with a fixed frequency excitation of 71 Hz. For 2 g and 6 g, the resonators exhibit a single orbit with one intersection point, indicating a periodic motion with one period. Notably, the first resonator has a higher energy orbit compared to those located closer to the tip of the beam. This occurs because the energy propagation within the bandgap is attenuated along the length of the structure, resulting in weaker excitation for the resonators nearer to the tip. Additionally, we observe stable orbits concentric to the equilibrium point (near 0 mm displacement), characterizing periodic intrawell motion for all resonators. At excitation of 9 g, the results show irregular motions, as indicated by multiple intersection points on the Poincaré map. The resonators have multiple orbits with varying energy levels, concentric to two equilibrium points at 0 mm and 5 mm. This behavior indicates irregular interwell motion. This high amplitude of oscillation is observed for all resonators, indicating that energy is not attenuating along the length of the beam. It confirms that for high excitations, the bandgap disappears. The phase spaces also reveal asymmetry in the restoring force between one stable equilibrium point and another because the orbits around one equilibrium point show more energy than those around the other. This asymmetry is especially evident in resonators 1, 3, and 5 and can be attributed to geometric variations, assembly imperfections, material properties, or manufacturing uncertainties.

Figure S34 shows the phase space of displacement and velocity with the Poincaré maps for resonators in the monostable configuration (magnet spacing of 7 mm) under accelerations of 2 g, 6 g, and 9 g, with a fixed frequency excitation of 45 Hz. In all accelerations, the resonators exhibit a single orbit with one intersection point, indicating a periodic motion with one period. The first resonator has a higher energy orbit compared to those located closer to the tip of the beam. There is no indication of irregular motion. The orbits for all resonators are concentric around a single equilibrium point, confirming the monostable regime.

To confirm the presence of chaotic behavior, we apply the 0-1 test for chaos. Details of this test are provided in the section '0–1 Test for Chaos'. We use a sampling of 1000 to guarantee convergence of the classifier.

Figure S35 shows the results of this test for the displacement of the resonators under 2 g, 6 g, and 9 g. Figure S35A shows the results for the bistable resonators. At 2 g and 6 g, the values of the test are below 0.2, classifying the motion of the resonators as regular. At 9 g, the values of the test are above 0.8, indicating chaotic motion. Figure S35B shows the results for the monostable resonators. For all excitation levels, the values of the test are below 0.2, classifying the dynamic

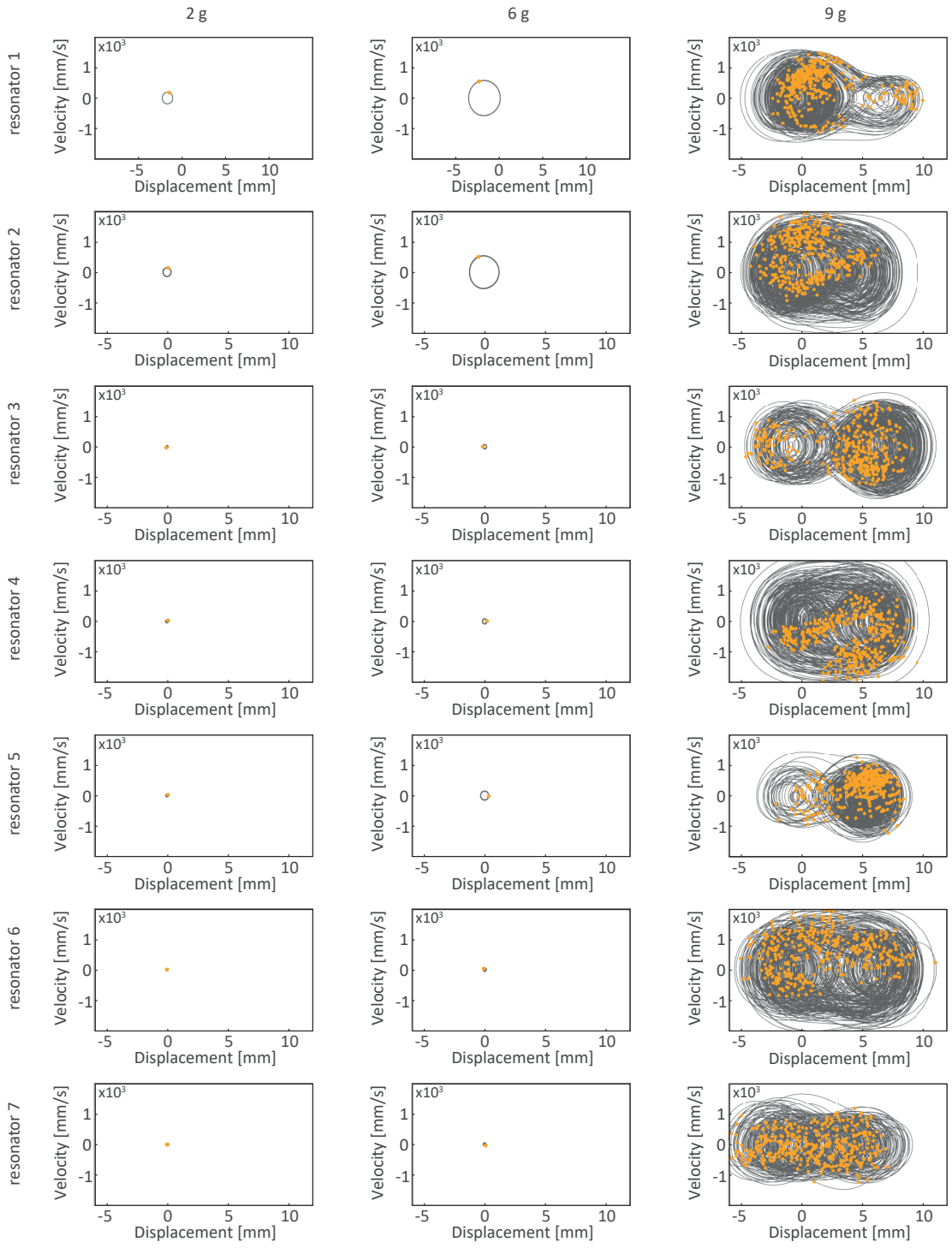


Figure S33: Phase portrait and Poincaré map for bistable resonators under accelerations of 2 g, 6 g, and 9 g at a frequency of 71 Hz. The phase portrait orbits are represented by gray lines, while the Poincaré points are shown as orange dots. The first column displays the results for an acceleration of 2 g, the second column for 6 g, and the third column for 9 g. The resonators are presented from top to bottom, with resonator 1 at the top and resonator 7 at the bottom.

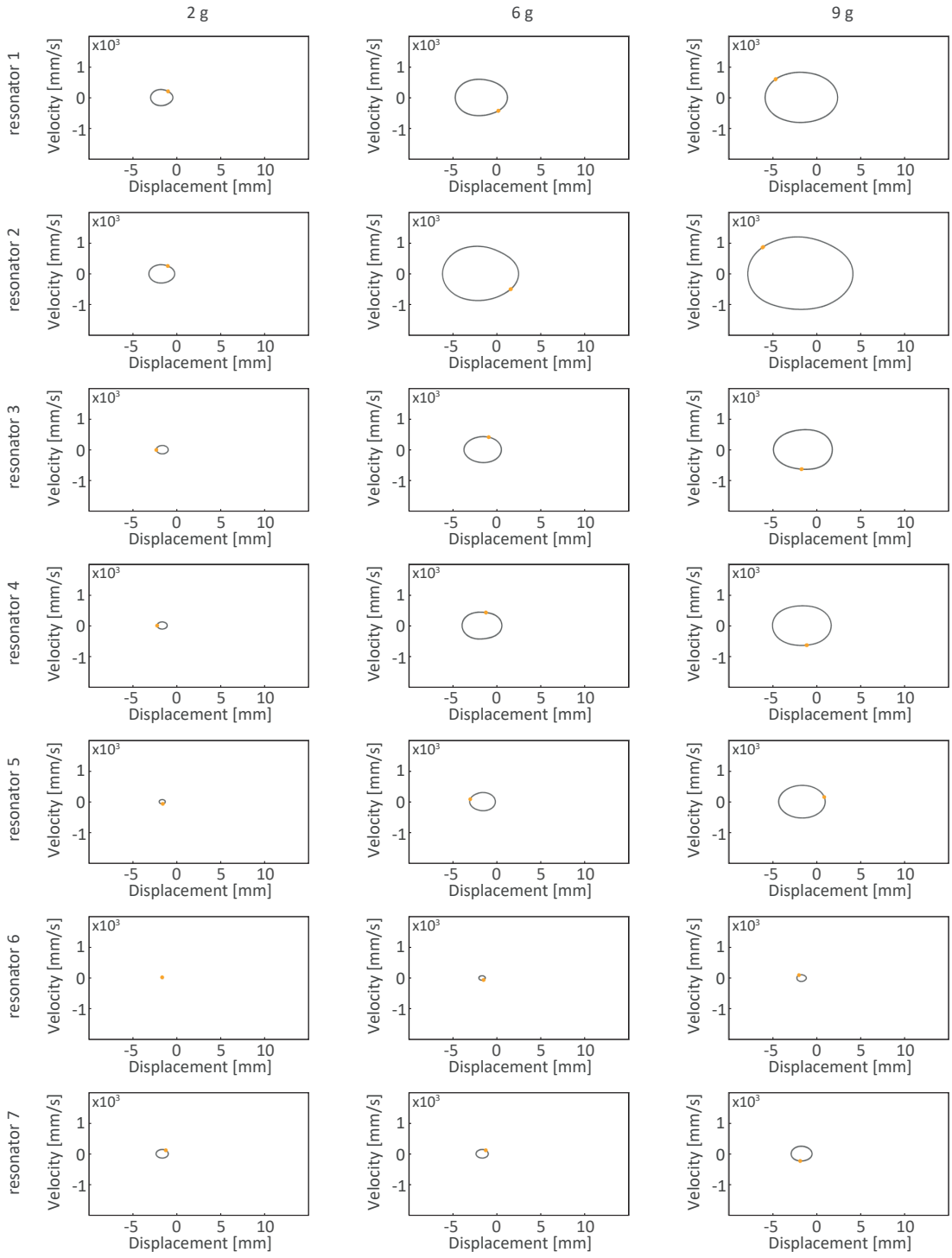


Figure S34: Phase portrait and Poincaré map for monostable resonators under accelerations of 2 g, 6 g, and 9 g at a frequency of 45 Hz. The phase portrait orbits are represented by gray lines, while the Poincaré points are shown as orange dots. The first column displays the results for an acceleration of 2 g, the second column for 6 g, and the third column for 9 g. The resonators are presented from top to bottom, with resonator 1 at the top and resonator 7 at the bottom.

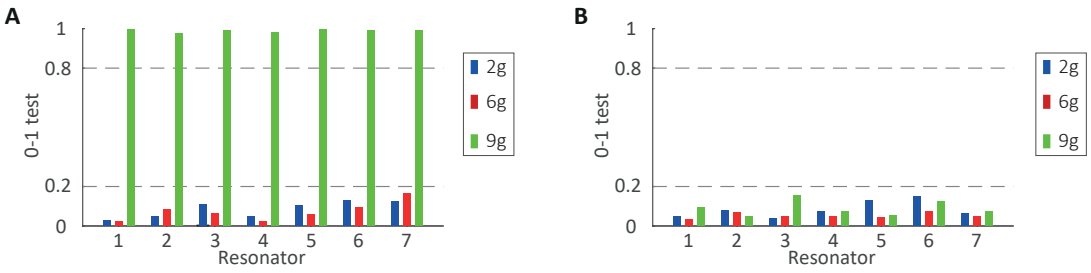


Figure S35: 0-1 test for chaos based on the experimental displacement of the resonators at (A) bistable and (B) monostable configurations under accelerations of 2 g, 6 g, and 9 g.

series as regular. Therefore, according to the 0-1 test for chaos based on the time series of the resonators and the observations from the transmissibility, we confirm that the presence of chaos in the response of the resonators disrupts the local resonance bandgap.

The experimental findings are consistent with the numerical results. Both analyses indicate that this chaotic behavior disrupts bandgap formation, resulting in a passband without pronounced wave amplification. Additionally, in terms of energy harvesting, experimental and numerical results confirm that under the chaotic behavior of the resonators, the energy generation improves when compared to the bandgap condition. The experimental and numerical results also show higher harvested power during chaotic motion than under the regular bandgap condition, consistent with the larger oscillation amplitudes.

To further investigate the physical mechanism associated with the loss of the attenuation band under chaotic motion, we evaluated the phase relationship between the resonator and the host beam directly from the experimentally measured displacement time histories. The displacement of resonator 1 and that of the host beam at the corresponding attachment position were detrended and bandpass filtered around the excitation frequency to isolate the dominant forced-response component. Their instantaneous phases were then obtained using the Hilbert transform, and the corresponding phase difference was evaluated over the same steady-state time interval. A nearly constant phase difference indicates a stable host–resonator phase relationship, whereas irregular temporal variations indicate that this relationship is no longer maintained.

The results in Fig. S36 show that, for the identical 3 mm bistable configuration at 71 Hz, the host–resonator phase relationship remains stable under 2 g excitation, when the resonator exhibits periodic intrawell motion. Under 9 g excitation, when chaotic interwell motion occurs, the phase difference varies irregularly with time. This behavior supports the interpretation that chaotic motion disrupts the stable host–resonator interaction required for locally resonant attenuation.

In contrast, the identical 7 mm monostable configuration at 45 Hz, shown in Fig. S37, maintains a stable phase relationship under both 2 g and 9 g excitation, consistent with its periodic response and preserved attenuation behavior.

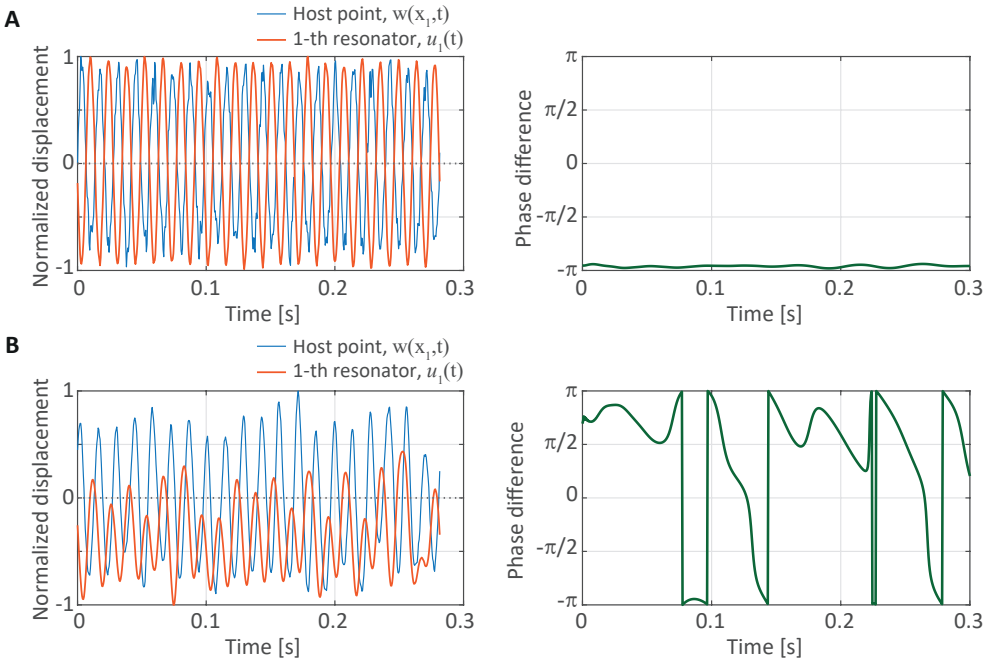


Figure S36: Experimental host–resonator phase relationship for the identical 3 mm bistable configuration excited at 71 Hz under (A) 2 g and (B) 9 g. Each panel shows the normalized displacement time histories of resonator 1 and the host beam at the corresponding attachment point, together with their time-dependent phase difference. The displacement signals are normalized by their respective maximum absolute values.

These experimental observations are consistent with the numerical results and with the Poincaré and 0–1 test for chaos analyses. Together, they indicate that the transition to chaotic interwell motion weakens the coherent local-resonance mechanism and leads to the disappearance of the attenuation band.

We next experimentally test the metastructure with nonidentical magnet spacings. Seven configurations combining bistable and monostable resonators are considered, as shown in Fig. S38A. These configurations are designed to investigate how spatially distributed nonlinear resonator states affect vibration attenuation and energy harvesting.

The transmissibility and normalized total harvested-power PSD responses for each configuration are shown in Fig. S38. An excitation amplitude of 2 g was imposed to maintain the resonators within the regular low-amplitude regime and avoid amplitude-dependent effects associated with large-amplitude nonlinear motion. The nonidentical configurations generate broad attenuation regions and, in some cases, multiple separated attenuation intervals, indicating their ability to attenuate vibrations over different frequency ranges. For example, configuration N2 exhibits an attenuation band starting near 40 Hz and extending to approximately 73 Hz, whereas configuration N5 exhibits attenuation regions that extend from approximately 40 Hz to 82 Hz. Narrow transmissibility peaks with relatively low amplitudes are observed between adjacent attenuation intervals, indicating

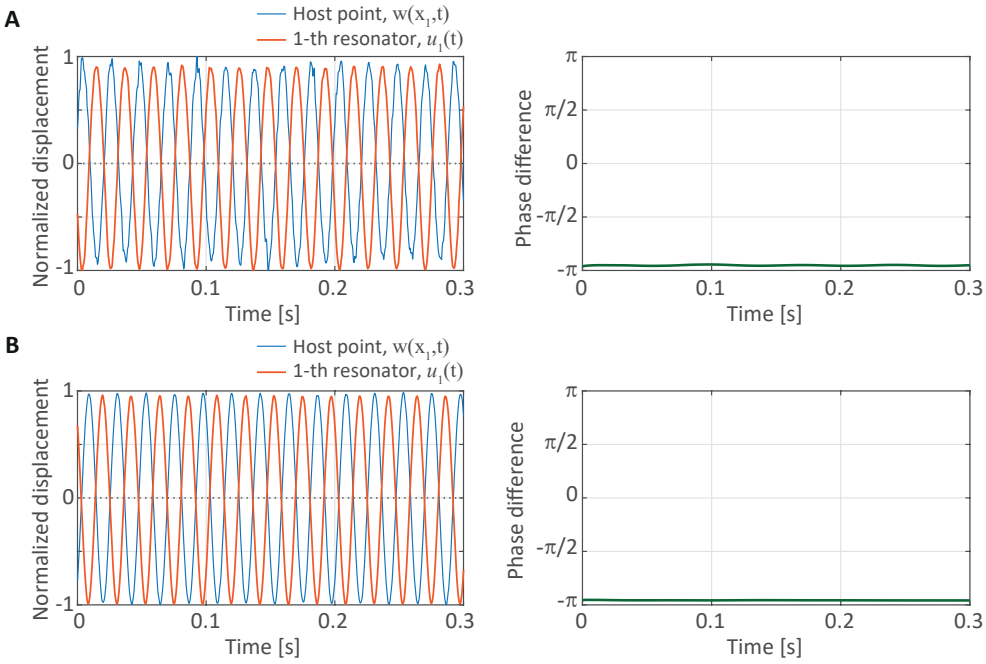


Figure S37: Experimental host–resonator phase relationship for the identical 7 mm monostable configuration excited at 45 Hz under (A) 2 g and (B) 9 g. Each panel shows the normalized displacement time histories of resonator 1 and the host beam at the corresponding attachment point, together with their time-dependent phase difference. The displacement signals are normalized by their respective maximum absolute values.

partial recovery of vibration transmission between locally resonant regions.

The results are consistent with the tuning behavior observed for identical resonator configurations. Resonators with smaller magnet spacings, associated with bistable behavior, contribute mainly to attenuation at higher frequencies, whereas resonators with larger magnet spacings, associated with monostable behavior, contribute to attenuation at lower frequencies. Therefore, combining different magnet spacings allows the attenuation regions to be redistributed and broadened compared with metastructures composed of identical resonators.

In terms of energy harvesting, the nonidentical configurations produce harvested-power contributions over multiple frequency intervals. This behavior results from the distribution of resonator frequencies introduced by the different magnet spacings. For instance, configuration N4 exhibits several harvested-power peaks distributed over a broad frequency range, indicating that mechanically programmed nonidentical resonators can broaden the frequency range over which electrical power is generated. This feature is relevant for practical excitation conditions in which the dominant vibration frequency is not fixed.

Next, the performance of the nonidentical configurations is compared with that of metastructures with identical magnet spacings. The results are represented in a two-dimensional performance map that separates the vibration-attenuation and energy-harvesting metrics. The attenuation performance

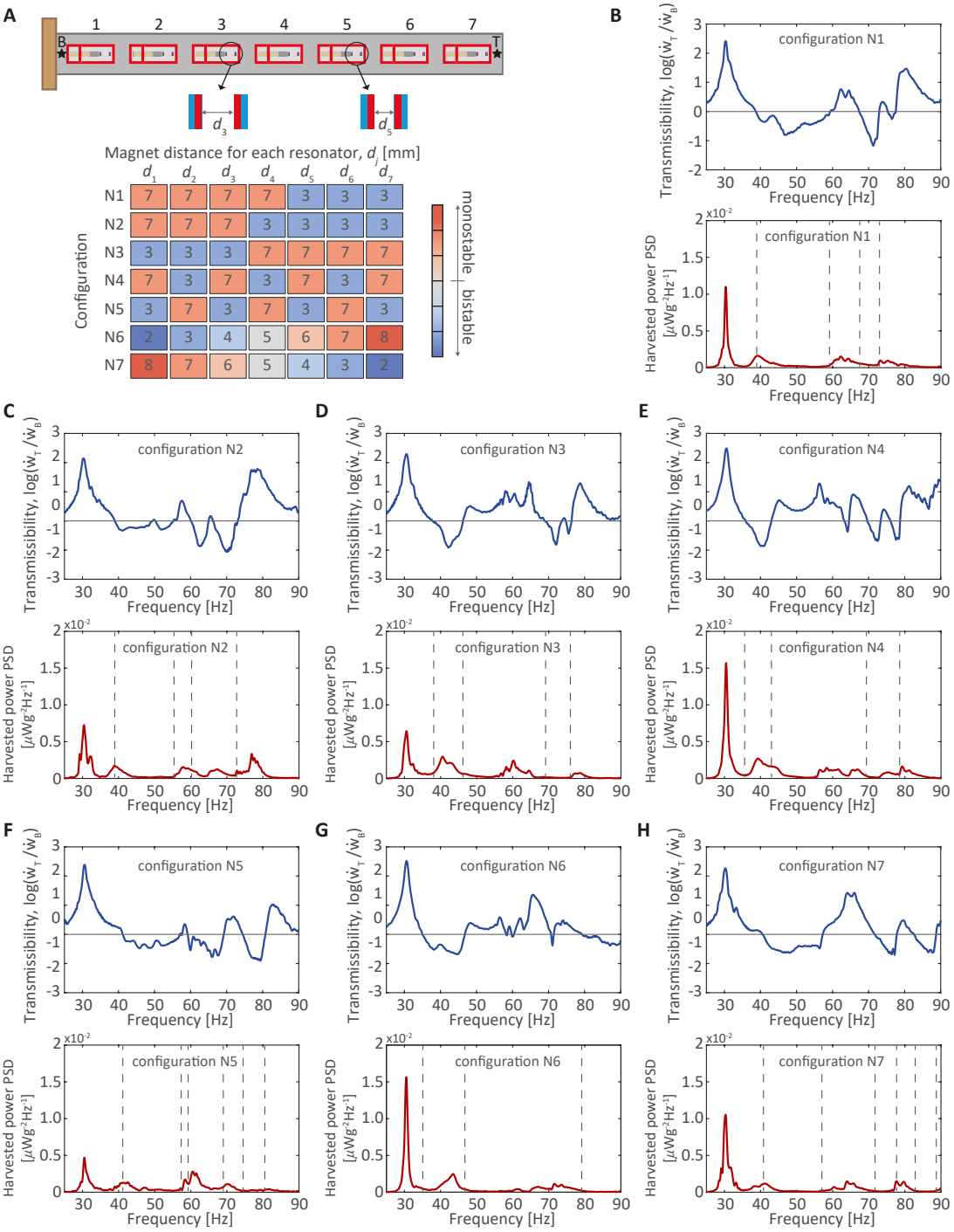


Figure S38: Vibration attenuation and energy-harvesting performance of the metastructure with nonidentical magnet spacings. (A) Tested configurations obtained by varying the magnet spacing of the resonators. Transmissibility response (top) and normalized total harvested-power PSD (bottom) for configurations (B) N1, (C) N2, (D) N3, (E) N4, (F) N5, (G) N6, and (H) N7. Vertical dashed lines indicate the boundaries of the identified attenuation regions.

is quantified by the bandgap bandwidth B, obtained from the frequency intervals satisfying $\log_{10} T < -0.05$. The energy-harvesting performance is quantified by the area A_P under the normalized total harvested-power PSD over the tested frequency range. The two metrics are normalized using distinct identical-configuration references. The bandgap bandwidth is normalized by the identical bistable configuration with a magnet spacing of 3 mm, which provides the reference attenuation bandwidth. The harvested-power area is normalized by the identical monostable configuration with a magnet spacing of 7 mm, which provides the reference harvesting response. Therefore, values larger than unity indicate improvement relative to the corresponding reference metric.

Figure S39 presents the experimental performance map for the tested nonidentical configurations. Configurations located in the upper-left region improve the attenuation bandwidth but reduce the harvested-power area relative to the harvesting reference. Configurations located in the lower-right region increase the harvested-power area but reduce the attenuation bandwidth relative to the bandgap reference. Configurations located near or above both reference lines provide a more balanced multifunctional response.

The results show a trade-off between vibration attenuation and energy harvesting. Configuration N5 provides the largest attenuation bandwidth among the tested nonidentical cases, but it also presents a reduced harvested-power area. In contrast, configuration N4 provides the strongest harvesting response, with a broader distribution of harvested-power contributions over frequency, but with lower attenuation bandwidth than the best suppression-oriented configuration. Configuration N2 offers a more balanced response, combining a broad attenuation region with a harvested-power area that is not strongly reduced relative to the harvesting reference.

These results demonstrate that nonidentical magnet-spacing distributions can be used to prioritize different functionalities. Suppression-oriented configurations are advantageous when vibration attenuation is the primary objective, whereas harvesting-oriented configurations are more suitable when electrical generation over a broader frequency range is desired. More balanced configurations provide a compromise between both functions. Together with the numerical results, the experimental performance map confirms that spatially programming the magnet spacings provides a practical strategy for tuning the multifunctional response of the metastructure beyond what is obtained with identical resonators.

Energy harvesting demonstration and low-power sensing potential

To demonstrate the energy harvesting capability of the metastructure, the harvested electrical output is used to power light-emitting diodes (LEDs) during vibration excitation. Seven yellow LEDs are connected to the seven independent resonator channels, so that each resonator drives one LED through its corresponding electrical circuit. This arrangement provides a visual indication of the spatial distribution of the harvested energy along the metastructure. The LEDs are arranged from left to right following the resonator order, with resonator 1 located closest to the fixed base and

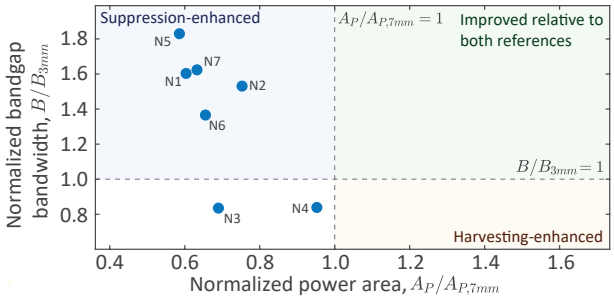


Figure S39: Experimental performance map of the metastructure with nonidentical magnet spacings. The horizontal axis shows the normalized harvested-power area, $A_P/A_{P,7\text{mm}}$, where $A_{P,7\text{mm}}$ is obtained from the identical monostable configuration with magnet spacing of 7 mm. The vertical axis shows the normalized bandgap bandwidth, $B/B_{3\text{mm}}$, where $B_{3\text{mm}}$ is obtained from the identical bistable configuration with magnet spacing of 3 mm. Dashed lines indicate the reference value of unity for each metric.

resonator 7 located closest to the free end.

The demonstration is performed using the metastructure with identical magnet spacing of 7 mm, which corresponds to a monostable configuration. Two excitation conditions are considered. The first condition is selected near resonance at 29 Hz, where the host beam vibration and the resonator response are large. The second condition is selected inside the bandgap region at 41 Hz, where the transmitted vibration along the host beam is reduced by the locally resonant attenuation mechanism. Figure S40 presents selected frames from Movie S1, showing the LED activation at different excitation amplitudes for the resonance and bandgap conditions. These two cases illustrate that the metastructure can generate visible electrical output near resonance and inside the attenuation band.

Figure S40A shows the LED response near the resonance condition. As the excitation amplitude increases, the LEDs turn on progressively, indicating that the resonators generate sufficient alternating voltage to activate the LEDs. Differences in LED brightness are observed among the channels. These differences are associated with the spatial distribution of the vibration mode and the local motion of each resonator. Therefore, the LED brightness provides a qualitative visualization of the harvested energy distribution.

Figure S40B shows the LED response inside the bandgap region. In this case, the vibration transmitted toward the beam tip is attenuated, but several LEDs still turn on, demonstrating that part of the mechanical energy is localized and converted by the embedded resonators. This result is important because it shows that the metastructure can preserve energy harvesting functionality even when operating in a vibration attenuation regime. Thus, the bandgap does not completely suppress the electromechanical conversion; instead, it redistributes the mechanical energy into resonator motion while reducing transmission through the host structure.

The LED demonstration provides a qualitative visualization of the harvested electrical output. A



Figure S40: LED demonstration for the metastructure with identical magnet spacing of 7 mm under two excitation conditions, (A) near resonance at 29 Hz and (B) inside the bandgap region at 41 Hz. The LEDs are connected to the independent resonator channels and arranged according to the resonator positions from the fixed base to the free end. The frame sequences show the activation of the LEDs as the excitation amplitude increases, providing a qualitative visualization of the spatial distribution of the harvested electrical output.

quantitative electrical power generated under the two excitation conditions with a fixed amplitude of 6 g is summarized in Table S6. Near resonance at 29 Hz, the total harvested power reaches 10.67 μW. Inside the bandgap region at 41 Hz, the metastructure still generates 2.05 μW, even though the vibration transmitted through the host beam is attenuated.

In the LED demonstration, the LEDs are activated directly by the alternating voltage generated by the piezoelectric resonators, since the LEDs themselves allow current to pass during part of each voltage cycle. Continuous operation of autonomous electronic devices, however, requires a controlled DC supply. For this purpose, the alternating electrical output must be rectified, stored, and regulated before being supplied to electronic loads. Therefore, the net DC power available after the power-management stage is lower than the AC power measured across the load resistances.

The conversion efficiency depends on the electrical interface, including the rectifier topology, input-voltage amplitude and storage voltage. As a datasheet-based reference, the bq25570 energy-harvesting power-management circuit from Texas Instruments reports high conversion efficiency under specified operating conditions. From the charger-efficiency curves, considering a rectified input voltage of approximately 0.4 V and a storage voltage of 3.0 V, an efficiency of about 75% can be used as an illustrative estimate. Using this efficiency, the resonance condition would provide an estimated DC power of approximately 8.0 μW. For the bandgap condition, applying the same efficiency gives approximately 1.54 μW. The bandgap estimate should be interpreted with caution because the datasheet does not report an efficiency curve exactly for this power operating point; the same 75% value is used only as a reference for power-budget comparison. The estimated DC powers therefore provide order-of-magnitude references, whereas the actual regulated output must be measured with the final rectification, storage, and power-management circuit.

For comparison with low-power electronics, the estimated DC powers can be expressed as equivalent currents for a regulated 3.3 V supply. Under this assumption, the resonance condition corresponds to approximately 2.43 μA, while the bandgap condition corresponds to approximately 0.47 μA. These current levels provide a practical reference for comparing the harvested output with the requirements of ultra-low-power sensing devices.

Table S6: Quantitative electrical output measured during the LED demonstration and estimated DC power after power management. The measured P_{tot} corresponds to the AC power dissipated in the load resistances. The estimated DC power is calculated using an illustrative 75% conversion efficiency based on the bq25570 charger-efficiency curves for comparable input-voltage and storage-voltage conditions. The equivalent current is calculated from the estimated DC power using $I_{\mathrm{DC,eq}} = P_{\mathrm{DC}}/3.3\ \mathrm{V}$.

Condition	**Frequency**	P_{tot}	**Estimated** P_{DC}	**Estimated** $I_{\mathrm{DC,eq}}$ **at 3.3 V**
Resonance	29 Hz	10.67 μW	8.0 μW	2.43 μA
Bandgap	41 Hz	2.05 μW	1.54 μW	0.47 μA

Table S7 lists datasheet-reported operating modes of commercial low-power sensors, providing a power-budget reference for identifying sensing functions that could be supported directly, intermittently, or after energy accumulation in a storage element. The comparison with these commercial sensors shows that the estimated DC power levels are compatible with several ultra-low-power operating modes, especially sleep, wake-up, and low-rate sensing states. The resonance condition provides a higher power budget and could support intermittent measurements from low-power environmental, inertial, or ambient-light sensors when combined with suitable energy storage. The bandgap condition provides a smaller but still useful power budget, making it more appropriate for energy accumulation, standby operation, wake-up monitoring, or sparse sensing events. In both cases, wireless transmission, data logging, or display operation would require duty-cycled operation, in which energy is first accumulated in a storage element and then released during short active intervals. These estimates indicate that the metastructure can generate useful μW-level electrical power while preserving vibration-attenuation functionality in the bandgap regime.

Table S7: Examples of commercial low-power sensors with datasheet-reported operating modes comparable to the estimated DC power generated by the metastructure. The power values are calculated from datasheet current values using $P = VI$. When the datasheet directly reports the average power, the reported value is used. The comparison considers only the sensor integrated circuit and does not include microcontrollers, wireless transmission, data logging, displays, or additional interface losses.

Device	**Datasheet operating mode**	**Supply voltage**	**Datasheet current**	**Power level**
ADXL362 accelerometer	Motion-triggered wake-up mode	2.0 V	270 nA	0.54 μW
ADXL362 accelerometer	Measurement mode at 100 Hz output data rate	2.0 V	< 2 μA	< 4.0 μW
HDC1080 humidity and temperature sensor	Sleep mode	3.3 V	100 nA	0.33 μW
HDC1080 humidity and temperature sensor	Average supply current for relative-humidity and temperature measurement at 1 sps	3.3 V	1.3 μA	4.29 μW
SHTC3 humidity and temperature sensor	Sleep mode	3.3 V	0.3 μA	0.99 μW
SHTC3 humidity and temperature sensor	Low-power measurement mode, one measurement per second	3.3 V	0.5 μA	1.6 μW
BME280 humidity, pressure, and temperature sensor	Sleep mode	3.3 V	0.1 μA	0.33 μW

BME280 humidity, pressure, and temperature sensor	Average current at 1 Hz for humidity, pressure, and temperature measurements	3.3 V	3.6 μA	11.88 μW
OPT3001 ambient light sensor	Low operating-current mode	3.3 V	1.8 μA	5.94 μW

The power-budget comparison above is based on a specific reference condition, using the identical 7 mm monostable configuration under selected resonance and bandgap excitations. These values therefore represent a demonstrated baseline, not the upper limit of the metastructure. The mechanically programmed configurations show that the magnet spacing distribution can redistribute the resonator dynamics and shift the system toward harvesting-enhanced regimes. This provides a practical route to increase the generated power for a target vibration environment while retaining vibration-attenuation functionality. Hence, the estimated power levels reported here already fall within the range of ultra-low-power sensing modes, and the mechanically programmed nature of the metastructure offers additional potential for improving the available power through configuration design.

0-1 test for chaos

The 0-1 test for chaos is a statistical method based on time-series analysis to classify the dynamic behavior of the resonators. Unlike the Lyapunov exponent method, which requires phase space reconstruction and eigenvalue calculation at a high computational cost, the 0-1 test for chaos offers a more computationally efficient approach (*22*). This method identifies chaotic or non-chaotic behavior by performing a Euclidean extension transformation of the time series. A statistical classifier, derived from the covariance and variance of these transformed coordinates, is then used to categorize the dynamic behavior (*23*). Classifier values below 0.2 indicate regular motion, while values above 0.8 suggest chaotic behavior. Values between 0.2 and 0.8 are considered inconclusive. This methodology is applied to the displacement time series of the resonators.

The 0-1 test for chaos maps the time series $x(t)$ into a pair of transformed coordinates:

$$p_n(c) = \sum_{j=1}^{n} x(t_j)\, \cos(j\, c)\,, \tag{S59}$$

$$q_n(c) = \sum_{j=1}^{n} x(t_j)\, \sin(j\, c)\,, \tag{S60}$$

where c is a random value uniformly drawn from the interval $[0, 2\pi)$ and $n = 1, 2, \ldots, N$. For regular (non-chaotic) behavior, the coordinates display bounded motion, while in chaotic systems, they asymptotically resemble Brownian motion.

The mean square deviation

$$M_n(c) = \lim_{N\to\infty} \frac{1}{N} \sum_{j=1}^{N} \left(\left[p_{j+n}(c) - p_j(c) \right]^2 + \left[q_{j+n}(c) - q_j(c) \right]^2 \right) \tag{S61}$$

is used to identify diffusive or non-diffusive behavior. The classifier

$$K_c = \lim_{N\to\infty} \frac{Cov(\overline{t_n}, \overline{M_n})}{\sqrt{Var(\overline{t_n})\, Var(\overline{M_n})}}, \tag{S62}$$

where $\overline{M_n} = (M_1, M_2, \ldots, M_n), \overline{t_n} = (t_1, t_2, \ldots, t_n), Cov$ and Var denoting covariance and variance operators, is computed for several values of c. The median result is taken to classify the dynamic behavior as chaotic ($K > 0.8$), regular ($K < 0.2$), or inconclusive ($0.2 < K < 0.8$).

Caption for Movies

Caption for Movie S1. Vibration-driven powering of seven LEDs by the metastructure. The video shows the metastructure with identical monostable resonators at a magnet spacing of 7 mm, excited near resonance at 29 Hz and inside the bandgap at 41 Hz. For each frequency, the excitation amplitude is increased and then decreased between 0 g and 8 g. The seven LEDs are connected to the independent resonator channels and arranged from left to right according to the resonator positions, with resonator 1 nearest the clamped base and resonator 7 closest to the free tip.

Caption for Movie S2. Vibration test of the metastructure with monostable resonators at a magnet spacing of 7 mm. The video shows the metastructure response to a fixed excitation frequency under resonance condition at 31 Hz and bandgap condition at 45 Hz.

Caption for Movie S3. Vibration test of the metastructure with bistable resonators at a magnet spacing of 3 mm. The video shows the metastructure response to a fixed excitation frequency under resonance condition at 31 Hz and bandgap condition at 71 Hz.

Caption for Movie S4. Vibration test of the metastructure with bistable resonators at a magnet spacing of 3 mm under increasing excitation amplitude within the bandgap region. The video demonstrates the amplitude dependence of the metastructure with bistable resonators. The test is conducted at a fixed frequency of 71 Hz while gradually increasing the amplitude from 2 g to 10 g. At lower amplitudes, the bandgap phenomenon is observed; however, as the amplitude increases, the bandgap effect disappears, and the resonators show chaotic motion.

Caption for Movie S5. Digital image correlation results from the vibration test. The video shows the metastructure response measured using 3D digital image correlation.

Caption for Movie S6. Assembly of the metastructure: exploded view animation. The video provides a detailed demonstration of the metastructure assembly.

References and Notes

1. K. Mikoshiba, J. M. Manimala, C. Sun, Energy harvesting using an array of multifunctional resonators. *Journal of Intelligent Material Systems and Structures* **24** (2), 168–179 (2013), doi:10.1177/1045389X12460335.

2. Y. Li, E. Baker, T. Reissman, C. Sun, W. K. Liu, Design of mechanical metamaterials for simultaneous vibration isolation and energy harvesting. *Applied Physics Letters* **111** (25), 251903 (2017), doi:10.1063/1.5008674.

3. X. Xu, *et al.*, Multifunctional Metamaterials for Energy Harvesting and Vibration Control. *Advanced Functional Materials* **32**, 2107896 (2022), doi:10.1002/adfm.202107896.

4. C. Xu, S. Chen, C. H. Wang, Y. Yang, L. Zhao, Amplitude-robust metastructure with combined bistable and monostable mechanisms for simultaneously enhanced vibration suppression and energy harvesting. *Applied Physics Letters* **122** (15), 151701 (2023), doi:10.1063/5.0136134.

5. C. Xu, Y. Yang, C. H. Wang, L. Zhao, Simultaneous low-frequency vibration suppression and energy harvesting using a metastructure with alternately combined nonlinear local resonators. *Mechanical Systems and Signal Processing* **211**, 111241 (2024), doi:10.1016/j.ymssp.2024.111241.

6. J. Hyun, J. Jung, J. Park, W. Choi, M. Kim, Simultaneous low-frequency vibration isolation and energy harvesting via attachable metamaterials. *Nano Convergence* **11** (38) (2024), doi:10.1186/s40580-024-00445-2.

7. J. Park, G. Lee, H. Kwon, M. Kim, J. Rho, All-Polarized Elastic Wave Attenuation and Harvesting via Chiral Mechanical Metamaterials. *Advanced Functional Materials* **34** (39), 2403550 (2024), doi:10.1002/adfm.202403550.

8. R. U. Ahmed, S. Banerjee, Low frequency energy scavenging using sub-wave length scale acousto-elastic metamaterial. *AIP Advances* **4**, 117114 (2014), doi:10.1063/1.4901915.

9. J. Li, X. Zhou, G. Huang, G. Hu, Acoustic metamaterials capable of both sound insulation and energy harvesting. *Smart Materials and Structures* **25** (4), 045013 (2016), doi:10.1088/0964-1726/25/4/045013.

10. J.-S. Chen, W.-J. Su, Y. Cheng, W.-C. Li, C.-Y. Lin, A metamaterial structure capable of wave attenuation and concurrent energy harvesting. *Journal of Intelligent Material Systems and Structures* **30** (20), 2973–2981 (2019), doi:10.1177/1045389X19880023.

11. Z.-Q. Lu, L. Zhao, H. Ding, L.-Q. Chen, A dual-functional metamaterial for integrated vibration isolation and energy harvesting. *Journal of Sound and Vibration* **509**, 116251 (2021), doi: 10.1016/j.jsv.2021.116251.

12. D. Misseroni, A. B. Movchan, D. Bigoni, Omnidirectional flexural invisibility of multiple interacting voids in vibrating elastic plates. *Proceedings of the Royal Society A: Mathematical, Physical and Engineering Sciences* **475** (2229), 20190283 (2019), doi:10.1098/rspa.2019.0283.

13. S. Timoshenko, S. Woinowsky-Krieger, *Theory of plates and shells* (McGraw-Hill Book Company, New York) (2002).

14. P. Hagedorn, A. DasGupta, *Vibrations and Waves in Continuous Mechanical Systems* (Wiley, Chichester) (2007).

15. A. Movchan, N. Movchan, I. Jones, D. Colquitt, *Mathematical Modelling of Waves in Multi-Scale Structured Media*, Chapman & Hall/CRC Monographs and Research Notes in Mathematics (CRC Press) (2017).

16. D. Tan, Y. gang Leng, Y. Gao, Magnetic force of piezoelectric cantilever energy harvesters with external magnetic field. *The European Physical Journal Special Topics* **224**, 2839–2853 (2015), doi:10.1140/epjst/e2015-02592-6.

17. L. Tang, Y. Yang, C.-K. Soh, Improving functionality of vibration energy harvesters using magnets. *Journal of Intelligent Material Systems and Structures* **23** (13), 1433–1449 (2012), doi:10.1177/1045389x12443016.

18. D. Vokoun, M. Beleggia, L. Heller, P. Sittner, Magnetostatic interactions and forces between cylindrical permanent magnets. *Journal of Magnetism and Magnetic Materials* **321**, 3758–3763 (2009), doi:10.1016/j.jmmm.2009.07.030.

19. A. Erturk, D. Inman, *Piezoelectric Energy Harvesting* (Wiley, Chichester) (2011).

20. A. Erturk, D. Inman, A distributed parameter electromechanical model for cantilevered piezoelectric energy harvesters. *Journal of Vibration and Acoustics* **130** (4), 041002 (2008), doi: 10.1115/1.2890402.

21. S. Strogatz, *Nonlinear Dynamics and Chaos: with applications to physics, biology, chemistry and engineering* (Westview Press, Boulder) (2014).

22. J. P. Norenberg, R. Luo, V. G. Lopes, J. V. L. Peterson, A. Cunha, Nonlinear dynamics of asymmetric bistable energy harvesters. *International Journal of Mechanical Sciences* **257**, 108542 (2023), doi:10.1016/j.ijmecsci.2023.108542.

23. G. A. Gottwald, I. Melbourne, A new test for chaos in deterministic systems. *Proceedings of the Royal Society of London. Series A: Mathematical, Physical and Engineering Sciences* **460** (2042), 603–611 (2004), doi:10.1098/rspa.2003.1183.